Alma Mater Studiorum – Università di Bologna

DOTTORATO DI RICERCA IN

Ingegneria Civile, Chimica, Ambientale e dei Materiali

Ciclo XXX

Settore Concorsuale: 09/D2 - Sistemi, metodi e tecnologie dell'ingegneria chimica e di processo

Settore Scientifico Disciplinare: ING-IND/24 - Principi di ingegneria chimica

VIRTUAL PROTOTYPING OF PHARMACEUTICAL GRANULATION AND COATING EQUIPMENT

Presentata da: Luca Del Bene

Coordinatore Dottorato

Prof. Luca Vittuari

Supervisore

Prof. Maria Grazia De Angelis

Co-Supervisore

Prof. Michele Pinelli

Esame finale anno 2018

It is very difficult for us, placed as we have been from earliest childhood in a condition of training, to say what would have been our feelings had such training never taken place.

George Gabriel Stokes

To my nephews, Diego

and Giacomo

Index

Abstract

A virtual prototyping methodology for pharmaceutical granulation and coating has been developed. Application of the Multiphase Particle-In-Cell method (MP-PIC) allowed to simulate two-phases gas-solid flow that occurs in granulation and coating equipment. The computational performance of MP-PIC model is very high. The use of CPFD® Barracuda VR™, which implements the MP-PIC model, was validated against literature experimental and CFD-DEM data, showing its critical points. Barracuda VR™ overestimates the particle transport, but, at the same time, it captures the major trends in the considered physical quantities. This makes Barracuda VR™ a valid instrument to conduct relative comparative analysis, while it is considered less reliable in the estimation of absolute performance values. The application of Barracuda VR™ was evaluated using a Wurster coater for pharmaceutical application. It was found that an air flow rate equal to 800 Nm^3/h in the considered machine allows a best performance measured in terms of coating distribution homogeneity on pellets. Several virtual prototypes were modeled to obtain a rotating fluidized bed in a static geometry (RFB-SG), called “Spin Flow”. The spin flow fluidized bed (SFFB) must be adapted to perform both granulation

and coating processes. Virtual experiments were made, using Barracuda VR™, by varying the air flow rate at the different inlets of the prototypes, but keeping the total air flow rate constant and equal to the best one found for the Wurster process. It was found that one virtual prototype, i.e., the one with four lateral inlets, was good to obtain a spin flow fluidized bed with small particles, as the one used for granulation process, but with the present virtual prototypes it was not possible to obtain a spin flow fluidized bed for larger particles, as the one used for Wurster coating process.

Sommario

È stato sviluppato un metodo per la prototipazione virtuale di macchine per la granulazione e il rivestimento di particelle in ambito farmaceutico. L'applicazione del modello Multiphase Particle-in-Cell (MP-PIC) ha permesso di simulare il flusso bifase gas-solido presente in granulatori e rivestitori con prestazioni computazionali molto elevate. L'utilizzo di CPFD® Barracuda VR™ è stato validato su dati sperimentali e dati di simulazioni CFD-DEM presenti in letteratura mostrando le sue criticità. La tendenza a sovrastimare il trasporto di particelle, ma allo stesso tempo la capacità di catturare l'andamento delle grandezze fisiche considerate, fanno di Barracuda VR un ottimo strumento per analisi comparative, mentre è considerato meno affidabile per stimare valori e performance assoluti. L'applicazione di Barracuda VR è stata valutata su un rivestitore Wurster per applicazioni farmaceutiche. È stato possibile valutare che una portata d'aria di 800 Nm^3/h permette la migliore performance in termini di omogeneità di distribuzione del rivestimento sulle particelle. Diversi prototipi virtuali sono stati modellati per ottenere un letto fluido rotante in una geometria statica (RFB-SG), detto "Spin Flow". Il letto fluido di tipo spin flow (SFFB) deve essere adattabile sia

a processi di granulazione che a processi di rivestimento. Sono stati condotti degli esperimenti virtuali, usando Barracuda VR™, variando la portata d'aria agli ingressi dei prototipi virtuali, ma mantenendo la portatat d'aria totale costante e uguale a quella trovata per il processo Wurster. Questi esperimenti virtuali hanno evidenziato che un prototipo virtuale, ovvero quello con quattro ingressi laterali, ha reso possibile ottenere un letto fluido spin flow con particelle piccole, tipiche della granulazione, ma con i presenti prototipi non è stato possibile ottenere un letto fluido spin flow per particelle più grandi, tipiche dei processi di rivestimento Wurster.

List of Figures

List of Tables

Nomenclature

Roman Letters

C	Porous coefficient matrix for inertial term
C_d	Drag coefficient
D	Porous coefficient matrix for viscous term or Drag model
d	Diameter
E	Energy
$F_{1,2}$	Blending functions
$\vec{F}$	Force
$\vec{g}$	Gravity
h	Enthalpy
I	Moment of inertia
$\vec{J}$	Diffusion flux
k	Turbulent kinetic energy
k_{eff}	Effective conductivity
m	Mass
n_c	Number of particles
p	Static pressure
Re_t	Turbulent Reynolds number
s	Thickness
S	Source term
T	Torque
t	Time
$\vec{v}$	Velocity
V	Mean velocity

Greek Letters

α	Volume fraction
β	Drag law expression
ε	Dissipation rate of turbulent kinetic energy
λ_s	Granular pressure
μ_s	Solid shear viscosity
ρ	Fluid density
Θ	Granular temperature
ϕ	Particle probability function
$\bar{\bar{\tau}}$	Stress tensor
τ	Interparticle stress
ω	Specific dissipation rate of turbulent kinetic energy
$\vec{\omega}$	Rotational velocity

Abbreviations

AHU	Air Handling Unit
API	Active Pharmaceutical Ingredient
CFB	Circulating Fluidized Bed
CFD	Computational Fluid Dynamics
CFL	Courant-Friedrichs-Lewy condition
CPFD	Computational Particle Fluid Dynamics
CTD	Cycle time distribution
CW	Confidence width
DEM	Discrete Element Method/Model
DNS	Direct Numerical Simulation
ECT	Electrical Capacitance Tomography
HEPA	High-Efficiency particulate air
ICT	Information and Communication Technology
KTGF	Kinetic Theory of Granular Flow
LES	Large Eddy Simulation
LHS	Left Hand Side
MP-PIC	Multiphase Particle-In-Cell
PEPT	Positron Emission Particle Tracking

PH	Peak Height
PNC	Peak normal coating
PW	Peak Width
RANS	Reynolds Average Navier-Stokes
RFB-SG	Rotating Fluidized Bed in a Static Geometry
RHS	Right Hand Side
RTD	Residence time distribution
SFFB	Spin Flow Fluidized Bed
SGS	Sub-grid scale
SM2020	Smart Manufacturing 2020
SST	Shear stress transport
TFM	Two Fluid Model
VP	Virtual Prototyping/Prototype
VPD	Virtual Product Design

Subscripts

c, ij	contact between particles i and j
cp	Closing pack
d, ij	viscous damping between particles i and j
$d, g-i$	gas-particle drag
g	Gas
h	Enthalpy
i, j	Index for particles, species, phases or directions
m	Mass
s	Solid

Introduction and motivations

The work presented in this report deals with the major topic of the smart manufacturing. In fact the project is fully granted by the Cluster project Smart Manufacturing 2020: CTN01_00163_216744 (SM2020) [1]. The project SM2020 applies to Italian industries and aims to deal with future and present challenges represented by the economic crisis and competition of emerging markets such as China, India and Brazil [1]. Innovative information and communication technologies (ICT) must be developed and deployed within the industry partners. The concept of smart manufacturing is sometimes referred as "Industry 4.0", aimed to consider it as the fourth industrial revolution [2]. Advanced manufacturing countries such as Germany, United States and South Korea have already implemented policies to fund smart manufacturing research and development [2]. However, these concepts are very recent: in Germany, the Industry 4.0 concept was announced only in 2011 [2]. Italy has immediately followed this trend with different cluster projects and one of them is the Smart Manufacturing 2020 with its four lines of research and innovation: (1) Smart Monitoring and Planning, (2) Smart Maintenance, (3) Smart Products and Services and (4) Virtual Product and Production Design. Of these four lines of research and innovation, this work is related to the fourth goal "Virtual Product and Production Design" (VPD). VPD aims to design the product through the

development of a virtual prototype which is a geometric model able to conduct certain simulations [3]. Prototyping stage is thought to be necessary during the design process of a new product, but production and analysis of a physical prototype could be very time consuming and could generate high costs [3]. On the other hand, VPD could decrease these costs and could be used for the whole construction, its subunits and individual parts [3]. A definition of virtual prototyping is proposed by Wang [4]:

> *"Virtual prototype, or digital mock-up, is a computer simulation of a physical product that can be presented, analysed, and tested from concerned product life-cycle aspects such as design/engineering, manufacturing, service, and recycling as if on a real physical model. The construction and testing of a virtual prototype is called virtual prototyping (VP)."*

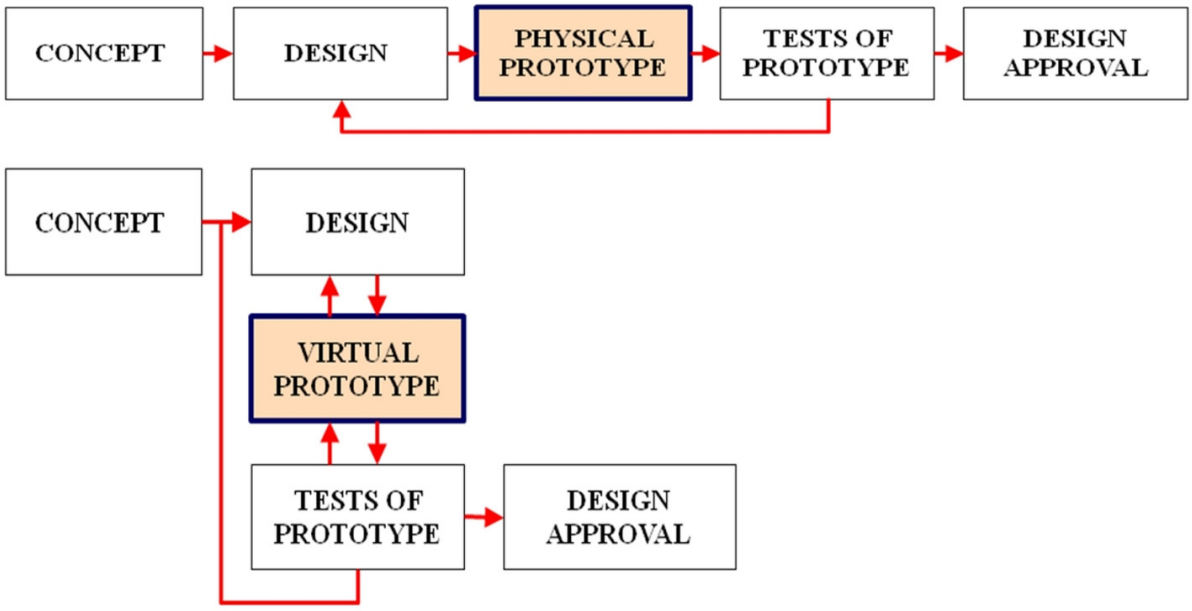

Figure I 1 Łukaszewicz comparison of traditional design and virtual prototype approaches [3].

As can be drawn from this definition, VP could be very broad and encompasses many aspects. Moreover, fields of application of VP are countless within industry. For instance, Barnat et al. and Zhang et al. [5,6] applied VP technique to reliability prediction of electronic packaging. VP can be applied also to design the process of production of a certain chemical as investigated by Conte et al [7]. An immersive environment such as virtual reality could also be place for VP as presented by Bao et al. in an early stage of virtual reality technology [8]. They proposed to apply an immersive Virtual Product Design to many industrial production design stages such as performance evaluation and product line simulation [8]. Virtual Product Design can also be collaborative: Lau et al. proposed an interactive design visualization system in order to let stakeholders of the design stage work at the same time and visualize the design process in real time [9]. An Internet based Virtual Reality collaborative environment was also introduced by Kan et al. [10]. Despite VP could be confused with standard engineering simulations, VP has a bigger scope, but remains a computer aided simulation. Moreover, finding differences between the two definitions could be time-demanding and pointless [4].

The SM2020 project encourages collaborations between academic and industry partners and this thesis is the results of the collaboration of University of Bologna and I.M.A. S.p.A. [11]. I.M.A. S.p.A., located in Ozzano dell'Emilia (BO), is an Italian company which produces high-technology automatic machines for pharmaceutical, food and other industries. Collaboration with the Active division of I.M.A.'s Pharma sector was tight and led to the main results obtained in this work. The main goal of the collaboration is to gain insights in the design of virtual prototype of granulators and coaters machine. As of today, granulation and coating are performed by a machine produced by I.M.A. in two different configurations [12]. Granulation is performed in a standard batch fluidized bed [13] while coating is performed in a forced

spouted bed process named Wurster process [14]. The two configurations are possible in the same machine, but it is required to manually exchange a part of it. The main goal of this project is to design a new machine able to perform both granulation and coating for pharmaceutical purpose. The new machine will ideally introduce a vortex chamber fluid bed to exploit high centrifugal accelerations [15]. The vortex chamber fluid bed will be called "Spin-Flow fluid bed" (SFFB) or simply "Spin-Flow" throughout this thesis and it is the subject of the Virtual Prototyping goal of the project.

It is very important to select the correct tools to perform Virtual Prototyping and, considering the importance of the flow field inside the Spin-Flow fluid bed, the Computational Fluid Dynamics techniques were chosen. Computational Fluid Dynamics (CFD) is a common technique for Virtual Prototyping and it can be applied to chemical and pharmaceutical industries [16]. CFD simulations consist in solving conservation equation of mass, momentum and energy of a fluid flow while imposing a set of boundary condition [16]. Spatial and time domains of the set of equations must be discretized in order to find a numerical solution. Discretization techniques for CFD are nowadays well established [17], but improvements in computational power are making CFD a more valuable tool for pharmaceutical applications such as mixing, solids handling, separation and packaging [16]. When particles do not have a sensible effect on the fluid flow, they are considered passive contaminants and their flow can be easily retrieved after resolving the fluid flow [18]. However, in granulation and coating applications, the presence of particles is dense and strongly affects the momentum and the energy of fluid flow. Therefore, CFD must be coupled with a model aiming to calculate the solid flow as well.

The most common models for solid flows are Eulerian-Eulerian and Eulerian-Lagrangian and the choice between them was part of the project. The Multi Phase Particle-In-Cell (MP-PIC) is a novel Eulerian-Lagrangian model aimed to deal with dense particle flow [19]. This model is implemented in a commercial software which allows calculation on GPU Cuda Cores. A comparison of MP-PIC model with the Discrete Element Model (DEM) was performed to highlight the capability of the first one to deal with larger machines such as the ones produced by I.M.A. It is opinion of the author that application of MP-PIC provides a suitable tool to virtual prototyping fluidized bed thanks to its easy scalability and a very fast computational performance compared to other methods. This thesis is structured as follow: first a review of the state of the art of granulators and coaters is given Section 1. A review of the mathematical models for CFD and solid flow simulation is given in Section 2. Section 3 explains a case study of a present granulator/coater which was performed to gain experience with the virtual prototyping tools. The main and conclusive study of a virtual prototype of a pharmaceutical granulator and coater is presented in Section 4. It is important to notice that some parts of this thesis could be similar to the deliverables handed in for the project SM2020 as it is the "driving force" of the PhD project.

Section 1
State of the art

This section presents an overview about granulation and coating with special emphasis on fluidized bed equipment. The section reviews also CFD simulations studies applied to granulators and coaters, despite literature is not broad.

1.1 Fluidization theory

Fluidized bed granulators use the principle of fluidization by which a packed bed of solid particles is made in contact with a gas flow [13]. When the gas flow crosses upwards the packed bed of solid particles with a sufficient superficial velocity, known as minimum fluidization velocity, the drag forces acting on the particles are strong enough to overcome the weight of the particle bed which becomes a suspended bed [13]. Therefore, the bed is said to be fluidized because it shows some macro-physical properties of fluids [20]. The distinction between fixed bed and fluidized bed is, therefore, dependent on the gas velocity and pressure drop. An example of the relation between these two quantities is given in Figure 1.1 [13]. Researchers tried to distinguish among different type of fluidized bed which are dependent on particles types and air velocity. Particle fluidization behavior was deeply studied by Geldart [21]. Geldart's

categorization of particles has probably been the most used so far [20]. Particle-fluid interaction is categorized by the particle size and the difference in density between particles and fluid, as shown in Figure 1.2 [21]. Particles of group C are said to be "cohesive" and they are hardly fluidized. They tend to form agglomerates and acting as larger particles. Particles from group A are said to have aeration property and are particularly suited for coating [22]. The Geldart's group B contains sand-like particles and group D contains spoutable particles [22]. By increasing the air velocity, the bed shows the following behaviors [20]: **packed bed.** The bed is packed when velocity is less than the minimum fluidization velocity; **particulate regime.** Once the minimum fluidization velocity is reached, the bed is in the particulate regime for particle of group A only; **bubbling regime.** The regime of bubbling fluidized bed is reached after the particulate regime, when the minimum bubbling velocity is reached, but particles of group B and D tend to have the minimum bubbling velocity undistinguishable from the minimum

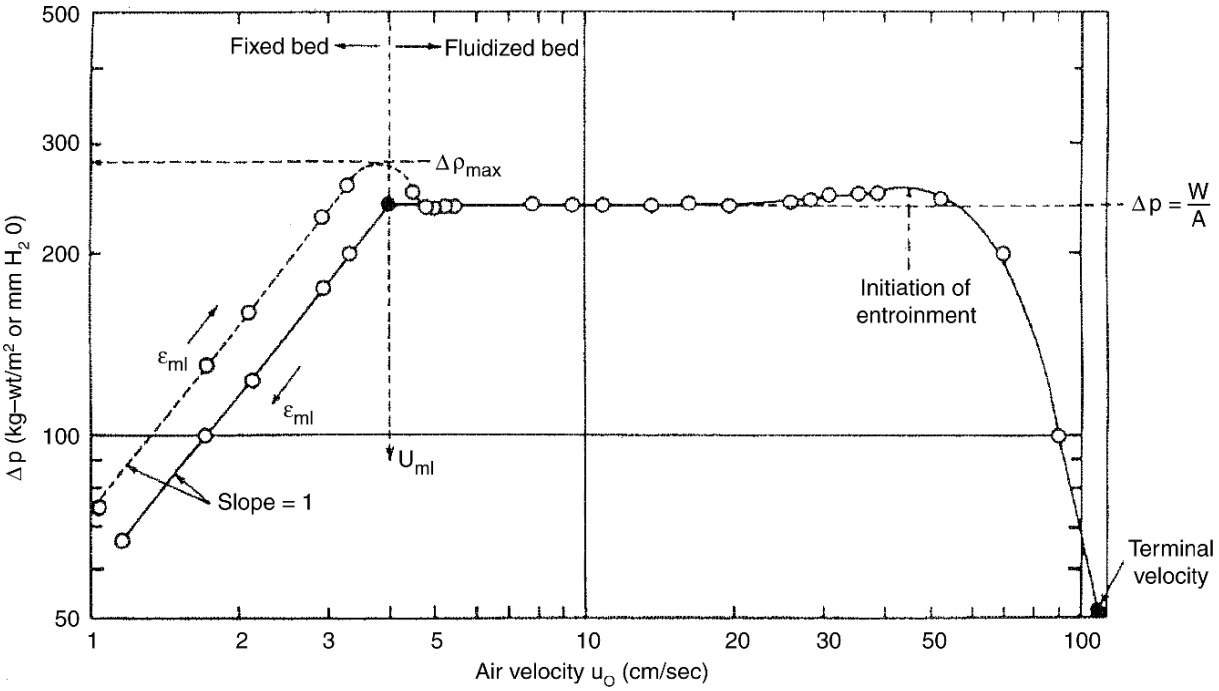

Figure 1.1 Relation between superficial velocity and pressure drop in a fluidized bed [13].

fluidization velocity; **slug flow regime.** When velocity is further increased, it is possible, in small diameter columns equipment, to form slugs limiting solids mixing and creating strong pressure fluctuations; **turbulent regime.** An increase in gas velocity produces the turbulent disrupting of bubbles. In this regime, the maximum of heat and mass transfer is reached. After this regime, the bed is not recognizable anymore, but particles are transported as a dilute phase. These regimes are summarized in Figure 1.3. Finally, a **spouted bed regime** is a fluid bed in which the gas forms a single central channel where solid is entrained for falling outside. This channel could naturally form or could be forced by the special geometry of the bed, as in the Wurster process, a special spouted bed used for coating purposes [14,23–26].

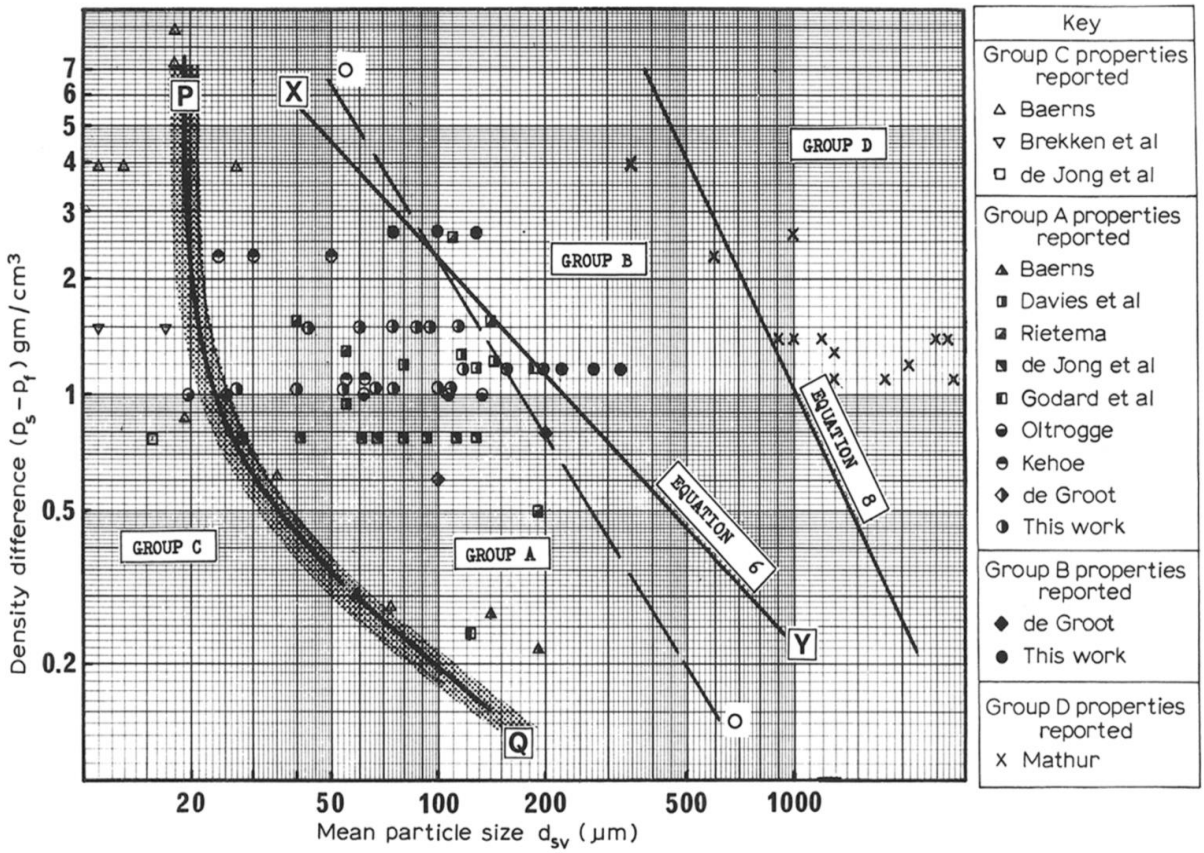

Figure 1.2 Geldart particles categories [21].

1.2 Granulation and equipment

Granulation is a particle dimension growing process which occurs by agglomeration of small particles in permanent structures in which original particles are still recognizable [27]. This process occurs usually by wetting solid particles with a solvent, usually called binder, which bounds smaller particles to form size-controlled agglomerates thanks to the superficial tension [28]. Granulation using solvent is one of the most important unit operation in pharmaceutical industry [29]. There are many reasons why a pharmaceutical preparation, which includes both active pharmaceutical ingredient (API) and excipients, is granulated. These reasons could be, among others, to enhance uniformity of APIs distribution and to augment flowability and compactability [30]. This last reason has a major importance in dealing with the production of tablets.

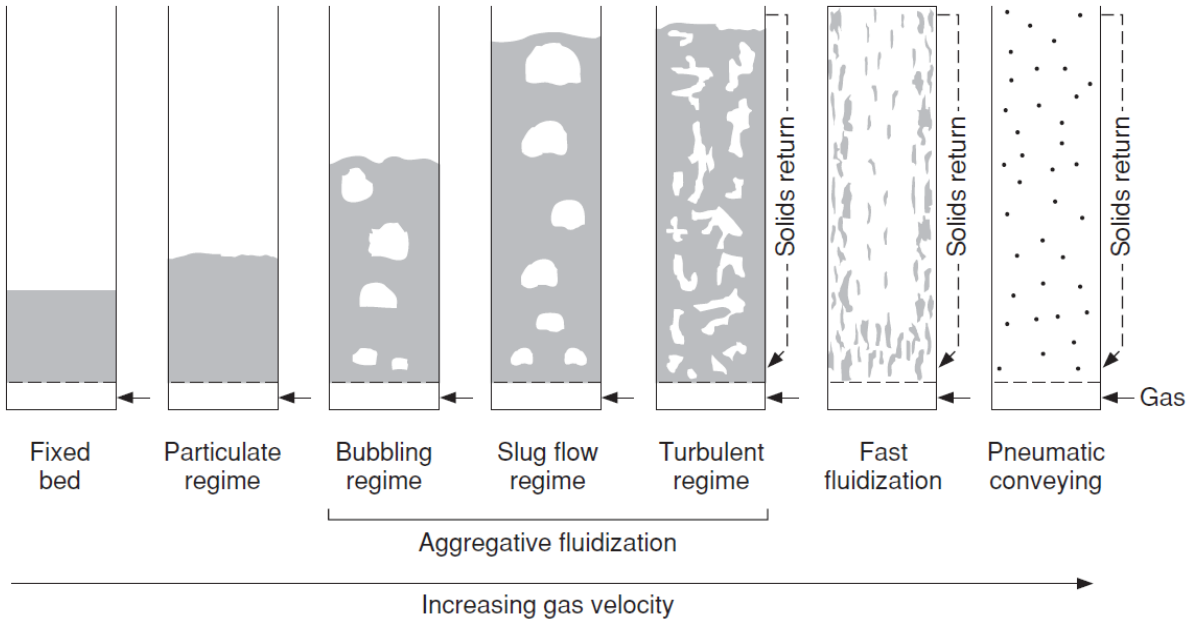

Figure 1.3 Regimes of fluidization [20].

High shear mixers and granulators are machines that perform the spraying of binder on particles which grow in a batch process [31]. However, the process must undergo through another machine to perform drying of wet particles and complete granulation [31]. This kind of granulators has been studied to gain knowledge about granular flows properties [29]. Fluidized bed granulators are another type of granulators. While high-shear mixers work in a batch process

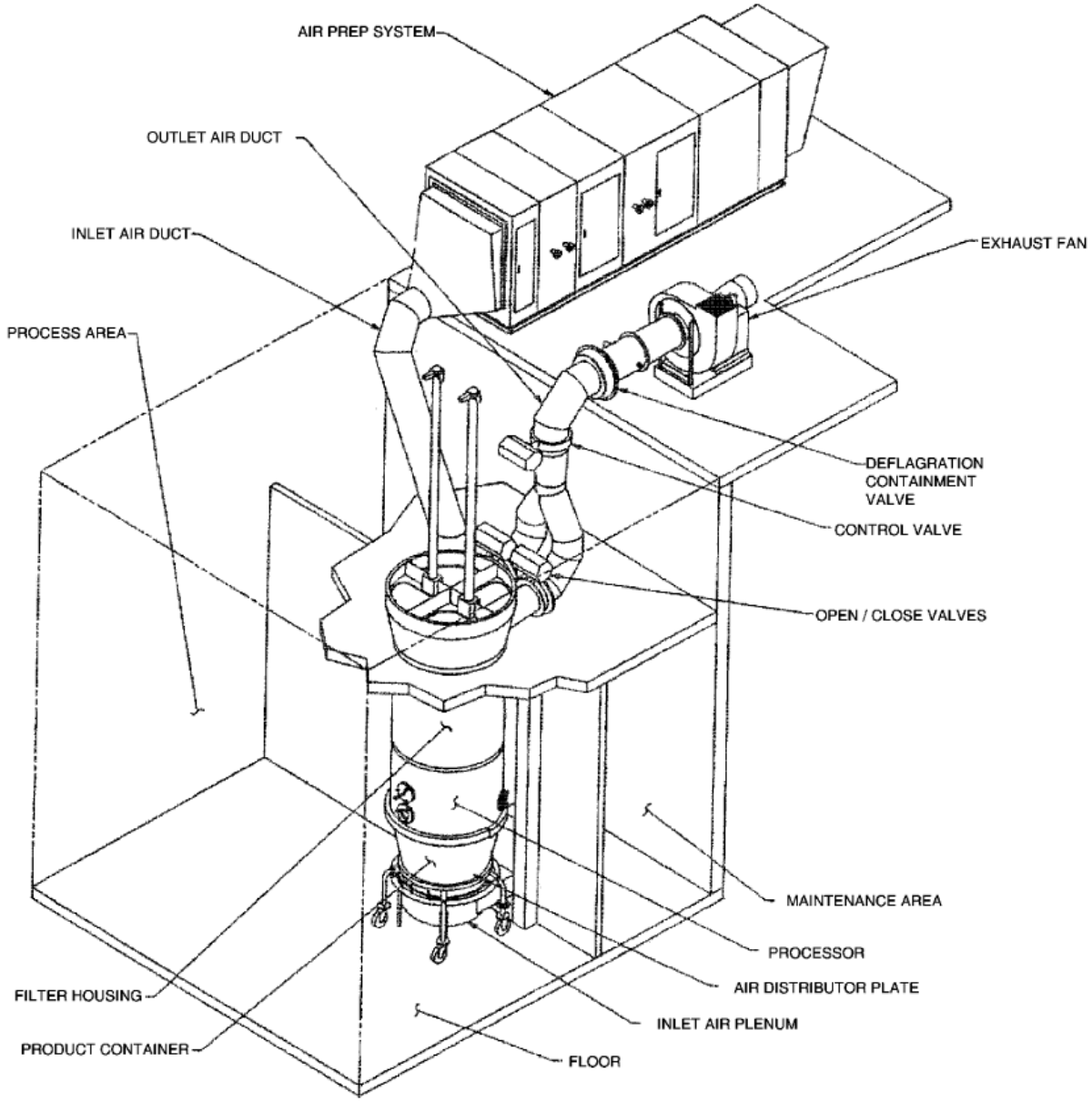

Figure 1.4 All components of a typical fluid bed granulator [13].

only, fluidized bed granulators can be adapted to work continuously (even if batch fluid bed granulators are more common) and can perform the drying phase as well [22,30,31]. A fluid bed granulation process involves several unit operations. In Figure 1.4 all components deputed to perform these unit operations are shown [13] and a brief description proposed by Parikh and Mogavero is given [13]:

- air passes through an air handling unit (AHU) to be prepared to be sent to contact with the product. AHU consists in filters, heat exchangers, dehumidification/rehumidification units and a high-efficiency particulate air (HEPA) filter;
- air is then directed to the inlet air plenum where it expands to evenly pass through the distributor plate;
- air is distributed in the product container (also called "product basket") where the contact between air and solid product occurs;
- after leaving the bed, air goes in the disengagement area or product chamber where larger particles lose momentum and fall back into the product basket;
- either in the product basket or in the product chamber the spray nozzle ensures the binder distribution; among the various types of spray nozzle, the two-fluid nozzle is the most commonly used for granulation. In this type of nozzle, the binder solution is atomized by compressed air;
- smaller particles are entrained; thus, cartridge filters are needed. These filters are kept clean thanks to an alternating blowback pulse;
- exhaust air goes through a fan which provides the air motion and a pressure under 1 atm. This ensures containment of API;

1.2.1 CFD modeling of fluid bed granulators

There has been a wide interest in simulation of granulators, but literature about CFD modeling of granulators is not broad and is never comprehensive of all processes that occur in granulation, likely because of computational burdens [32]. However, the use of CFD techniques has been applied to fluidized bed machines in many applications, but also to high-shear mixers. This section considers a generic fluid bed modeling approach, high shear mixer, circulating fluidized bed riser (CFB) and a couple of fluidized bed for granulation.

Considering CFD techniques, Ng et al. tried to model a high-shear mixer using an Eulerian-Eulerian approach also called the two fluids model (TFM) [29]. This model is claimed to be the most employed for modeling granular flows where the solid phase has a high volume fraction [33]. This approach considers the granular material as a continuum fluid which is modeled based on the kinetic theory of granular flow (KTGF) [34,35]. Granular phase and gas phase are considered as interpenetrating continua. By confronting simulations and experimental data, Ng highlights how this model can describe the volume fraction of granular phase with a certain degree of accuracy, but it shows a lack of accuracy in the description of velocity of the solid phase near the walls [29].

Despite the use of a very simple 2D geometry, the 2011 work of Chen et al. gives a very broad comparative analysis of different aspects of fluidized bed modeling [36]. After analyzing the effects of wall phase slip, Chen et al. proposed that the granular phase should use a full slip behavior at walls. No sensible differences were found in the introduction of the van Wachem simplification, which consists in dissipating the granular energy locally in the standard KTGF use [37]. Therefore, van Wachem simplification should be used, since it provides less

computational costs. For the same gas velocity, fluidization is much faster for higher coefficients of momentum restitution. This happens because a higher coefficient of momentum restitution causes a higher degree of elasticity in particle-particle contacts, resulting in a more relaxed packed bed which is easier to fluidize. Along with these model parameters, this work investigates also the effect of several process parameters, such as the shape of the distributor, the velocity of the air flow, the difference between batch and continuous feeding and the particle size.

Upadhyay and Park [38] partially extended the study of Chen et al. using CFD techniques to study a 2D simplified geometry of a circulating fluidized bed. The model used was the Eulerian-Eulerian TFM, while the coefficient of momentum restitution was used as adjustable parameter to validate the volume fraction of solid to match with the experimental evidences. A comparison between the models for granular viscosity of Syamlal [39] and Gidaspow [40] highlighted how the former can predict the volume fraction of solid in a better way, while the latter correctly predicts the axial heterogeneity of the system.

A similar work was performed by Hartge et al. in 2009 [33]. In this work, a tridimensional model of a CFB was studied by using CFD techniques. This work offers also a limited comparison between experimental data of a CFB plant and the CFD simulation results. The Eulerian-Eulerian approach was used and, as described by Upadhyay and Park [38], Gidaspow and Syamlal laws were evaluated along with the coefficient of momentum restitution. Moreover, also the Energy Minimization Multi Scale (EMMS) law was evaluated [41]. EMMS could be able to consider the different drag forces that occur due to the formation of agglomerates. This ability is peculiar for application to granulation where agglomerates form.

The two phase Eulerian-Eulerian approach is the most exploited in literature, probably because it is computationally less demanding [32]. However, considering the granular phase as a fluid that can penetrate the gas could introduce a very strong modeling. Moreover, the model cannot predict the trajectories of particles. In order to predict the trajectories of particles, a Lagrangian model for solid phase is needed. A common approach to predict particles trajectories is to consider particles as passive contaminants, i.e. they do not affect fluid flow [42]. This is called one-way interaction model [42]. This approach does not consider the particle-particle interaction and it is, therefore, suitable for very low solid volume fractions only. Therefore, it is not suitable for modeling fluidized bed where the solid volume fractions are high. The discrete element method (DEM) considers all forces acting on a single element, either it is a single particle or an agglomerate. To take into account the two way interaction between particles and fluid it must be coupled with CFD and it is then known as CFD-DEM [24,43].

Fries et al. [43] studied granulators by using CFD-DEM. They compared a standard top spray granulator with a Wurster coater/granulator. However, the sprayed binder liquid was not simulated, since they measured the homogeneity of the distribution of binder over particles by calculating the residence time distribution of particles in the spraying zone. Evidences showed that the Wurster configuration had a thinner residence time distribution which is likely related to a better homogeneity of binder distribution on particles.

A very important aspect of this review is that every author focused on the fluid dynamic behavior of granulators only, usually without binder spraying or considering only a spray zone (e.g. [43]), but none of them proposed a suitable model for particle agglomerates formation. Population balance models were proposed by Kumar et al. and Liu et al. [44,45], but they are only suitable

for small systems, since they require too high computational power. Therefore, a proper model for granulation is still missing.

1.3 The Wurster coating process

The Wurster coating process allows functionalization of excipient pellets or particles by depositing on them the active pharmaceutical ingredients or other functional films [14]. This process is widely used in pharmaceutical industry as well as in food industry [46]. The Wurster process occurs in a fluid bed machinery, the Wurster coater, made by a conical part in which a thin-walled vertical tube drives particle motions [24]. It is possible to divide the Wurster coater in different zones as shown in Figure 1.5. The whole Wurster equipment is the same as described in Figure 1.4, except for the presence of the Wurster tube in the center of the product basket and a non-homogeneous flow distribution plate which influences the fluid dynamic behavior in this zone. The air distribution plate is made in such a way to ensure that most of the air passes in the central part of the plate which is placed right below the downward Wurster tube, resulting in a spouted bed behavior [23,24]. Air passing through the outer part of the distribution plate ensures that the bed outside the Wurster tube is kept slightly fluidized so that the hot air could dry the coated particles [24]. There is a small adjustable gap between the Wurster tube and the distribution plate. In the center of the plate the binder atomizer, which is usually a two fluids nozzle, is placed pointing upwards [14,23]. This set up ensure that particles are spouted to rise in the Wurster tube after passing through the atomizer spray zone [24]. Spouted particles exit the Wurster tube to reach the fountain region (corresponding to the product chamber) where they lose momentum and move radially to reach the external part of the equipment and then fall

to the downbed region [23,24]. While being dried, particles in the downbed region slowly move down to reach the horizontal transport region [23]. Once there, particles move radially to the center of the equipment, thanks to the drag of the spouted region to complete the cycle in the machine [24]. This circulating particle flow that occurs in Wurster coater is likely to make this solution the best suited for small particles coating [22]. Recent findings suggest that the Wurster coater could be adapted to work continuously, as shown in Figure 1.5 [46].

1.3.1 CFD Modeling of Wurster coaters

Modeling of coating attracted more researcher than modeling of granulation, resulting in a much broader literature. However, modeling strategies are quite similar to the ones presented in section 1.2.1, including TFM and CFD-DEM models. Modeling the coating performances was

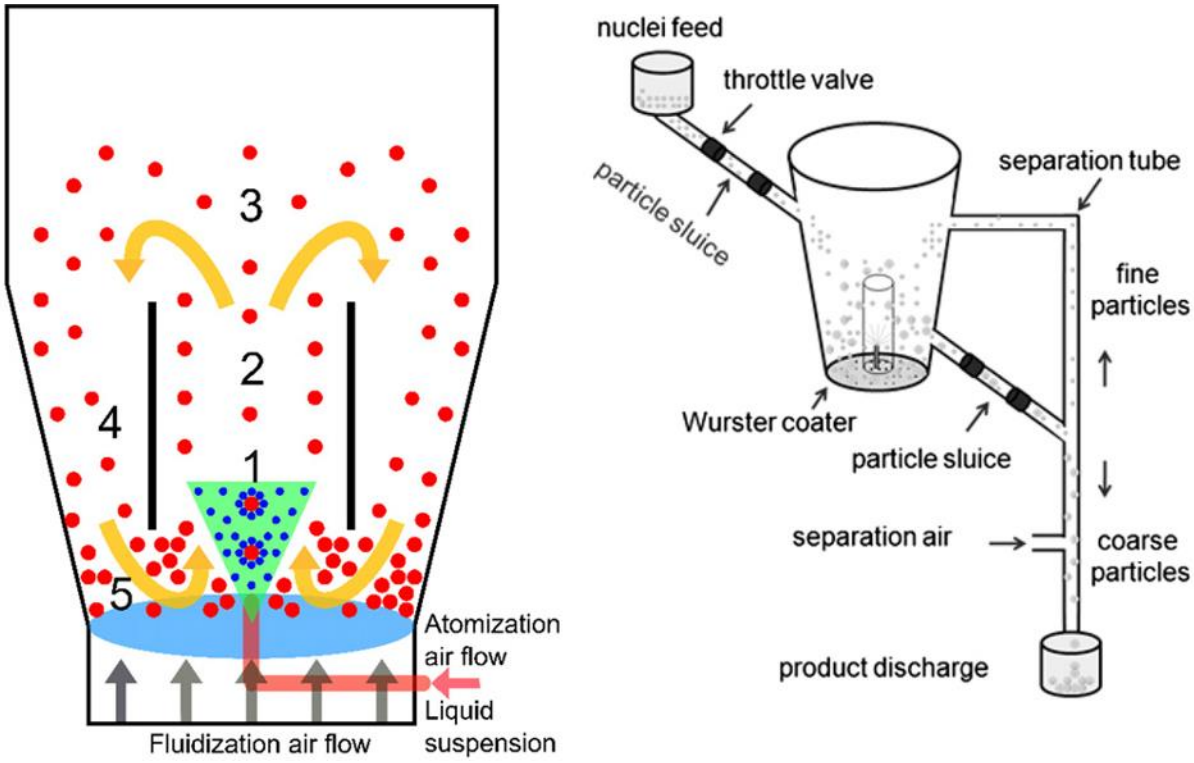

Figure 1.5 LHS: representation of the Wurster fluidized bed with different regions highlighted: (1) spray zone, (2) Wurster tube region, (3) fountain region, (4) downbed region, (5) horizontal transport region [24]. RHS: continuous Wurster coating apparatus [46].

already evaluated in the study by Fries et al.[43] even if they were applied to the binder distribution homogeneity in granulators. In fact, their work involved both granulators and Wurster coaters [43].

Karlsson et al. [26] preferred to use a TFM to simulate the Wurster coater because the expected amount of particles in the batch was up to 2×10^6 and it would require too much computational power if modeled using CFD-DEM. It must be notice that the work by Karlsson et al.[26] was published six years earlier than the work by Li et al. [24]. To provide closures for the particle phase momentum equations they applied KTGF. In this work a wetting model was introduced, but the injection of liquid through the atomizer was modeled by introducing a moisture content in the particle phase when passing in the spray region. The model was detailed thanks also to the addition of the modeling of moisture drying, introducing, therefore, the energy treatment.

Šibanc et al. [25] applied the TFM to an axial symmetric model of a Wurster coater. Despite the simplification of the axial symmetric model, they were able to model also the air distribution plate which is not common in literature. Again, closure for particle momentum equation was given by KTGF model. They set nozzle to spray air only in an amount which was calculated by a single-phase simulation. They evaluated and validated simulations against experiments, considering particles volume fraction, particle velocity and pressure fluctuation in the Wurster tube. Finally, they evaluated the pellet mass flow through the Wurster tube, a quantity which is difficult to measure.

Li et al. [24] calculated the performance of a Wurster coater without simulating the spraying of the coating liquid measuring the cycle time distribution and the residence time distribution in the spraying zone. The model used was CFD-DEM and the simulated system was relatively small to overcome computational burdens: the maximum diameter of the Wurster coater used

was 250 mm and its total height was 417 mm. The number of particles used was between 50,000 and 150,000. Using 32 CPUs on a cluster architecture, typical unsteady simulations took 12 hours per second. In this study, authors evaluated simultaneously different particle sizes finding that bigger particles pass closer to the atomizing nozzle receiving a higher quantity of liquid per pass. This occurrence is compensated by a smaller number of passes in the spraying zone with respect to smaller particles. The result is that in the Wurster coater it is possible to reach a good uniformity of the coating of particles with the sprayed liquid. These results are quite reliable since they were validated against experimental data obtained by Positron Emission Particle Tracking conducted by the same working group [14].

When it comes to deal with larger system than the last shown, it is clear that simulation time is, nowadays, a hard burden and strategies to overcome it are studied. On this purpose, Norouzi et al.[47] proposed a hybrid CPU-GPU solver for CFD-DEM simulations. They use OpenFOAM® solver for CFD and developed an in-house code to solve DEM domain and to couple CFD-DEM. CFD solver and the coupling solver run on the CPU, while the DEM solver runs on the GPU. Architecture used is a workstation equipped with an Intel® core™-i7 (quad core) with 12GB DD3 RAM and an NVIDIA GeForce® GTX 660Ti GPU with 2GB DDR5 RAM. This new software architecture was first successfully verified and then validated with (1) a cylindrical fluidized bed, (2) a spouted bed with a draft tube and (3) a Wurster fluidized bed. The Wurster coater simulation involved 47,200 particles and took 30 minutes of simulation per real time second [47].

Simulation and experimental studies of a lab scale Wurster coater were conducted by Wang et al. [48]. They compared simulation results obtained by TFM and computational particle fluid dynamics (CPFD) to experimental measurements obtained by an in-house made electrical

capacitance tomography (ECT) sensor. CPFD use the MP-PIC model to address the simulation of gas-solid flows [49]. CPFD strategy is an Eulerian-Lagrangian approach and it is implemented in the BARRACUDA-CPFD® package (Barracuda VR) which can parallelize Lagrangian domain of particles calculations on GPU CUDA cores [50]. The main conclusion the authors have drawn is that TFM agrees with experimental data where the solid concentration is lower, i.e. in the Wurster tube region, while CPFD approach describes better the bed behavior in the downbed region. Discrepancies with ECT measurements for CPFD in the low-solid density region and for TFM in the dense bed are mainly due to difficulties in having a good closure law for particle-fluid momentum equation which is valid for a wide range of solid volume fraction [48].

Section 2
Models and methods descriptions and selection

In this section, the most used models in simulation of dense gas-particle systems are presented. Treatment will mainly focus on selected models and their comparison to discarded models.

2.1 Computational Fluid Dynamics basic model

CFD modeling is mainly based on solving the conservation equations of mass, momentum and energy, which are known as Navier-Stokes equations [16]. The mass conservation equation can be written as follows [51]:

$$\frac{\partial \rho}{\partial t} + \nabla \cdot (\rho \vec{v}) = S_m \tag{2.1}$$

where ρ is the density of the fluid, t is the time, $\vec{v}$ is the velocity and S_m is the source term which represents the mass exchanged by the fluid with other phases due to phase change or chemical reactions which are not treated in this work.

The momentum conservation equation, valid for an inertial reference frame is given as [51]:

$$\frac{\partial}{\partial t}(\rho \vec{v}) + \nabla \cdot (\rho \vec{v} \vec{v}) = -\nabla p + \nabla(\bar{\bar{\tau}}) + \rho \vec{g} + \vec{F} \tag{2.2}$$

where p is the fluid pressure, $\bar{\bar{\tau}}$ is the stress tensor, $\vec{g}$ is the gravity acceleration and $\vec{F}$ represents all the external body forces, such as forces from contact with other phases (e.g. drag force) and source terms which are model-dependent (e.g. porous formulation, see Section 2.3). The stress tensor has a high dependency on the viscosity of the fluid [51].

The energy conservation equation can be written as follows:

$$\frac{\partial}{\partial t}(\rho E) + \nabla \cdot \left(\vec{v}(\rho E + p)\right) = \nabla \cdot \left(k_{eff} \nabla T - \sum_j h_j \vec{J}_j + \left(\bar{\bar{\tau}}_{eff} \cdot \vec{v}\right) \right) + S_h \qquad (2.3)$$

where $k_{eff}$is the effective conductivity, T is the absolute temperature, h_j is the enthalpy of species j, $\vec{J}_j$ is the diffusion flux of species j and E is given as follows:

$$E = h - \frac{p}{\rho} + \frac{v^2}{2} \qquad (2.4)$$

S_h is the source term for the energy conservation equation and it includes heat from chemical reaction or other models introduced by the user [51]. Energy conservation equation will be not treated further because it is not used in any part of this work.

2.1.1 Basic simplification of mass and momentum conservation equations

Neglecting the energy conservation equation is a big simplification, however, when temperature changes in the considered control volume are negligible this assumption is fair.

When random phenomena, such as turbulence, are not directly solved, but modeled (e.g. turbulence modeling by a Reynolds Average Navier-Stokes method, RANS), as it will be

discussed later in this section, the flow can reach a steady state so that it is time independent if we consider a time averaged velocity $\langle\vec{v}\rangle$. Moreover, for small Mach numbers, i.e. Ma < 0.3, the flow can be considered incompressible, so its density is constant. These assumptions reduce the mass conservation equation to:

$$\rho\nabla\cdot(\langle\vec{v}\rangle) = S_m \tag{2.5}$$

The effect of averaging quantities, especially velocity, through time will be discussed in Section 2.2.

2.2 Turbulence modeling

Turbulence is a complex three dimensional and time dependent phenomenon [52]. The level of modeling this complex phenomenon must be chosen wisely introducing the minimum amount of complexity needed to capturing the desired physics [52]. The major categories of approaches to model turbulence in CFD are Direct Numerical Simulation (DNS), Large Eddy Simulation (LES) and Reynolds Averaged Navier Stokes Equations (RANS) [52].

2.2.1 Direct Numerical Simulation

Direct Numerical Simulation (DNS) approach tries to solve the three conservation equations without modeling or averaging any quantity, thus resolving all length and time turbulence scales [51,52]. This approach can be very accurate over all scales, however, it is not suitable for high turbulent Reynolds numbers, Re_t, because the computational cost is proportional to the cube of the Reynolds number [51]. Due to its high computational cost, this method is unlikely used for any industrial application.

2.2.2 RANS models

Instantaneous flow velocity could be written as a sum of a time averaged velocity and an instantaneous fluctuation velocity with a statistical approach [52]. Assuming an incompressible flow the cartesian form of the momentum conservation equation is the following [52]:

$$\rho \frac{\partial V_i}{\partial t} + \rho V_j \frac{\partial V_i}{\partial x_j} = -\frac{\partial P}{\partial x_i} + \frac{\partial}{\partial x_j}(\tau_{ji}) + \frac{\partial}{\partial x_j}(-\overline{\rho v'_j v'_i}) \tag{2.6}$$

Where V_i is the mean velocity i^{th} component and x_i is the i^{th} direction. The last term, $-\rho\overline{v'_j v'_i}$ is a symmetric tensor, called the Reynolds stresses, which introduces six new variables, thus a closure for the system is needed [52].

Boussinesq approximation

The first hypothesis to close the system was made by Boussinesq [52]. The Boussinesq approximation relates the Reynolds stresses to the mean velocity gradients by mean of a quantity called turbulent (or eddy) viscosity, μ_t [53]. There are many models using the Boussinesq approximation and they are explained in CFD software manual or books [52–54]. The scope of this work encompasses only the Realizable k-ε and the SST k-ω, so only this two RANS models will be introduced here.

Realizable k-ε

All k-ε models allow the closure of the system of the Navier-Stokes equations by adding two transport equations for the turbulent kinetic energy, k, and its rate of dissipation, ε. With respect to the standard k-ε model, realizable k-ε model has an alternative formulation for the turbulent

viscosity and a modified transport equation for the turbulent kinetic energy dissipation rate. The transport equations for the turbulent kinetic energy and for its dissipation rate are the following:

$$\frac{\partial}{\partial t}(\rho k) + \frac{\partial}{\partial x_j}(\rho k V_j) = \frac{\partial}{\partial x_j}\left[\left(\mu + \frac{\mu_t}{\sigma_k}\right)\frac{\partial k}{\partial x_j}\right] + G_k + G_b - \rho\varepsilon - Y_M + S_k \tag{2.7}$$

$$\frac{\partial}{\partial t}(\rho \varepsilon) + \frac{\partial}{\partial x_j}(\rho \varepsilon V_j) = \frac{\partial}{\partial x_j}\left[\left(\mu + \frac{\mu_t}{\sigma_\varepsilon}\right)\frac{\partial \varepsilon}{\partial x_j}\right] + \rho C_1 S\varepsilon - \rho C_2 \frac{\varepsilon^2}{k + \sqrt{\nu\varepsilon}} + C_{1\varepsilon}\frac{\varepsilon}{k} C_{3\varepsilon} G_b + S_\varepsilon \tag{2.8}$$

$$\mu_t = \rho C_\mu \frac{k^2}{\varepsilon} \tag{2.9}$$

Equations (2.7), (2.8) contain many constants and source terms (among the standard user definable S_k and S_ε) which are not introduced here. Further explanation of these equations is given in [51].

Shear-stress transport k-ω model

The shear stress transport (SST) k-ω model was developed by Menter [55] as a modification of the standard k-ω model proposed by Wilcox [52]. The model utilizes a blending function to switch from standard k-ω model, which is used in the boundary layer, to the k-ω model in outer regions and free shear flows [55]. ω is the specific dissipation rate which could represent the ratio of ε to k. The SST k-ω model is more accurate and reliable for a wide class of flows with respect to the standard k-ω model while keeping the resolution of the boundary layer [55]. Therefore, it is the preferred model when a large geometry system contains parts in which the

boundary layer resolution is important. The transport equations for the turbulent kinetic energy and for its specific dissipation rate are the following:

$$\frac{\partial}{\partial t}(\rho k) + \frac{\partial}{\partial x_i}(\rho k V_i) = \frac{\partial}{\partial x_j}\left[\left(\mu + \frac{\mu_t}{\sigma_k}\right)\frac{\partial k}{\partial x_j}\right] + G_k - Y_k + S_k \tag{2.10}$$

$$\frac{\partial}{\partial t}(\rho \omega) + \frac{\partial}{\partial x_j}(\rho \omega V_j) = \frac{\partial}{\partial x_j}\left[\left(\mu + \frac{\mu_t}{\sigma_\omega}\right)\frac{\partial \omega}{\partial x_j}\right] + G_\omega - Y_\omega + D_\omega + S_\omega \tag{2.11}$$

$$\mu_t = \rho \frac{k^2}{\omega} \frac{1}{\max\left[\frac{1}{\alpha^*}, \frac{SF_2}{\alpha_1 \omega}\right]} \tag{2.12}$$

Again, further description is given in [51]. It is worth to notice that F_2 is a blending function and another blending function, F_1, is included in the definition of σ_k and σ_ω [51].

2.2.3 Large Eddy Simulation

Large Eddy Simulation (LES) is so called because this technique resolves large scale eddies only, so it is halfway between DNS and RANS model. It was first introduced by Smagorinsky and applied for meteorology studies [56]. Application of LES is useful because quantity such as mass and momentum are mostly transported by large eddies which are more problem-dependent and dictated by the geometry and boundary conditions while small eddies are subject to modeling because their nature is more isotropic and less problem-dependent [51]. Modelling of small eddies could be done with the sub grid-scale (SGS) model by Smagorinsky [56] or other models which usually take the Boussinesq hypothesis [51].

2.3 Modeling grids or perforated plates: the porous formulation

It is CFD best practice to not model parts of different scale sizes in the same simulation. This happens because the ratio of volumes of the biggest and smallest cells in the model should not be too high to avoid numerical instabilities [50]. Smaller parts are usually approximated by introducing a model to account for their macroscopic outcomes. For instance, in case of fluidized bed equipment the grids or perforated plates could have holes with a size in the order of millimeters (or less for finer grids) while the whole equipment is larger than a meter. To model such equipment in their whole geometry two ways are possible: (1) using different mesh cell sizes for small and big parts of the model and (2) using small mesh size for the whole model. As already mentioned the first option could lead to numerical instability, while the latter would increase too much the number of mesh elements resulting in need of an unfeasible computational time. Therefore, grids and perforated plates could be accounted only for their macroscopic effect, i.e. a pressure loss term and being modelled as a porous media [53]. In most CFD software, such as Ansys Fluent and Star CCM+, porous media are modelled by adding to the standard fluid momentum conservation equation a source term:

$$S_i = -\left(\sum_{j=1}^{3} D_{ij}\mu v_j + \sum_{j=1}^{3} \frac{1}{2} C_{ij}\rho|v|v_j\right) \tag{2.13}$$

where S is the source term, i and j are the three directions (x, y and z) and D and C are matrices. In case of simple homogeneous porous media, the two matrices are diagonal with $1/\alpha$, which

is the inverse of permeability, and C_2, which is the inertial resistance factor. Thus, for a homogeneous porous media equation (2.13) reduces to:

$$S_i = -\left(\frac{\mu}{\alpha} v_i + \frac{1}{2} C_2 \rho |v| v_i \right) \tag{2.14}$$

which transforms in terms of pressure drop as:

$$\Delta P = \left(\frac{\mu}{\alpha} v_i + \frac{1}{2} C_2 \rho |v| v_i \right) \cdot \Delta s \tag{2.15}$$

where Δs is the thickness of the porous media.

On the other hand, a orthotropic porous mean, such as a perforated plate, can be modelled by increasing of 2 or 3 orders of magnitude two terms of the diagonals of the two matrices and specifying a coordinate system with one collinear coordinate with the desired direction [54]. Increasing too much these two terms would lead to numerical instability while the desired effect is not affected in a sensible way.

This method uses a superficial velocity formulation, thus it does not take into account interstitial velocity in the porous medium which could have effects on heat transfer and chemistry calculation [53].

2.4 Modeling multiphase flows

Nowadays, modelling of multiphase flow using CFD is a possible and deployed technique, but it still represents a challenging task [32]. Present and foreseeable computational burdens are a major concern [32]. Two major approaches were considered by many authors: Eulerian-Eulerian models and Eulerian-Lagrangian models.

2.4.1 The Eulerian-Eulerian Two Fluid Model with Kinetic Theory of Gas Flow

Eulerian-Eulerian model treats gas and solid phase as inter-penetrating continua without monitoring each solid particle trajectory [32]. As previously exposed in Section 1.2.1 and Section 1.3.1, this approach is also known as Two Fluid Model (TFM) and is probably the most used in literature due to its computational efficiency [25,26,29,33,38,48]. This model solves the mass and momentum conservation equations (Equations (2.1) and (2.2)) in a modified version to consider the volume fraction of each phase. If there are no mass exchange between the two phases bass conservation equations for gas and solid respectively become the following [32]:

$$\frac{\partial(\alpha_g \rho_g)}{\partial t} + \nabla \cdot \left(\alpha_g \rho_g \overrightarrow{v_g}\right) = 0 \tag{2.16}$$

$$\frac{\partial(\alpha_s \rho_s)}{\partial t} + \nabla \cdot (\alpha_s \rho_s \overrightarrow{v_s}) = 0 \tag{2.17}$$

Where the g and s represent gas and solid respectively and α is the phase volume fraction. Following the same criteria, the momentum conservation equation for each phases can be written as follow [32]:

$$\begin{aligned} &\frac{\partial}{\partial t}\left(\alpha_g \rho_g \overrightarrow{v_g}\right) + \nabla \cdot \left(\alpha_g \rho_g \overrightarrow{v_g}\, \overrightarrow{v_g}\right) \\ &\qquad = -\alpha_g \nabla p_g + \nabla\left(\overline{\overline{\tau_g}}\right) + \alpha_g \rho_g \vec{g} - \beta\left(\overrightarrow{v_g} - \overrightarrow{v_s}\right) \end{aligned} \tag{2.18}$$

$$\begin{aligned} &\frac{\partial}{\partial t}(\alpha_s \rho_s \overrightarrow{v_s}) + \nabla \cdot (\alpha_s \rho_s \overrightarrow{v_s}\, \overrightarrow{v_s}) \\ &\qquad = -\alpha_s \nabla p_s + \nabla(\overline{\overline{\tau_s}}) + \alpha_s \rho_s \vec{g} + \beta\left(\overrightarrow{v_g} - \overrightarrow{v_s}\right) \end{aligned} \tag{2.19}$$

where the last term on the right-hand side represents the drag volumetric force in which β is a function of the selected drag model. Expressions and models for the drag force will be given in

Section 2.4.4, since its formulation is shared by all multiphase models. The turbulent treatment is either performed using LES or RANS as previously explained in Section 2.2. The stress tensor for the granular phase includes the solid shear viscosity μ_s and the bulk viscosity λ_s which have a different meaning from fluid dynamic viscosity. Moreover, pressure is defined as a property of fluid only, thus, a formulation for the solid pressure must be defined. The concept of solid pressure, solid shear viscosity and solid bulk viscosity are usually described by the Kinetic Theory of Granular Flow (KTGF) [34,35]. According to KTGF, the solid pressure is a function of the momentum restitution coefficient (e), the statistic spatial arrangement of particles (g_0) and the granular temperature (Θ_s):

$$p_s = \alpha_s \rho_s \Theta_s + 2\rho_s(1+e)\alpha_s^2 g_0 \Theta_s \tag{2.20}$$

$$g_0 = \left[1 - \sqrt[3]{\frac{\alpha_s}{\alpha_{s,\mathrm{cp}}}}\right]^{-1} \tag{2.21}$$

$$\Theta_s = \frac{1}{3}(\overrightarrow{v_s}'\overrightarrow{v_s}') \tag{2.22}$$

where $\alpha_{s,\mathrm{cp}}$ is the maximum allowable volume fraction for the solid, the closing pack volume fraction, and $\overrightarrow{v_s}'$ is the solids fluctuating velocity, thus the granular temperature is an estimation of the kinetic energy of the particles. While granular pressure is not dependent on the particle diameter this is not true for the bulk viscosity and the solid shear viscosity. The former has this expression [32]:

$$\lambda_s = \frac{4}{5}\alpha_s \rho_s d_s g_0 (1-e)\left(\frac{\Theta_s}{\pi}\right)^{\frac{1}{2}} \tag{2.23}$$

The solid shear viscosity formulation is the following [32]:

$$\mu_s = \frac{4}{5}\alpha_s \rho_s d_s g_0 (1+e)\left(\frac{\Theta_s}{\pi}\right)^{\frac{1}{2}} + \frac{10\rho_s d_s \sqrt{\pi\Theta_s}}{96(1+e)\alpha_s g_0}\left[1+\frac{4}{5}\alpha_s g_0 (1+e)\right]^2 + \frac{p_s \sin\phi}{\sqrt{I_{2D}}} \tag{2.24}$$

Further explanation of this last equation can be retrieved from [32,34,35]. Since the bulk viscosity and the solid shear viscosity depends on the particle diameter, d_s, this must be unique and well defined to close the problem. If a granular material is composed by solids of two or more particle diameters, it is necessary to define a different phase for each particle diameter [32]. This represents the biggest limitation of the TFM with KTGF because, usually, granular material is composed by solids with a particle size distribution which has a not negligible standard deviation. Moreover, adding too many phases to better represent the particle size distribution increases the computational cost of the simulations, nullifying one of the reason to use this approach.

2.4.2 The Eulerian-Lagrangian CFD-DEM model

The Eulerian-Lagrangian models keeps the treatment of the gas phase equal to the one used in Eulerian-Eulerian models, i.e. by solving the mass and momentum conservation equation, see Equation (2.16) and Equation (2.18). On the other hand, the solid particles dynamics is calculated according to Newton's second law of motion. In the CFD-DEM (Discrete Element Method) the particle interaction model consists in the mechanism of elasticity, damping and slippage [32]. The Newton's second law linear and angular momentum conservation equations are expressed for each particle, i, as follow:

$$m_i \frac{d\overrightarrow{v_i}}{dt} = \sum_{j=1}^{n_c} \left(F_{c,ij} + F_{d,ij}\right) + F_{d,g-i} + F_{p,g-i} + m_i \vec{g} \tag{2.25}$$

$$I_i \frac{d\overrightarrow{\omega_i}}{dt} = \sum_{j}^{n_c} \left(T_{t,ij} + T_{r,ij}\right) \tag{2.26}$$

where m_i is the particle mass, n_c is the number of particles j in contact with particle i, $F_{c,ij}$ is the interparticle elastic contact force, $F_{d,ij}$ is the viscous damping force, $F_{d,g-i}$ is the gas-particle drag force, I_i is the moment of inertia, $\overrightarrow{\omega_i}$ is the rotational velocity, $T_{t,ij}$ is the tangential forces generated torque and $T_{r,ij}$ is the rolling friction torque [32]. Description of each force is given in [32], while the drag force will be explained in Section 2.4.4. By looking at Equations (2.25) and (2.26), it is noticeable that the calculation of the contact force for each particle-particle contact is needed to close the particle linear and rotational momentum equations. The number of particle contacts increases exponentially with particle number and this is why literature addressed only small systems [24,43,47].

2.4.3 The Eulerian-Lagrangian MP-PIC method

Among the Eulerian-Lagrangian approaches, the Multiphase Particle-In-Cell (MP-PIC) is the most novel method, being firstly presented in the 1996 by Andrews and O'Rourke [57]. Computational particle Fluid Dynamics (CPFD) is a software house which implemented the use of MP-PIC in the Barracuda Virtual Reactor® software which implements MP-PIC and groups particle in several clusters, named computational particles or particle clouds, in which all particles share the same properties, namely the same velocity, temperature, composition etc. [49]. Therefore, the number of computational units is diminished with respect to DEM. Unlike

CFD-DEM approach, the MP-PIC approach cannot model each particle-particle contact because several particles are grouped in the already mentioned particle clouds [49]. A particle probability function, $\phi(\vec{x}, \overrightarrow{v_i}, \rho_s, V_i, t)$, describes the dynamics of the particle phase and its time evolution is given by the solution of the following Liouville equation:

$$\frac{\partial \phi}{\partial t} + \nabla \cdot (\phi \overrightarrow{v_i}) + \nabla_{\overrightarrow{v_i}} \cdot \left(\phi \frac{d\overrightarrow{v_i}}{dt} \right) \tag{2.27}$$

The particle acceleration follows the Newton's second law of motion but, unlike the DEM model, the forces exerted by contact are replaced by the inter-particle stress function τ [49]. The acceleration expression is the following:

$$\frac{d\overrightarrow{v_i}}{dt} = D\left(\overrightarrow{v_g} - \overrightarrow{v_s}\right) - \frac{1}{\rho_s}\nabla p + \vec{g} - \frac{1}{\alpha_s \rho_s}\nabla \tau \tag{2.28}$$

where D is an expression of the drag model. The inter-particle stress is a function of the volume fraction and the closing pack volume fraction:

$$\tau = \frac{P_s \alpha_s^{\beta}}{\max\left[\alpha_{s,cp} - \alpha_s, \varepsilon(1 - \alpha_s)\right]} \tag{2.29}$$

where P_s is a constant in unit of pressure, β is a dimensionless constant and ε is a dimensionless constant in the order of 10^{-7} to avoid mathematical singularity. The interparticle stress is not calculated on the Lagrangian unit, but it is calculated on the Eulerian grid in which the particles properties are interpolated. More information on the interpolation strategy is given in [19].

Due to the introduction of the computational particle strategy, MP-PIC employs much less computational resources than the ones needed by CFD-DEM, but it requires that each

computational particle represents a statistically relevant number of real particles. Therefore, MP-PIC is not suitable to capture the small scale behavior due to interparticle contacts such as particle bridges [58]. However, MP-PIC is a powerful tool for fluidized bed equipment modeling and simulation.

2.4.4 The drag models

The momentum exchange between solid and gas due to drag is expressed as a volumetric momentum source for Eulerian-Eulerian models, while for the Eulerian-Lagrangian approaches it is calculated on each particle in the Lagrangian domain and in the Eulerian grid is the sum of the drag forces exerted on each particle. It is possible to express the drag force acting on each particle as follow [49]:

$$F_i = m_i D\left(\overrightarrow{v_g} - \overrightarrow{v_i}\right) \tag{2.30}$$

$$D = C_d \frac{3}{8} \frac{\rho_g}{\rho_s} \frac{\left|\overrightarrow{v_g} - \overrightarrow{v_i}\right|}{r_i} \tag{2.31}$$

Being C_d, the drag coefficient, an expression of the drag models, here the most used drag models are presented with their formulation used by the MP-PIC software Barracuda Virtual Reactor® [50].

The Wen-Yu Drag model

The Wen-Yu drag model was first presented in 1966 [59]. It is suited for mild dense particle systems [50]. According to the Wen-Yu model, the drag coefficient strongly depends on the Reynolds number of the particle.

$$Re_p = \frac{\rho_g d_p \left|\overrightarrow{v_g} - \overrightarrow{v_l}\right|}{\mu_g} \tag{2.32}$$

$$C_d = \begin{cases} \frac{24}{Re_p}\alpha_g^{n_0} & Re_p < 0.5 \\ \frac{24}{Re_p}\alpha_g^{n_0}(c_0 + c_1 Re^{n_1}) & 0.5 \leq Re_p \leq 1000 \\ c_2\alpha_g^{n_0} & Re_p > 1000 \end{cases} \tag{2.33}$$

where:

$$c_0 = 1.0$$
$$c_1 = 0.15$$
$$c_2 = 0.44$$
$$n_0 = -2.65$$
$$n_1 = 0.687$$

This model uses a Stokes drag at low Reynolds, the Schiller-Nauman drag at transition Reynolds [50]. The coefficient used can be adjusted.

The Ergun drag model

The Ergun drag model was developed for high dense particle fluidized bed [60,61]:

$$D = 0.5\left(\frac{c_1\alpha_s}{\alpha_g Re_p} + c_0\right)\frac{\rho_g\left|\overrightarrow{v_g} - \overrightarrow{v_l}\right|}{r_i\rho_s} \tag{2.34}$$

where $c_0 = 1.75$ is the non-linear coefficient and $c_1 = 150$ is the linear coefficient [60]. The coefficient can be adjusted and values of $c_0 = 2$ and $c_1 = 150$ are suggested by the manual of Barracuda Virtual Reactor® [50].

The Wen-Yu/Ergun blend drag model

Gidaspow proposed a drag function blending between the Wen-Yu and the Ergun drag model to have a comprehensive drag function at every possible solid volume fractions [35]. The drag model is expressed as [50]:

$$D = \begin{cases} D_1 & \alpha_s < 0.75\alpha_{s,cp} \\ (D_2 - D_1)\left(\dfrac{\alpha_s - 0.75\alpha_{s,cp}}{0.85\alpha_{s,cp} - 0.75\alpha_{s,cp}}\right) & 0.75\alpha_{s,cp} \leq \alpha_s \leq 0.85\alpha_{s,cp} \\ D_2 & \alpha_s > 0.85\alpha_{s,cp} \end{cases} \quad (2.35)$$

Where D_1 is the Wen-Yu drag model and D_2 is the Ergun drag model [50].

2.5 Method choices

This section will focus on the decision of which methods and models could be applied to each simulation case. However, based upon this section topics, it is possible to make general choices about the methods to be used. Each method choice is made either by testing during the experience of the research group, literature review considerations and available resources.

2.5.1 Multiphase flow method choice

In order to choose the best suited model for multiphase flow the objective of the simulation must be clear along with the quantities that must be measured and evaluated. The scope of this PhD project is to deliver a virtual prototype of an industrial granulator and coater. One of the most important quantities to be measured to assess the performance of granulators or coaters is the quality of binder or coating solution distribution on particles. The coating sprayed on particles in machines such as the Wurster coaters could sensibly increase the particle size and lead to

change in the solid flow treatment. Therefore, binder or coating sprayed are often modeled by considering residence time distribution in the spraying zone [24]. Using TFM, it is possible to add a moisture source to particles that pass through the spraying zone, but then, moisture content is treated as a transport property which can go through convection and diffusion [26]. Moreover, tracking each particle could be important to understand whether or not the coating could have a thin distribution over the batch of pellets and particle and this can be done with Lagrangian methods only [24,43]. In addition to this, difficulties in modeling particle batches with a reasonable particle size distribution led the decision to exclude Eulerian-Eulerian methods to produce a virtual prototype of the coater/granulator. Having excluded the TFM, the choice between CFD-DEM and MP-PIC was mainly driven by the computational performance. In the industrial scenario it is reasonable to assume that particle clouds, which include several particles, can statistically represent, with a good accuracy, the whole particle batch [48]. MP-PIC was chosen as the multiphase model for its better computational performance [32]. Due to its reliability, proven by broader literature and consolidated research, CFD-DEM was considered in first place, but, after testing its computational performance on the available workstations and clusters, it was discarded. In terms of computational performance, Zhong et al. stated that MP-PIC is 50 times faster than CFD-DEM, but it requires twice the TFM simulation time [32]. However, this conclusion was drawn considering a reacting flow [32], but in this work no reaction scheme was implemented and the computational performances could be different. For instance, Liang et al. found out that for simple fluidized bed with no reaction schemes, MP-PIC can be an order of magnitude faster than TFM [62]. In a previous work carried out in our research group 27 seconds of simulation of an industrial fluidized bed were performed in about 14 days using TFM corresponding in a performance of 1 seconds of simulation time calculated in 12

hours of real time [63]. However, work carried out for this thesis demonstrated that using MP-PIC, with a huge work of optimization and improving computational strategies, it is possible to simulate 600 seconds of an operating fluidized bed of similar size in less than half day, reaching the computational performance of about 1 seconds of simulation per minute of real time. Despite the system simulated were different and the computational performance cannot be directly compared, the better computational performance is likely due to the different calculation strategy. In our group MP-PIC calculations were performed using CPFD® Barracuda Virtual Reactor™, a commercial software which allows to parallelize calculations on the GPU CUDA cores [58]. Researchers applied this strategy on CFD-DEM simulation, but, despite promising results, they did not reach such a powerful performance [47]. The major advantages of using CUDA cores to parallelize the Lagrangian domain of a simulation is that architecture of present GPUs allows to have up to 2000 and more CUDA cores which can simultaneously perform calculation in an industry-affordable workstation. On the other hand, the clusters available in our facilities reach up to 12 CPU cores and require a conditioned dedicated room. By switching calculation on GPU's CUDA cores instead of CPU it is possible to earn two orders of magnitude of calculation units without the need of a dedicated IT department. This can improve the pace of virtual prototyping.

2.5.2 Turbulence model choice

As proposed by the developers of the MP-PIC model, LES is the correct turbulence model to be used when addressing the multiphase simulation using MP-PIC [19]. This occurs because particles can be transported by large eddies, thus, their resolution could improve simulations accuracy [19]. However, LES can be computationally demanding and sometimes such accuracy

is not needed. For example, in dealing with single phase gas flow simulations it could be better to use RANS models to lighten simulations. When flow alternates zones near the walls and zones away the walls the perfect choice is the SST k-ω [55]. The SST k-ω model was found to be the best choice to simulate jet flow from orifices [64]. The Wurster coater considered has an air distribution plate such as the one shown in Figure 2.1. The distributor plate is made of several holes with diameter between 1 mm and 4 mm. Air flow crossing this plate results in several jets and this fact led the choice of the turbulent model to the SST k-ω model when dealing with the distributor plate.

2.5.3 Drag model selection

Fluidized bed and especially the ones used in batch granulation and coating alternates zones of high particle volume fractions and zones with low particle volume fractions. As mentioned in the drag model explanation the Wen-Yu Ergun blend drag model is the best choice for such cases.

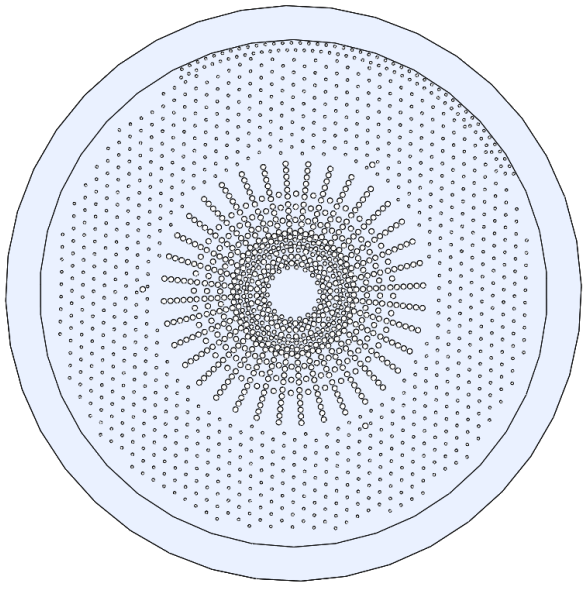

Figure 2.1 Air distribution plate used in ARIA 120 Wurster coater configuration.

2.6 Validation of the MP-PIC software CPFD® Barracuda Virtual Reactor®

As mentioned, MP-PIC is a novel method for multiphase flow simulation and it is implemented in the software by CPFD®, Barracuda Virtual Reactor® (Barracuda VR). Therefore, it is not a mature method as the other multiphase methods and it needs to be validated. Literature lacks good validation studies and the fast pace of development of the software is the cause that validation literature gets outdated very fast. A critical validation study was performed by Liang et al. in 2014 finding that Barracuda VR v15.1 predicts a higher bubble possibility to the wall profile with respect to TFM and experimental data [62]. In a more recent work (2016), Wang et al. stated that CPFD method can be useful to investigate the gas-solid flow in a Wurster fluidized bed [48]. However, they do not mention which release of Barracuda VR they used. For this reason, validation of the MP-PIC method and evaluation of its performance was pursued.

2.6.1 Description of the reference data and methods

The evaluation of the particle paths resolution was found to be the most useful for this purpose. Li et al. used a positron emission particle tracking (PEPT) technique to track the particles in a Wurster coater and performed CFD-DEM simulation of the same machine as described before in Section 1.3.1 [14,24]. Their works are used to compare MP-PIC results and to draw some useful considerations about this method. As mentioned, Li et al. had not applied any model for coating, but they measured the cycle time distribution (CTD), i.e. the distribution of the time for a particle to complete an entire cycle in the whole machine, and the residence time distribution

in the spray zone (RTD), i.e. the distribution of the residence time of each particle in the spray zone depicted in Figure 2.2 [24].

2.6.2 Software and hardaware

Barracuda VR v.17.0.03 was used to perform MP-PIC calculations. Parallelization of simulation was performed on standard office workstation equipped with an NVIDIA GeForce GT 640 with 384 CUDA cores.

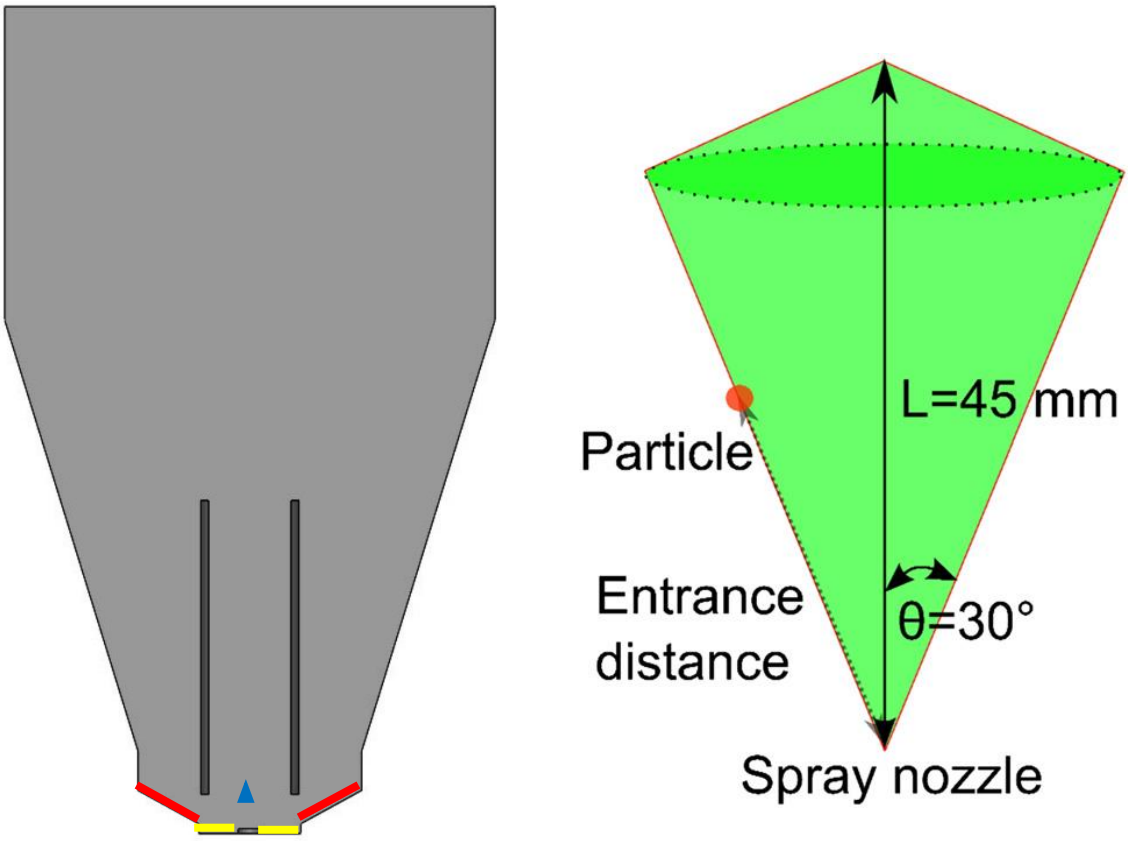

Figure 2.2 LHS: Geometrical 3D model of the Wurster coater used in the validation study. RHS: representation of the spray zone by Li et al. [24]

2.6.3 Geometry and boundary conditions

The Wurster coater considered has a maximum diameter of 250 mm was 250 mm and its total height is 417 mm. Detailed description of the geometry is given in [14]. In Figure 2.2 the 3D geometrical model is presented. The bottom of the machine, is divided in two parts. The central flat part, (highlighted in yellow in Figure 2.2) supplies the 55% of the total fluidization flow rate while the outer conical shaped part (highlighted in red in Figure 2.2) supplies 45% of the total flow rate. The mentioned total flow rate is 73.3 m^3/h. The atomization flow rate of 3.5 m^3/h enters from a small central inlet located 3 mm above the bottom plate (highlighted with a blue triangle in Figure 2.2). 200 g of particles with 1749 μm diameter and a density of 1420 kg/m^3 are fed in the machine as initial condition. No other particle feeds are present. The air supplied has a density equal to 1.204 kg/m3 and a viscosity equal to 18.37 μPa s.

2.6.4 Grid and time sensitivity study and performance evaluation

Grid size was limited by upper and lower constraints, so the grid sensitivity study was not performed. The Eulerian cell size cannot be larger than the one used because otherwise it is not possible to have a good representation of the geometry. On the other hand, each Eulerian cell must contain at least one computational particle. Due to the small size of the system compared to the size of particles allowable grid size did not change the simulation. However, computational particles have a small number of real particles and this does not fall in the best practice of Barracuda VR [58]. The time step chosen must satisfy the Courant-Friedrichs-Lewy condition (CFL) since the method used by Barracuda VR is explicit [17,50]. Barracuda VR can automatically adjust the time step to fall within certain values for the CFL [50]. In this case, the

time step varied around 1×10^{-5} s. Similarly to Li et al. [24], 25 s of simulation are sufficient for having independent results for the cumulative distribution of the cycle time and much less time is needed to have a steady approximation of the residence time distribution in the spray zone. The available combination of hardware and software presented in Section 2.6.2 was able to simulate 1 s of physical time in about 5 h, while CFD-DEM model employed by Li et al. required 12 h on 32 CPUs. It must be noticed that the hardware configuration used in this work can be provided in every office while the architecture of 32 CPUs used by Li et al. requires a dedicated cluster.

2.6.5 Validation results

Average volume fraction

To show the most probable disposition of particles within the Wurster apparatus the average particle volume fraction was measured and compared with CFD-DEM by Li et al [24]. This comparison is presented in Figure 2.3. While there is a good agreement in the shape of the horizontal transport region and of the fountain region, the latter one height is overestimated. However, the main differences occur in the Wurster tube. In the MP-PIC simulation particles are more concentrated in the central part of the Wurster tube and less concentrated near the Wurster tube walls. In the CFD-DEM simulation there is an opposite behavior [24]. This fact may cause an overestimation of particles presence in the spray zone. This behavior may be caused by the upper and lower constraints that had to be faced during the Eulerian grid construction. With such a difficult grid construction turbulence may not be well captured.

Velocity investigation

The fact that the pinnacle of particles in the fountain region reaches a higher point could be explained by looking at the average velocity profile in the Wurster apparatus. Air velocity determines the force at which particles are entrained according to the drag model. The average vertical velocity profile is shown in Figure 2.4. The average fluid vertical velocity remains unexpectedly confined in the central region at the exit of the Wurster tube and this might cause an underestimation of the fluid velocity in the outer part of the fountain zone and in the downbed region while in the Wurster tube the fluid velocity is overestimated. As drag force is proportional to the difference between fluid velocity and particle velocity a wrong estimation of fluid velocity could lead to a wrong estimation of particle velocity. It is expected that particles rise faster in

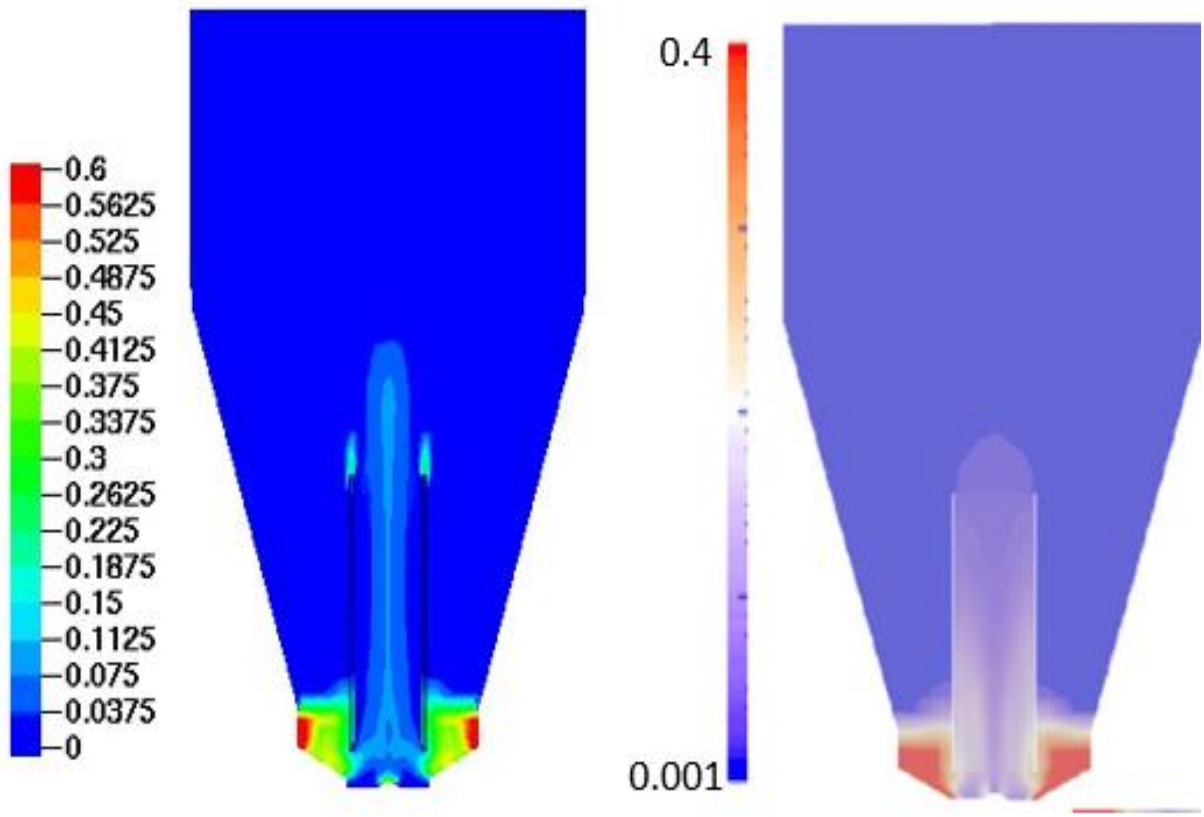

Figure 2.3 LHS: Comparison of the average particle volume fraction between MP-PIC results. RHS: CFD-DEM results by Li et al. [24].

the Wurster tube because they are accelerated by a faster fluid flow and fall faster in the downbed region because they are decelerated by a slower fluid flow. The comparison of particles velocity calculated with MP-PIC with the data retrieved in the work of Li et al. confirms these forewords [24]. In fact, as can be seen in Figure 2.5, particle velocity obtained with the MP-PIC simulation is always higher than the experimental data, both inside the Wurster tube (radial distance less than 22 mm) where particles are rising and in the downbed region where particles are falling. However, the zone close to the wall show a deceleration of particles which is present in both the experiments and CFD-DEM simulations, but the MP-PIC simulation overestimates this deceleration, probably because of bad near to wall resolution, a known issue of CPFD approach [62]. In the center part of the Wurster tube, i.e. where the atomization flow rate is placed, both MP-PIC and CFD-DEM largely overestimate the vertical particle velocity, probably because there is a bad resolution of the high velocity flow due to the presence of the atomizer. In the outer part of the Wurster tube (between 15 mm and 20 mm of radial distance)

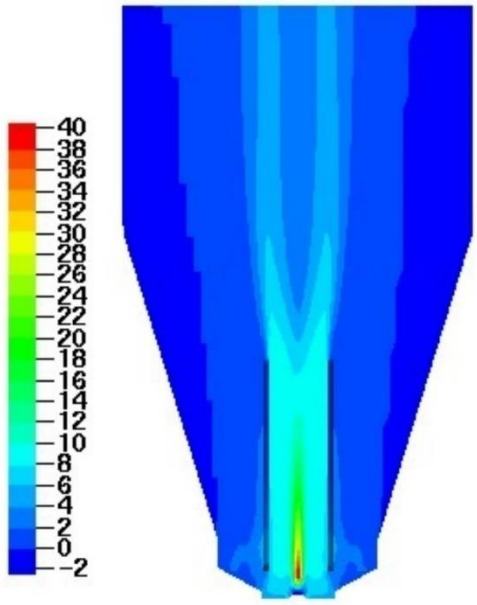

Figure 2.4 Fluid vertical velocity in the Wurster coater, expressed in m/s.

MP-PIC overestimates particle velocity but the trend is more consistent to the experimental data than CFD-DEM profile is. Overestimation of velocity is probably due to a wrong drag force definition. Researchers have proposed to adjust the drag model by a scaling factor of 0.6 [48]. This could improve results when particles have a higher velocity in rising the Wurster tube, but reducing in such a way the drag coefficient could worsen the particle downward velocity estimation because in the downbed region particles are decelerated by the fluid flow.

Cycle time distribution

Since particle vertical velocity is overpredicted in any part of the machine, faster cycle should occur as well as shorter particle residence time per cycle. As shown in Figure 2.6 the cycle time

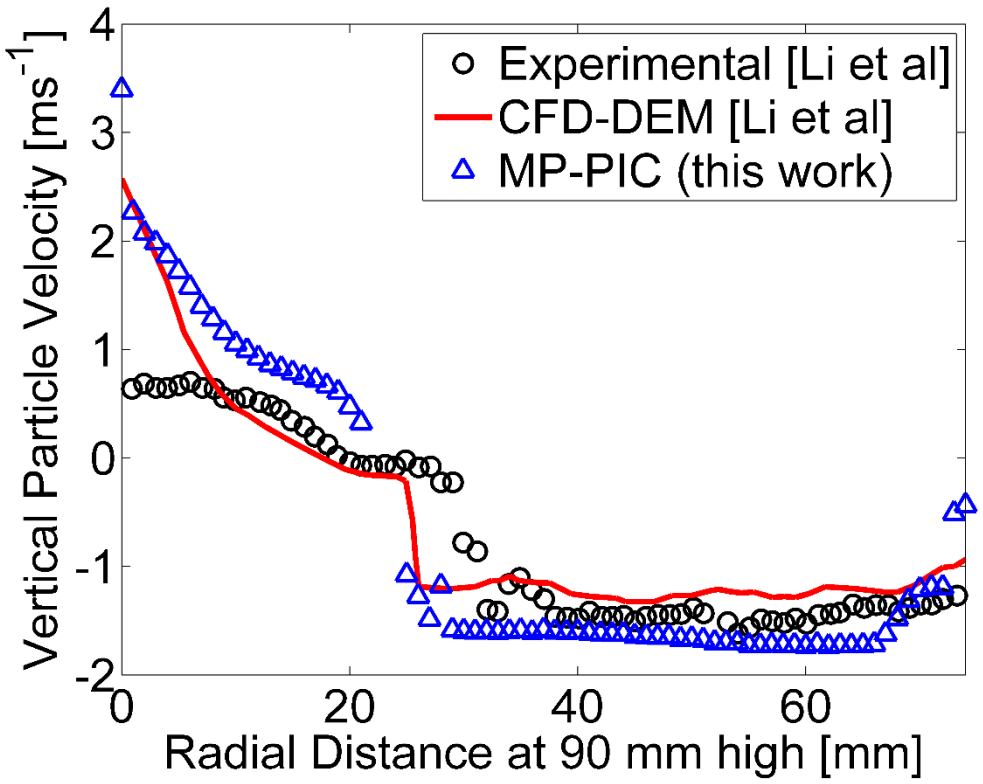

Figure 2.5 Vertical particle velocity at height of 90 mm against the radial distance from the center. Comparison between MP-PIC, CFD-DEM and experimental data.

distribution for the MP-PIC is narrower than the experimental and CFD-DEM calculated distributions. The peak of the distribution is at a slightly lower time and the percentage of particle cycles decreases faster with the cycle time for the MP-PIC calculations.

Residence time distribution in the spray zone

Faster cycle time distribution means that the residence time in the spray zone for each particle cycle should be lower. In fact, this prediction is confirmed by the comparison of the residence time distribution in the spray zone between MP-PIC and CFD-DEM calculations, as shown in Figure 2.7. Despite the peak value of the residence time is approximately the same, it has a much larger value for the percentage of particle cycles. In the figure, it is also shown a comparison with smaller particles residence time distribution in the spray zone calculated with CFD-DEM

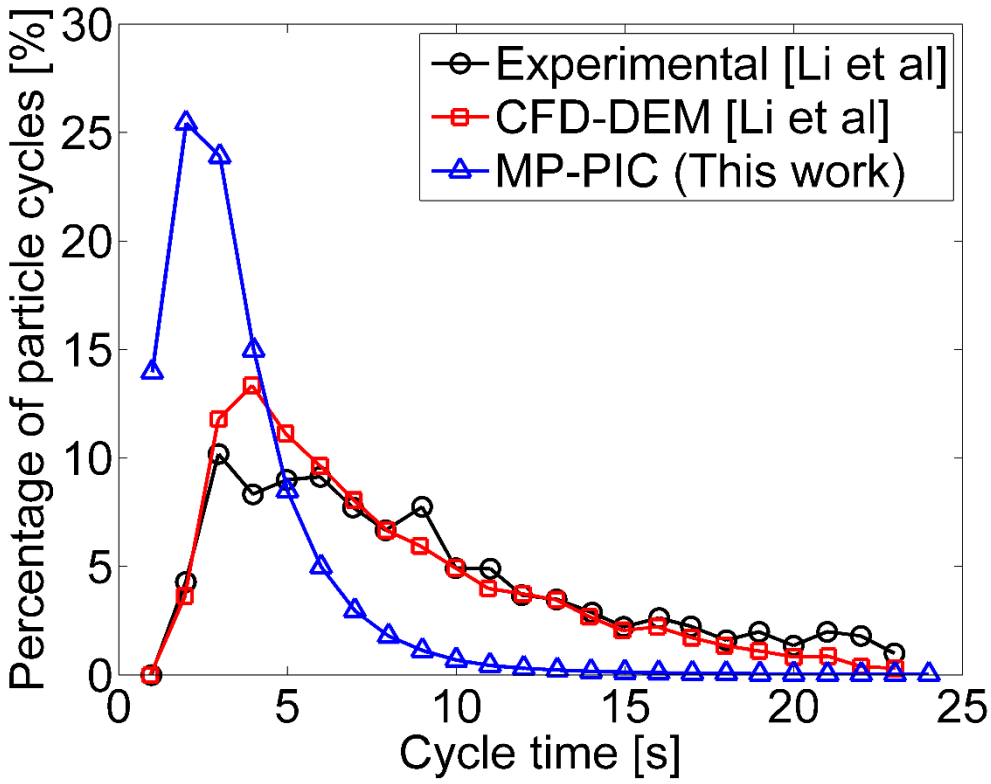

Figure 2.6 Cycle time distribution curve comparison between MP-PIC, CFD-DEM and experimental data

by Li et al. [24], showing that MP-PIC could overestimate the performance of the Wurster coater as if smaller particles are used.

2.6.6 Final consideration on validation study

MP-PIC overestimates the performance of the Wurster coater. A proposed scaling factor for the drag model could mitigate this overestimation, but the literature lacks of strong motivation for the use of a certain value [48]. Furthermore, the value proposed by Wang et al. for the scaling factor of the drag model could be dependent on the specific case on which it is based. In this work it has been chosen to not add any scaling factor, but consideration about performance will be made only in relative values rather than absolute values, i.e. only similar cases will be

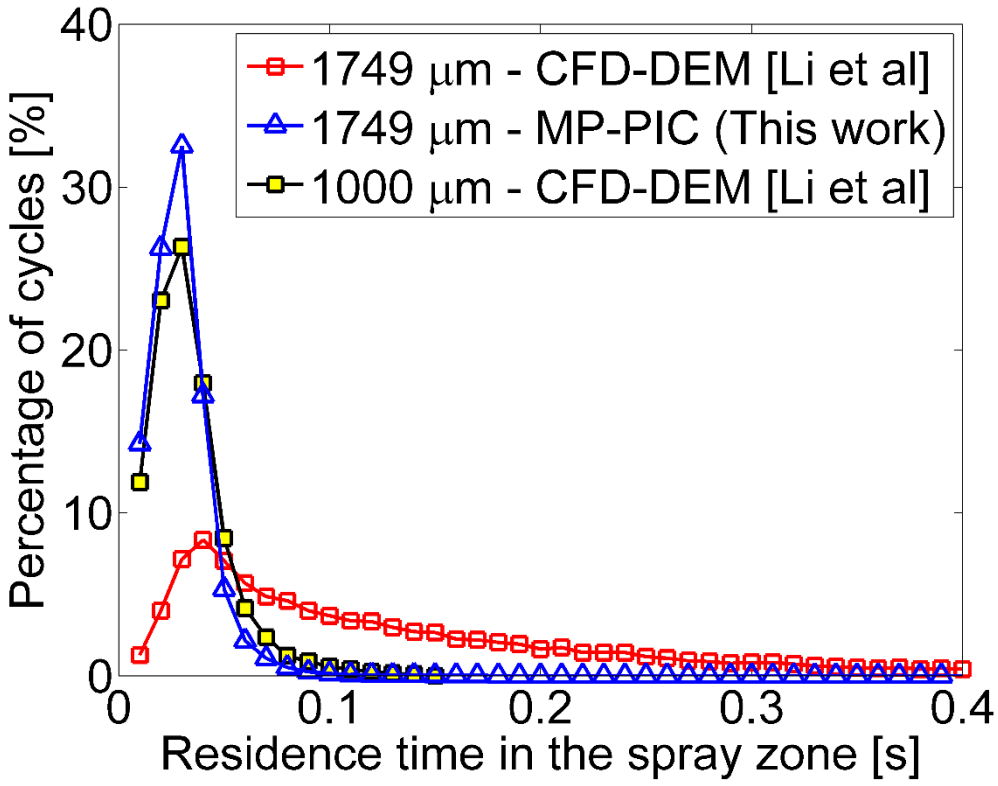

Figure 2.7 Calculated residence time distribution in the spray zone comparison between MP-PIC and CFD-DEM.

performed and compare among each other. Moreover, it is believed that the major error source in this validation study consists in having small Eulerian cells compared to the particle size involved as explained in Section 2.6.4. The statistical approach used by MP-PIC could suffer from having particle clouds with a small number of real particles. However, MP-PIC will be applied to a much larger equipment and this should eliminate this statistical error.

Section 3
Case study: a pharmaceutical fluid bed equipment

3.1 IMA's ARIA equipment

IMA S.p.A produces a multipurpose equipment line named ARIA [12]. It allows drying, granulation and pellet coating. The design of the machine was made to allow the through-the-wall installation as shown in Figure 3.1. The line ARIA has several sizes named by adding a number to the name. For instance, Figure 3.1 shows the ARIA 600 equipment.

Figure 3.1 An example of an ARIA equipment, ARIA 600 [11]. The light blue plane represents the wall.

The different size configurations are customizable as shown in Figure 3.2 but fixed configurations are proposed in the company portfolio [12].

The machine is composed by different parts [12]. In the bottom is placed the bowl, also referred as base or basement, where the main air inlet is placed. The bowl has a concave floor to ease the cleaning. Above the bowl the basket is placed. The basket has a conical shape and can be replaced to switch between granulation and coating batch processes. The basket connects the basement to the main chamber where usually the product loses its inertia and fall back to the basket. The main chamber could have several removable tight proof steel windows which can be replaced by probe or atomizing nozzle units and they can be removed during standard maintenance cleaning. On the top of the chamber, a plate allows positioning of the filters which could be of different types (e.g. bag filters or star plated filters). The cap of the equipment has a large outlet pipe connected to the fan which provides the main fluidization air flow.

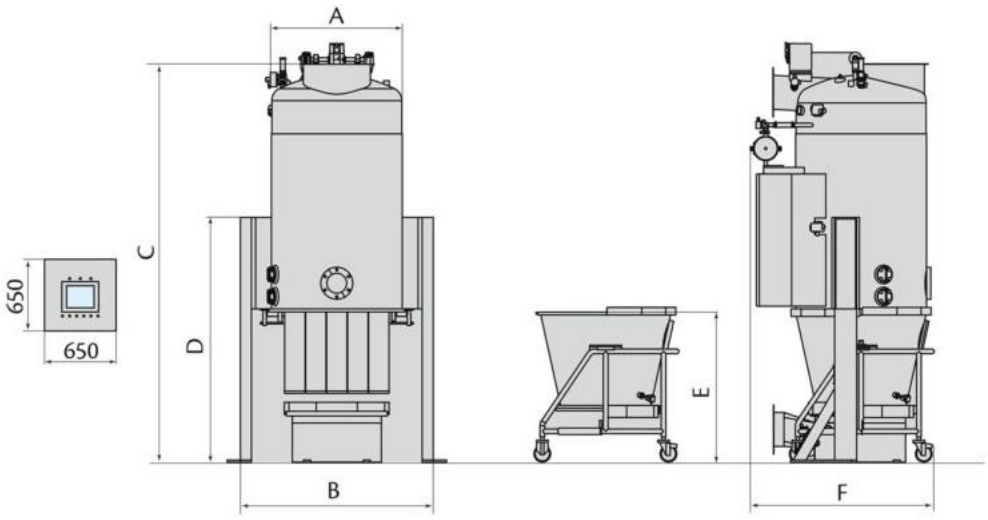

Figure 3.2 ARIA equipment's layout. Letters represent customizable sizes [11].

3.1.1 Granulation and coating configurations

As mentioned before, the basket allows changing the machine configuration to perform granulation or coating. In case of granulation the basket conical shape starts immediately from the bowl and the bottom of the basket holds the product support grid. As granulation operations process fine powders the grid has a fine mesh. The granulation is performed with a top spray configuration; therefore, the atomizer is placed in a chamber window, pointing the basket.

The coating configuration allows for a Wurster process [14]. The basket starts with a small cylindrical part and then it has the mentioned conical shape where the Wurster tube is placed. Between these two parts an air distribution plate is placed right below the product support grid. The plate is designed to direct the upstream flow in the inner part of the basket where the Wurster tube forces the particles to rise with a spouted bed like flow. The Wurster tube is placed at a distance from the air distribution plate which allows the horizontal transport of pellets from the external part of the machine. The vertical position of the Wurster tube can be easily changed by a gear which occupies a fraction of the down bed region. The coating atomizing nozzle is placed in the center of the air distribution plate and it points upward.

3.2 ARIA 120 3D modeling

IMA's laboratory holds an ARIA 120 unit. It is a pilot scale unit with a batch size around 50 kg. This equipment was available for testing both granulation and coating. According to Figure 3.2, the total height of the machine (C value) is 2790 mm the diameter of the product chamber is

700 mm (A value). A 3D model of the machine was made using 3D CAD software SolidWorks for both granulation configuration and Wurster coater configuration.

3.2.1 Granulation configuration

The granulation configuration is also known as top spray configuration because the binder is sprayed from the top. The 3D model of ARIA 120 in granulation configuration is shown in Figure 3.3. The figure shows the main dimension (approximated). To allow CFD simulations only the fluid domain was modeled and not the real metal walls. The model was built in such a way to lighten the simulations, so it has the following simplifications:

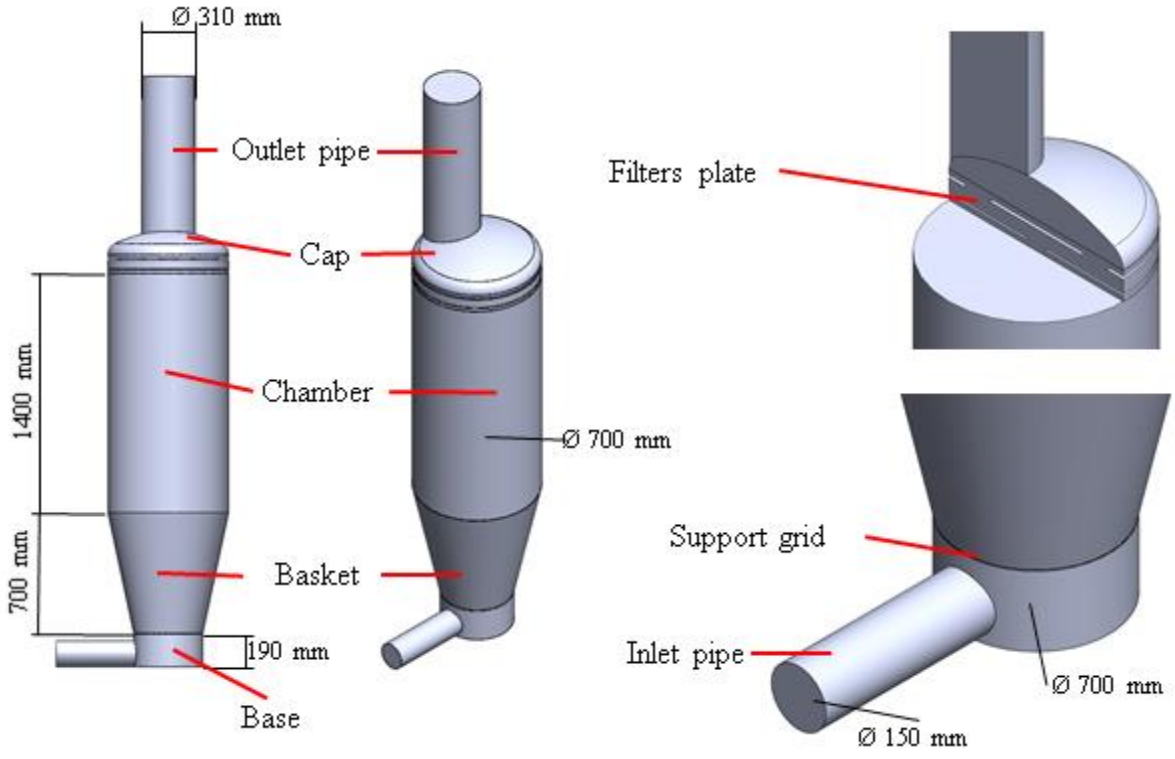

Figure 3.3 3D CAD model of ARIA 120 unit in granulation configuration.

- The inlet pipe is straightly connected to the base without the diverging rectangular junction.
- The inlet and outlet pipes are elongated to outdistance the numerical boundary conditions as CFD best practices.
- Base floor is not concave but flat.
- All small features such as bolts and windows are not considered.
- Filters are not considered.

Since the grid holes' dimension is too small, the grid is modeled as a porous medium as described in Section 2.3. This is the strongest simplification of the machine so far, but this model strategy is due to make simulations feasible.

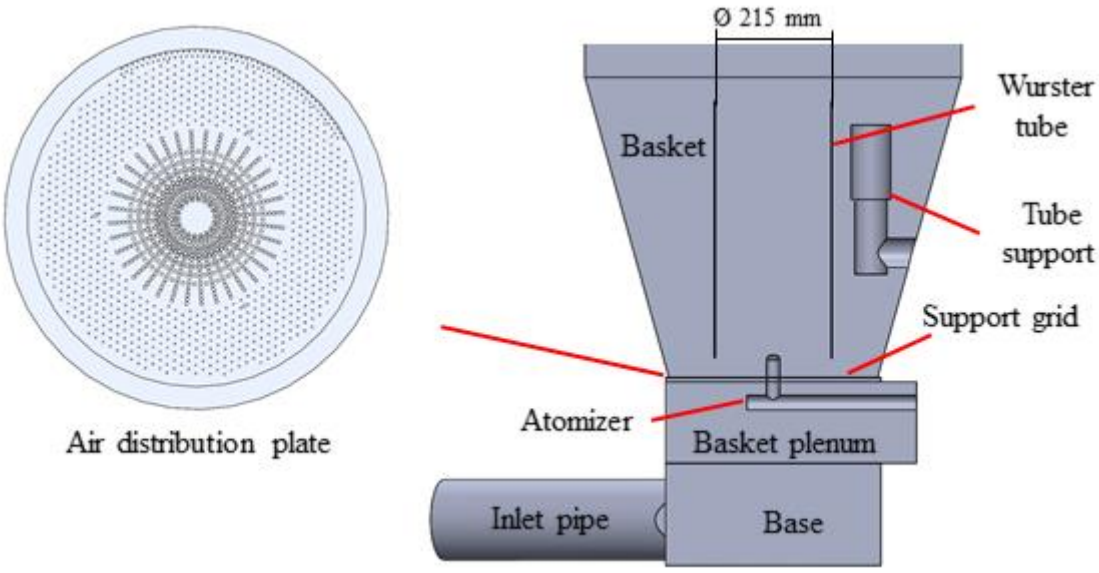

Figure 3.4 3D CAD model of the basket of ARIA 120 unit in Wurster coater configuration. Lateral section view.

3.2.2 Wurster coater configuration

It is possible to change the product basket to switch from the granulation configuration to the Wurster coater configuration, also called bottom spray configuration. The 3D CAD model of the basket is given in Figure 3.4. With respect to the granulation configuration the basket has an additional plenum directly open to the basement. The atomizer tube is placed in this plenum which is separated from the product container by the air distribution plate and the product support grid. The atomizer vertically crosses the air distribution plate and the product support grid to enter in the basket axial direction. Atomizer points inside the Wurster tube which has a diameter equal to 215 mm and a height equal to 478 mm. The Wurster tube is supported by a tool which allows to vertically move it to regulate the partition height, i.e. the space between the Wurster tube and the support grid. The air distribution plate has several holes which allow less air flow resistance in the central part to develop the spouted fluid bed typical of the Wurster process. In the same way as granulation configuration, the support grid is not 3D modeled due to the small size of the holes.

3.3 Preliminary experiments in granulation configuration

To assess the knowledge of the ARIA 120 machine fluid dynamic a preliminary experiment was performed. This experiment aims to evaluate pressure drops for having a quantitative analysis to be compared with simulations. The equipment was set in granulation configuration and experiments were conducted without a product batch. This allow to easily tune simulations to the values obtained by experiments. A set of five experiment was performed by changing the

Table 3.1 List of experiments mass flow rates. In brackets, the uncertainty of the measurements.

Experiment number	Nominal Mass flow rate [Nm^3/h]	Mass flow rate [g/s]
1	1000	356.6(12)
2	800	285.4(07)
3	600	214.1(07)
4	400	142.8(07)
5	200	71.1(07)

input mass flow rate in the machine as listed in Table 3.1. The ARIA 120 controller allows to set the mass flow rate in terms of Nm^3/h measuring the real value in the machine. There are several pressure sensors, but for this study, only the pressure sensor in the base and the pressure sensor in the chamber were considered. These two sensors give the pressure drop of support grid and the product batch (during normal operations, not for this study since there is no product batch). The outcome of the two sensors is given in Table 3.1. It comes immediately to attention that static pressure drops are negative (even if the absolute value is small) in the first three cases. This is a warning signal especially because the product support grid should bring its own pressure drop which could be higher. The pressure drop due to the support grid was measured in previous experiments (see [63]) resulting in the following constants for equation (2.15) and thickness:

$$\begin{aligned} {}^{1}/_{\alpha} &= 5.809\times10^{8}\ \mathrm{m^{-2}} \\ C_2 &= 4979.7\ \mathrm{m^{-1}} \\ \Delta s &= 0.003\ \mathrm{m} \end{aligned} \tag{3.1}$$

Thus, equation (2.15) becomes the following for the considered grid:

Table 3.2 Relative pressure in base and chamber for the five experiments. In brackets, the uncertainty of the measurements.

Experiment number	Nominal Mass flow rate [Nm^3/h]	Base relative pressure [Pa]	Chamber relative pressure [Pa]	Static pressure drops [Pa]
1	1000	-938(15)	-907(21)	-31(14)
2	800	-678(16)	-666(14)	-13(15)
3	600	-472(6)	-457(7)	-15(9)
4	400	-287(6)	-291(2)	4(6)
5	200	-176(4)	-185(2)	9(5)

According to equation (3.2) the pressure drop due to the support grid were calculated for the five conditions and reported in Table 3.3. As can be drawn from these results, static pressure drop is significantly lower than the expected value which is produced by the support grid. This is an important finding because the company used to rely on this pressure drop data to evaluate the behavior of the fluidized bed inside the machine. Therefore, this value cannot be reliable. To double check this statement, a rule of thumb check using Bernoulli's equation was performed:

$$P_{drop} = (P_b - P_c) + \frac{\rho v^2|_b - \rho v^2|_c}{2} + g(\rho z|_b - \rho z|_c) > 0 \qquad (3.3)$$

Despite Bernoulli's equation is valid only for fully developed pipe flow (which cannot be applied to the equipment), this check is worth the effort to further investigate the phenomenon. Assuming the pressure measured in the basement and in the product chamber and the velocities derived from the sections of the two parts, the total pressure drops calculated according to Bernoulli's equation are negative as shown in Table 3.3. Therefore, some assumptions must be wrong, and, in the following section, a possible explanation will be given.

Table 3.3 Pressure drop expected due to grid and pressure drop calculated using Bernoulli's Equation for the five experiments.

Experiment number	Grid expected pressure drop [Pa]	Bernoulli calculated total pressure drop [Pa]
1	160	-37
2	118	-20
3	81	-23
4	49	-5
5	22	-1

3.3.1 Interpreting negative pressure drop

Pressure drop must be positive and finding what could be wrong is of primary importance. Calibration of the pressure sensors was thought to be the primary reason but, after recalibration experiments gave the same results. Nonetheless, results shown before are the ones obtained from experiments performed after recalibration. The following step was to evaluate the pressure sensor positioning. The pressure sensor in the product chamber is placed where flow is mainly vertical and likely to be fully developed at least when the product is not present. Relying on this pressure sensor is acceptable. It is not possible to draw the same conclusion for the pressure sensor placed in the basement. Air flow through a horizontal pipe and then it expands in the basement and macroscopically curve to the vertical to going through the support grid. Thus, this behavior cause turbulences which are hardly predictable. Here the flow has not a known direction and it is for sure not well developed. Punctual behavior of the flow is unpredictable, thus, even the response of the pressure sensor. Moreover, the pressure sensor is positioned on the side wall of the basement right aside the inlet pipe hole. Therefore, it is likely that the sensor is placed in a low-pressure zone measuring an unrealistic value of pressure.

3.3.2 Verifying low pressure zone using CFD

The conclusions drawn in the previous section was validated through CFD analysis. The experiment validate was the first one, with a nominal air flow rate of 1000 Nm^3/h. The software used is ANSYS Fluent [53]. Geometry used is the one described in section 3.2 and the mesh for the test has around 1 million elements. Simulation is steady and the solver is pressure based. Flow is viscous and incompressible. Air density and viscosity are retrieved from general handbook [65]. Turbulence is modelled with a realizable $k-\varepsilon$ model using standard wall functions. This was a qualitative test to have a clear insight on what happened in the basement. To do so a view to the streamline of airflows is displayed in Figure 3.5. As predicted, the flow in the basement is not well developed, thus, fluctuations in pressure are unavoidable. To quantify these fluctuations, it is worth to have a look at the pressure contour plot on the wall of the

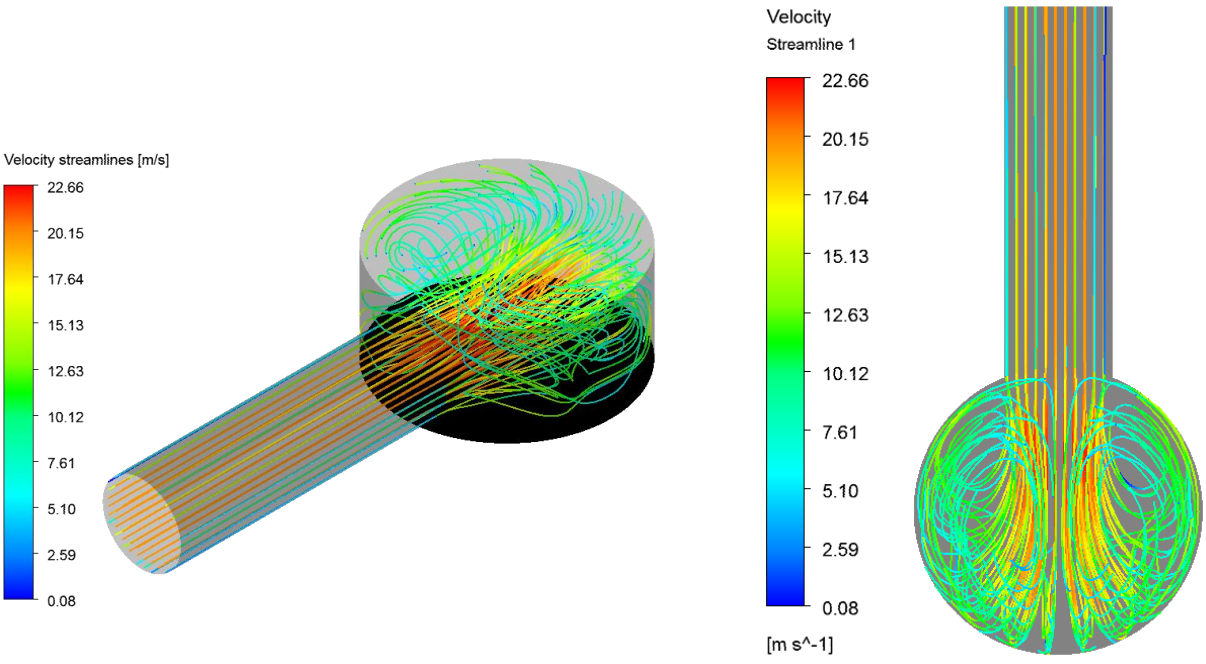

Figure 3.5 Velocity streamlines in the basement. LHS: Isometric view. RHS: top view.

basement. In Figure 3.6 it is possible to appreciate on which extent the static pressure varies in the basement: minimum and maximum pressure values differ by 350 Pa. Figure 3.6 also show the approximate position of the pressure sensor on the side wall of the basement. It is easy to understand that the pressure sensor lies in a low-pressure zone as expected, since it lies aside a fast jet flow. Therefore, measurements of pressure with this sensor will be underestimated. Since approximations made were large (especially the one on basement bottom shape, see Section 3.2), it is not possible to derivate a value to recalibrate the pressure sensor also because turbulence plays a major role and it is hardly predictable for the whole set of operating conditions. Moreover, simplification made in the 3D model, such as the flat basement and the

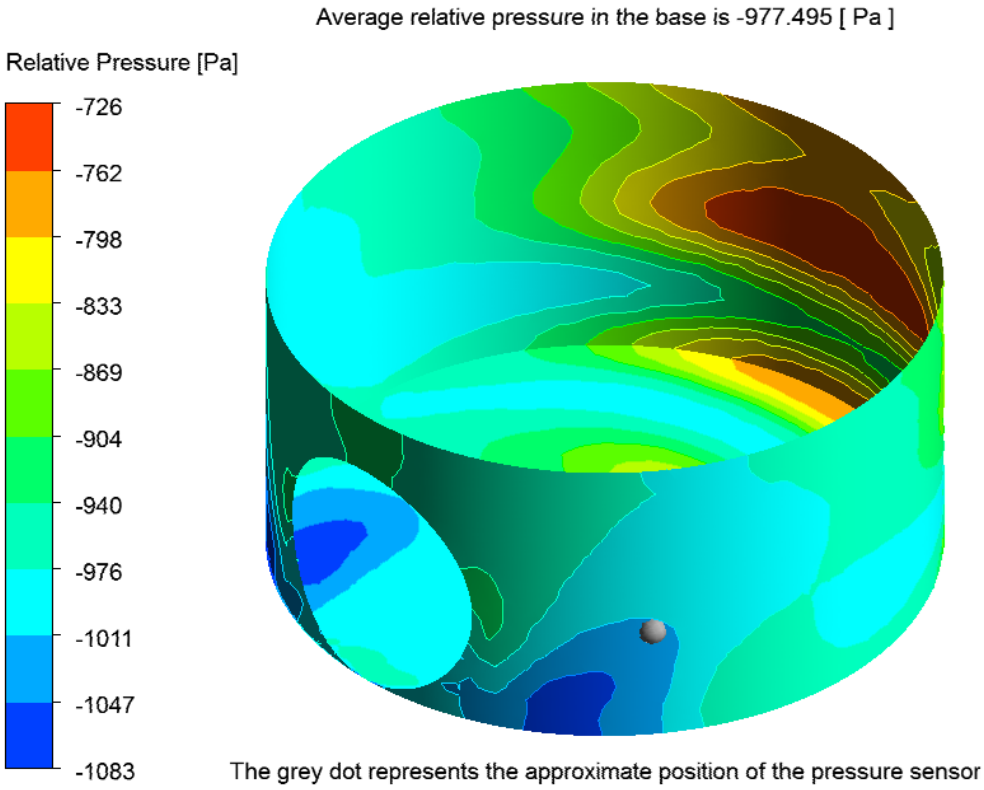

Figure 3.6 Pressure contour plot on the wall of the basement.

Table 3.4 Experiments performed on ARIA120 in coating configuration.

Experiment number	Spraying flow rate [ml/min]	Fluidization air flow [Nm^3/h]	Mass Yield [%]
1	175	800	98.58
2	200	800	96.15
3	150	800	99.07
4	200	1000	98.80
5	200	900	98.82
6	175	900	98.73
7	150	900	97.71
8	175	1000	97.66
9	150	1000	98.84

connection between the inlet pipe and the basement could affect the prediction of a recalibration factor for this pressure sensor. The best solution would be to add several pressure sensors in the basement and take the average of their measurements as the pressure in the basement.

3.4 Application of MP-PIC to ARIA120 in Wurster configuration

3.4.1 The available set of real experiments

Due to the availability of a set of experiments previously performed in IMA S.p.A. [66], it was possible to test the use of Barracuda VR to extend the knowledge of the Wurster process in the ARIA120 equipment. The experiments were performed using a batch of mass 50 kg of glucose pellets with a density equal to 680 kg/m^3. The pellets had a diameter between 0.85 mm and 1 mm with the particle size distribution shown in Figure 3.7. The Wurster tube was positioned at 35 mm from the support grid. From the atomizer a water solution of 10.4 % in methocel, a

common coating agent [67], was sprayed at three different rates. Three different air flow rates were tested for a total of 9 experiments summarized in Table 3.4. The fluidization air flow had a temperature $T = 70$ °C. The coating solution was sprayed for enough time to reach a total amount of methocel of 5 kg. Then, after a short phase to dry out the eventually remained water, the batch is discharged and weighted. The expected mass of the batch at this point is 55 kg. The yield is measured as follow:

$$Y_{mass} = \frac{m_{batch,f}}{m_{batch,i} + m_{meth}} = \frac{m_{batch,f}}{55\ \text{kg}} \tag{3.4}$$

Losses of mass in the batch could be caused by drops of coating solution that dry before hitting the pellets or pellets that stick to each other and are, therefore, not available for further use.

3.4.2 Virtual replication of real experiments with Barracuda VR

These experiments are virtually replicated in Barracuda VR. However, models for measuring the mass losses in the Wurster coater configuration of ARIA120 equipment are missing, thus,

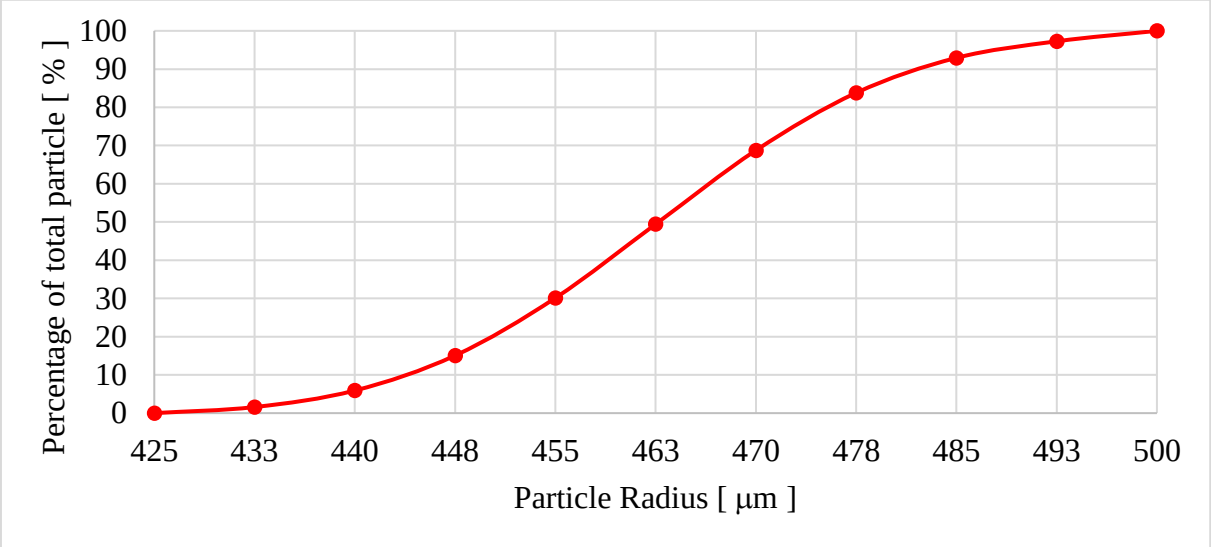

Figure 3.7 Cumulative particle size distribution of used glucose pellets

this set of virtual experiments aims to enhance the knowledge about the coating by adding an important prediction in the coating phase: the coating distribution uniformity. It is trivial to understand that in a batch of pellets reaching a coating distribution as much narrow as possible is of a major importance. Measuring the mass yield could be a quality reference measurement for the process because it is easily physically performed. On the other hand, it is impossible to measure for each pellet how much coating is deposited, thus, virtual experiments allow to extend the available data to make decision of which set of operating conditions is better for the quality of the product. Since real experiments and virtual experiments measure different quantities, these data will not be used as validation support. However, whether some issues are spotted, further investigation will be provided.

3.4.3 Part of the ARIA 120 to be modeled

To catch fluid dynamics of all holes of the air distribution plate a very thin Eulerian mesh must be generated. Unfortunately, the Eulerian mesh generation method available in Barracuda VR allows to only generate cartesian meshes and this means that all mesh elements which share a coordinate with an element in the plate must have the same size. The air distribution plate has holes in the size between 1 mm and 4 mm and to catch the fluid flow inside each of them much smaller Eulerian grid elements are needed. The size of pellets is around 1 mm, but the computational particles cannot be larger of the Eulerian grid elements for reasons explained in Section 2.6.5. Being the plate composed by zones of different holes densities, modeling the plate using the porous formulation would still require very small Eulerian grid elements. Therefore, the plate cannot be modeled inside the Barracuda VR environment. The solution is to model only the basket and the product chamber, avoiding the basement plenum, the plate or the support

grid. The effect of the plate will be simulated by different flow boundary condition at the base of the basket., i.e., on central boundary condition will simulate the mass flow rate right under the Wurster tube and an annular external boundary condition will simulate the mass flow rate under the downbed region. Given that the total mass flow rate is either 800 Nm3/h, 900 Nm3/h or 1000 Nm3/h, the amount of air flow passing in the central part and in the external part of the air distribution plate must be determined.

3.4.4 Mass flow ratio determination

Determination of the ratio between the two mass flow rates will be performed using air single-phase simulation with CFD software STAR-CCM+ and Ansys Fluent. Simulating the whole machine with the physical plate and all its holes was considered the best option to get better results. However, due to the high number of holes in the air distribution plate, this approach resulted in a very high computational cost, so it was decided to model either the plate as a porous mean or considering only an axial symmetric part of the machine.

Porous formulation derivation for the plate and simulation of the whole machine

Modeling the air distribution plate as a porous mean, needs that the viscous and dynamic coefficients for equation (2.15) must be determined. Since the air distribution plate has a non-regular holes pattern, a pair of coefficients for each recognizable regular pattern must be found. The plate has six concentric named from 1 to 5 for the internal parts and "ext" for the external part. This division is shown in Figure 3.8. The external part has a triangular pattern (the smaller holes that are visible on the left hand side of Figure 3.8 are closed in the machine) and it was simulated using only a small rectangular part (see Figure 3.9) and applying the symmetry conditions in Ansys Fluent. The internal parts were simulated using only a 20 degrees sector each and applying the periodic boundary conditions in STAR-CCM+. Several simulations were performed for different superficial velocities as inlet boundary condition for each part. This set of superficial velocities includes also the typical superficial velocities that pass through the plate

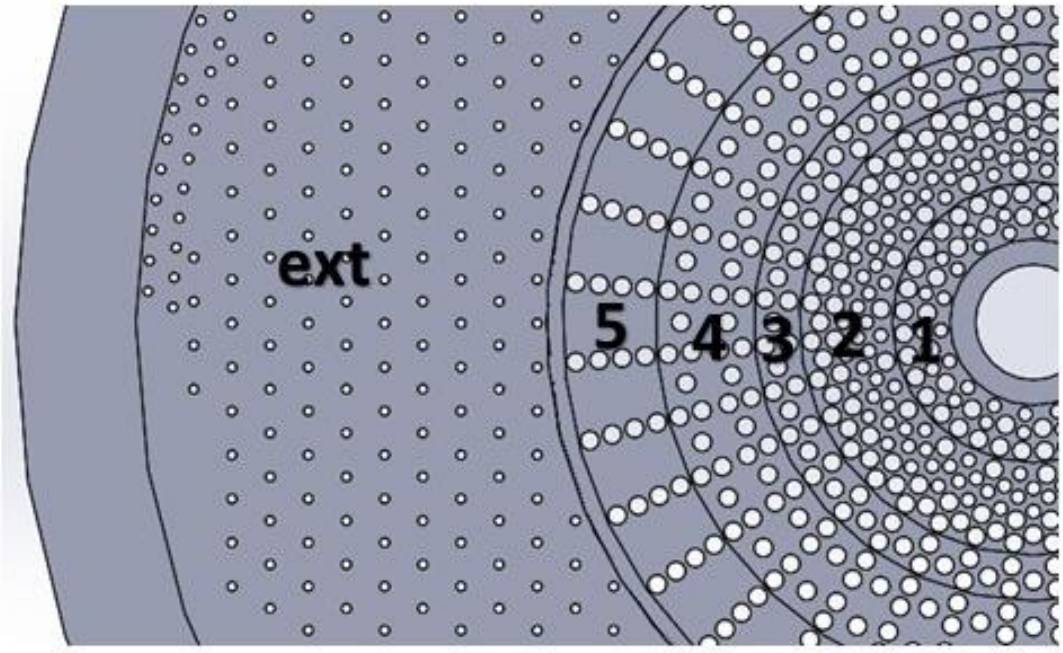

Figure 3.8 Division of the air distribution plate into six different part for porous formulation derivation.

during the normal operation of the ARIA120 in Wurster configuration. The used turbulent modeling for these simulations is the SST k-ω. The air viscosity and density were determined for air at 70 °C and 1 bar using correlations retrieved in literature [65]. Since the same air conditions will be used in the machine simulation, equation (2.15) is no longer dependent on viscosity and density of the fluid and it can be written as follow:

$$\frac{\Delta P}{\Delta s} = Av^2 + Bv \tag{3.5}$$

Therefore, the plot of linear pressure drop against the superficial velocity should results in a parable starting from the origyn. This plot is shown in Figure 3.10 for the internal parts only. Points for the part 5 are out of bound for visualization purposes. A second order polynomial fit of the data gave accurate results which are summarized in Table 3.5. The A and B coefficients

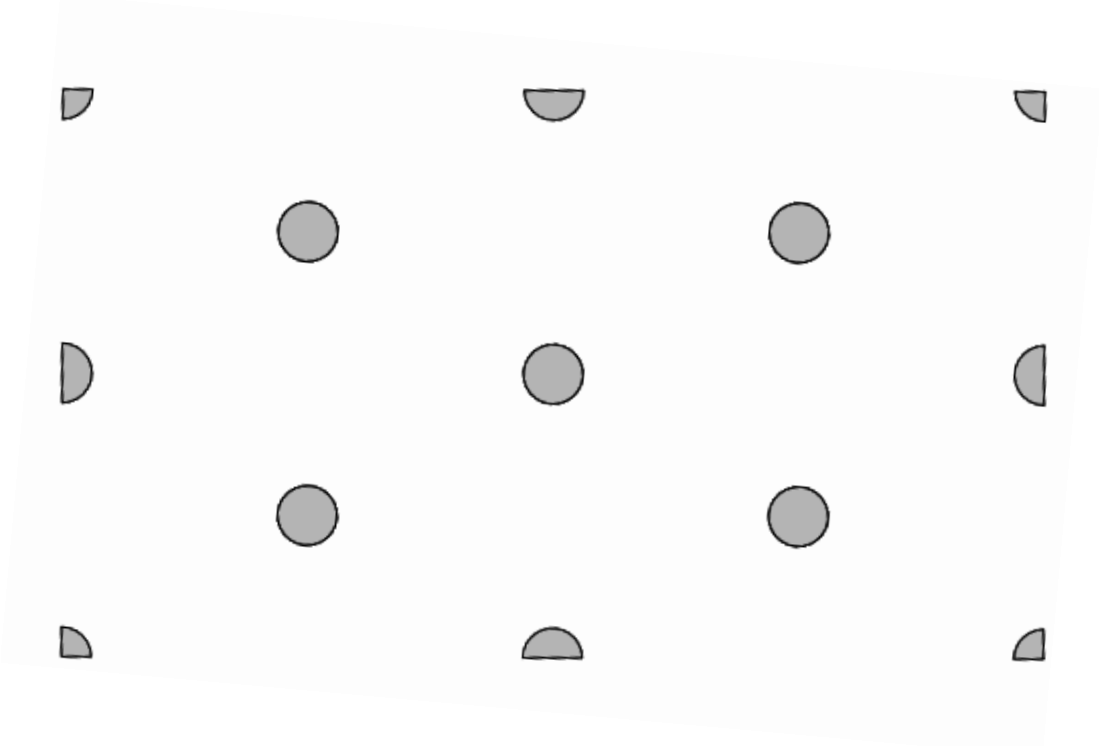

Figure 3.9 Triangular pattern of the external part of the machine. At each side of the pattern a symmetry condition was imposed.

Table 3.5 A and B coefficients values and their coefficient of determination for the air distribution plate porosity study.

Part	A [kg/m^4]	B [kg/(m^{3}s)]	R^2
1	4.6017	2.2453	1
2	2.3959	1.7484	1
3	5.7343	2.3484	1
4	10.746	2.9095	1
5	18.405	139.95	0.9896
Ext	319.06	32.379	1

increseas monotonically from the internal parts to the external ones except that coefficients for part 1 are larger than coefficients for part 2. This could be explained by the holes distribution density that seems a bit lower for part 1, as can be seen in Figure 3.8. The part 1 set of simulation

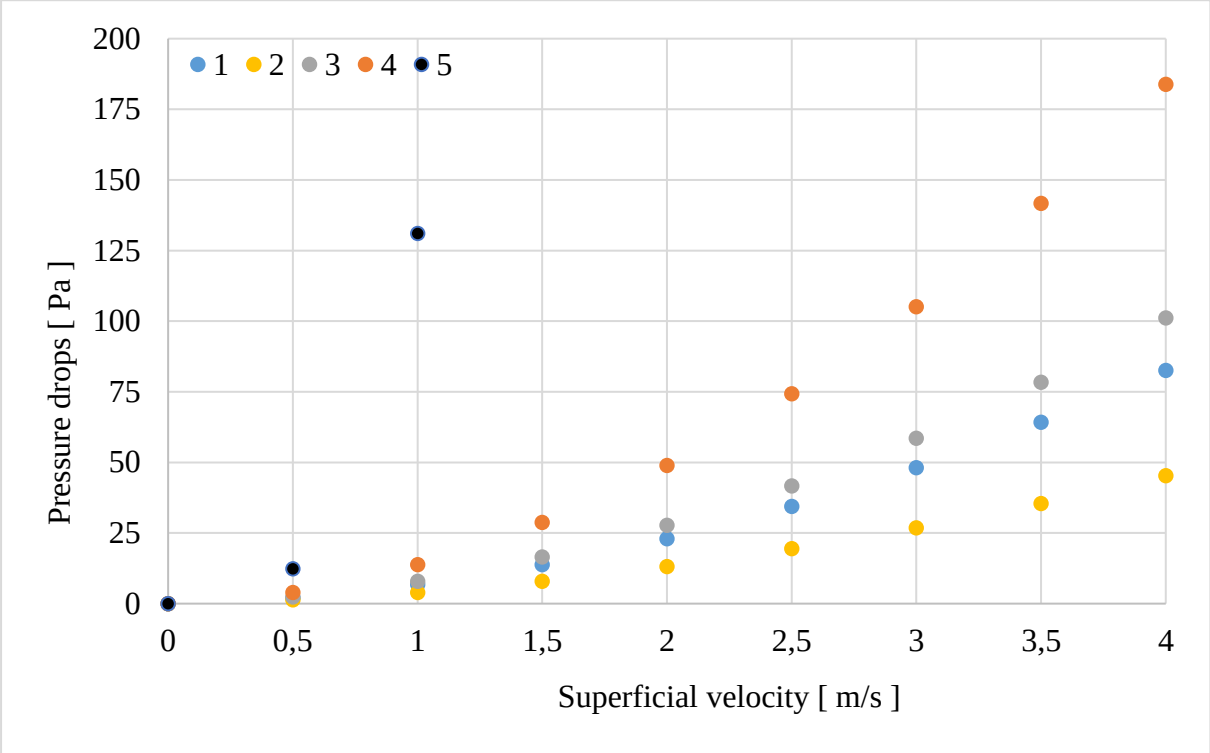

Figure 3.10 Pressure drops against superficial velocity for the five different internal parts.

were also the only one that gave a coefficient of determination smaller than 1. Since the simulation for deriving the porous formulation for each part of the air distribution plate was considered reliable, A and B coefficients were used for modeling the plate as a porous mean in the CFD simulation of the whole ARIA120 equipment in Wurster configuration. A single simulation with a mass flow of 1000 Nm^3/h was performed. The product support grid was simulated using the coefficient expressed in (3.1). The SST k-ω method was used to perform the simulations.Unfortunately the simulation of the whole machine with the modeling of the air distribution plate as a porous mean with differentiated loss coefficient did not give good results. The asymmetry in the base plenum and in the cylindrical part of the basket casued an unwanted and etotally unexpected velocity distiribution above the plate. The external flow rate is smaller than the internal flow rate which should definitely hinder the Wurster process and make the ARIA120 equipment not usable in the coating configuration. It is opinion of the author that the simplifications made for the base plenum and the inlet pipe connection 3D modeling played a

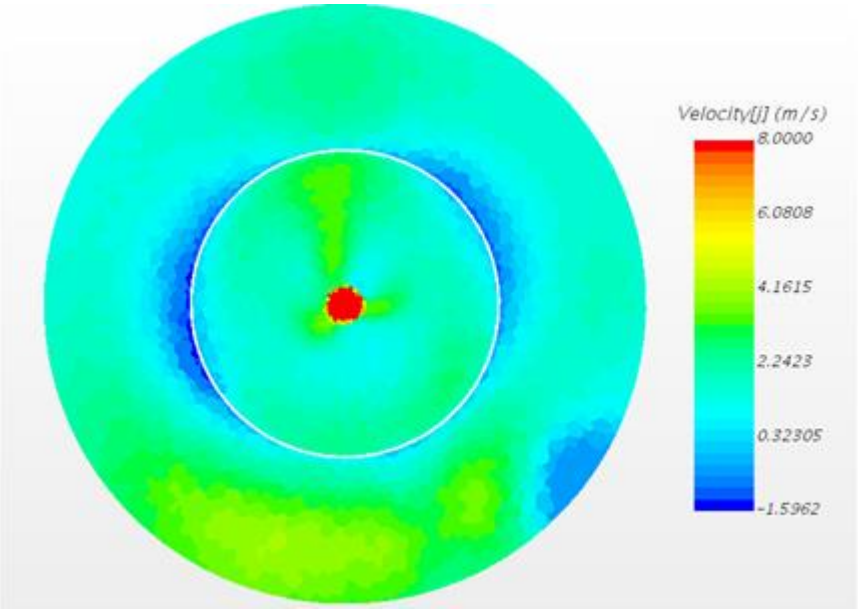

Figure 3.11 Air vertical velocity profile at 80 mm from the support grid.

major role in this bad outcome. Moreover, the turbulence model could be not appropriate for the frequent section enlargements and shrinkages that occurs in the machine. A top view of the air vertical velocity profile in the product basket at 80 mm from the support grid is shown in Figure 3.11. The air vertical velocity is not well distributed over the plate and, except for the central zone where the atomizer is present, there is no clear differences beteween the external part and the internal part. In this situation it is impossible to have a spouted bed and to perform the Wurster process. However, in the reality, the Wurster process occurs without problems. Since the real application of the Wurster process occurs without problems in the present machine. It was decided to not pursue this method to get information about mass flow rate inside the two parts of the machine.

Axial symmetric simulation of the whole plate

Every 60°, the holes pattern of the air distribution plate repeats itself. To find a correct amount of the distribution of the air flow rate due to the plate, it is possible to simulate only a sector of

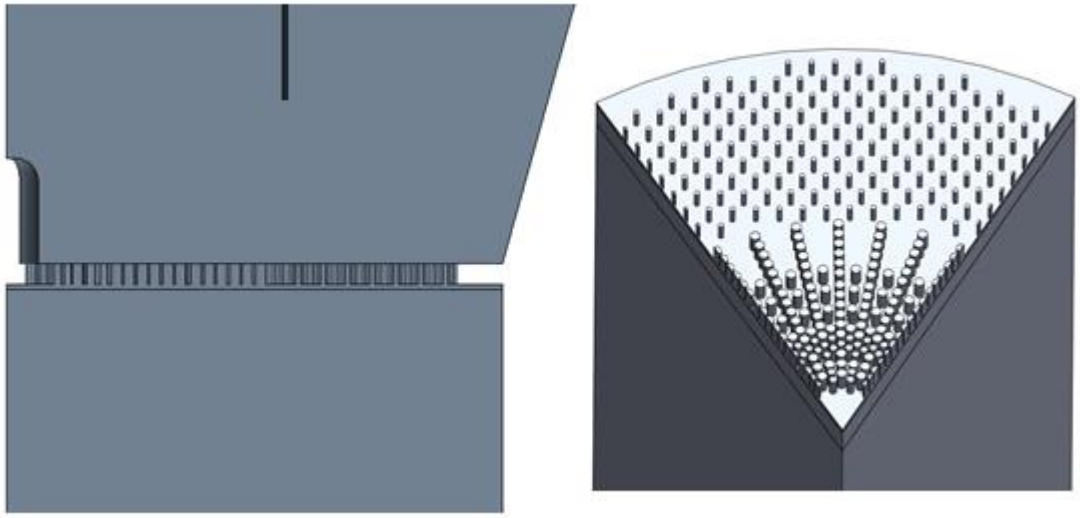

Figure 3.12 Fluid domain of the model used for the axial symmetric simulation of flow through the air distribution plate. Lateral view and isometric view.

the plate. However, this approach omits to consider the upstream flow in the basement, which is not axial symmetric. The axial symmetric simulations were performed using STAR CCM+ and imposing the periodic condition at the side of the 3D model. Boundary conditions are the same of the ones used in the previous approach. However, results are completely different and reflect more the expectation for the velocity profile in a Wurster coater. As can be seen from Figure 3.13, the vertical velocity is higher in the internal part of the machine and lower in the external part. The division between the two different zones is clear and recognizable as expected. Confirmation of this fact is given also by the velocity contours right above the plate, as can be seen in Figure 3.14. In the central part of the plate and then inside the Wurster tube there is a higher flow rate. Therefore, this approach was pursued because it was more promising than the previous one. Several simulations were performed at different air superficial velocity. Air viscosity and density are the one calculated from literature correlations for air at the atmospheric pressure and at two different temperatures, i.e., 20 °C and 70 °C [65]. The used turbulence

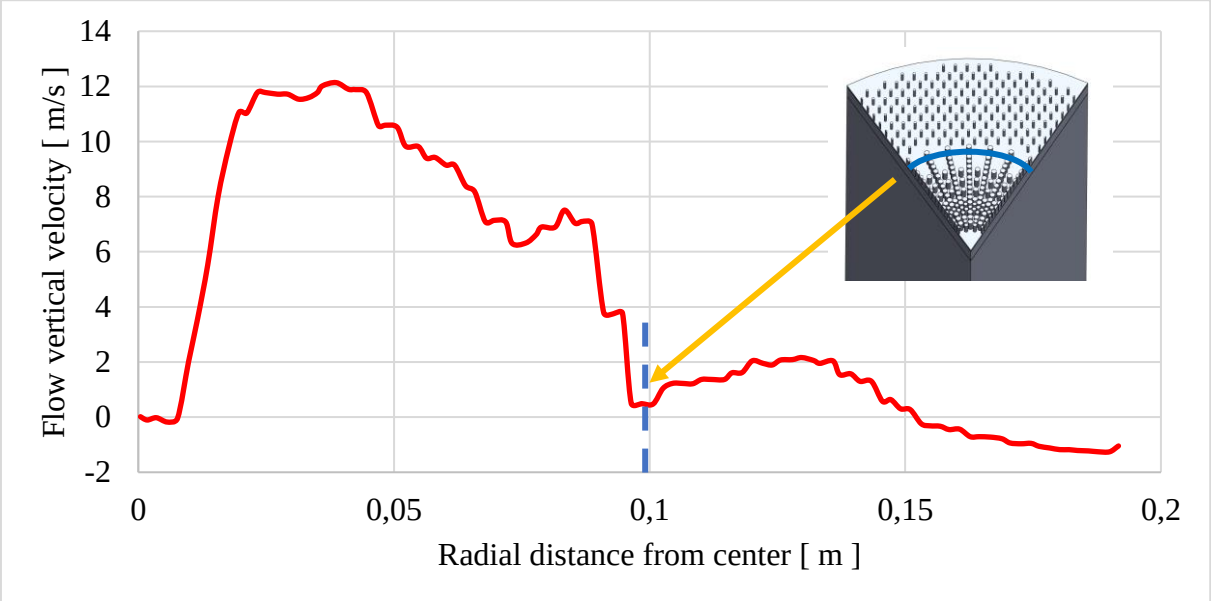

Figure 3.13 Air vertical velocity profile at 41 mm from the support grid.

model was the SST k-ω. The distance between the Wurster tube and the product support grid was either 10 mm or 71 mm. The air mass flow rate passing through the internal and the external part of the air distribution plate was measured. The ratio between these two mass flow rates calculated as follow:

$$R = \frac{\dot{m}_{int}}{\dot{m}_{ext}} \tag{3.6}$$

Where $\dot{m}_{int}$ and $\dot{m}_{ext}$ are respectively the mass flow in the internal and external part of the plate.

The different values for this ratio are shown in Figure 3.15. The value of the air mass flow ratio seems to decrease with the inlet superficial velocity, but it is stable for larger velocities. However, the decrement of the ratio in the whole spectrum of superficial velocity involves only

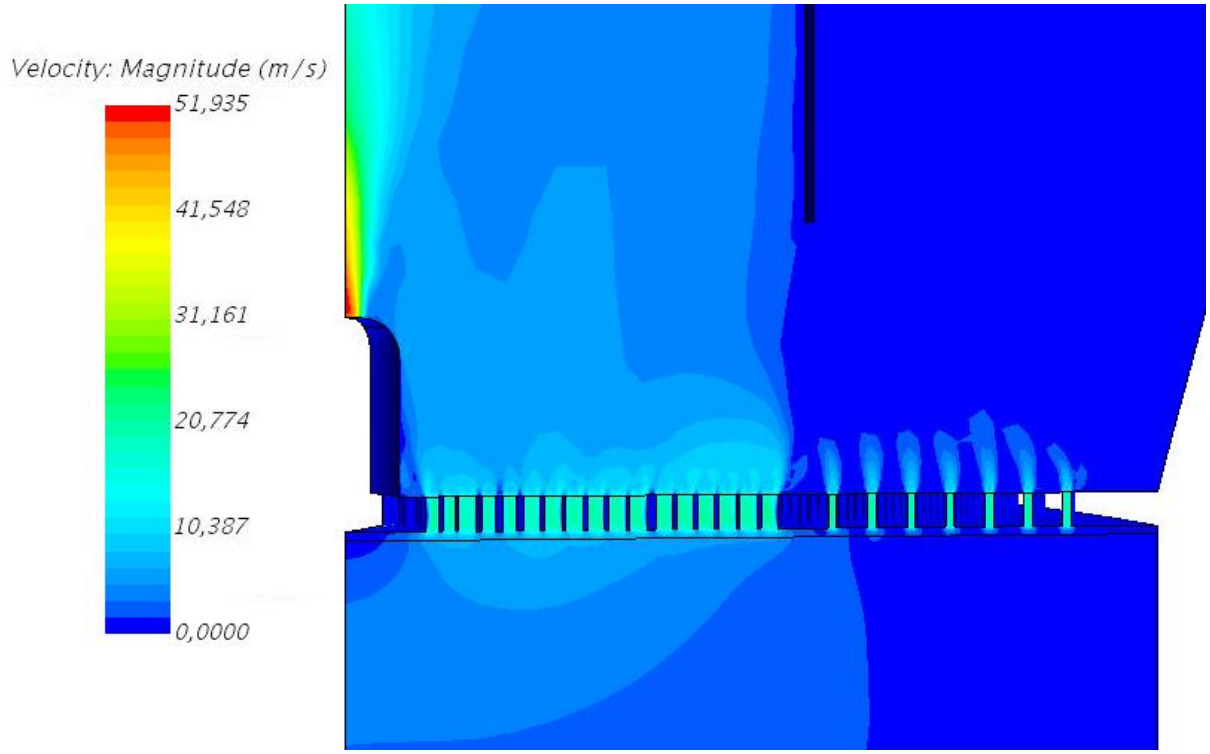

Figure 3.14 Velocity magnitude contours in the plate and above the plate zone. Side view.

the 4th significant figures. Therefore, for the virtual replication of the real experiments mass flow ratio equal to 3.384 was chosen.

3.4.5 MP-PIC simulation of ARIA120

Barracuda VR allows to inject liquid particles that can coat solids particles. When a liquid particle clouds gets in contact with a solid particle cloud the surface of solids particles are evenly coated with a total amount of liquid contained in the liquid particle. However, liquid film on particle cannot participate in phase changes, so drying of coated pellets is not possible. Despite the method is trivial and does not allow immediate drying, it is helpful to understand whether the batch is coated evenly among all the pellets. This approach can account in real time for the coating shield effect of particles that pass closer to the coating atomizer with respect to particle that pass further. This was not possible when only the residence time distribution in the spray

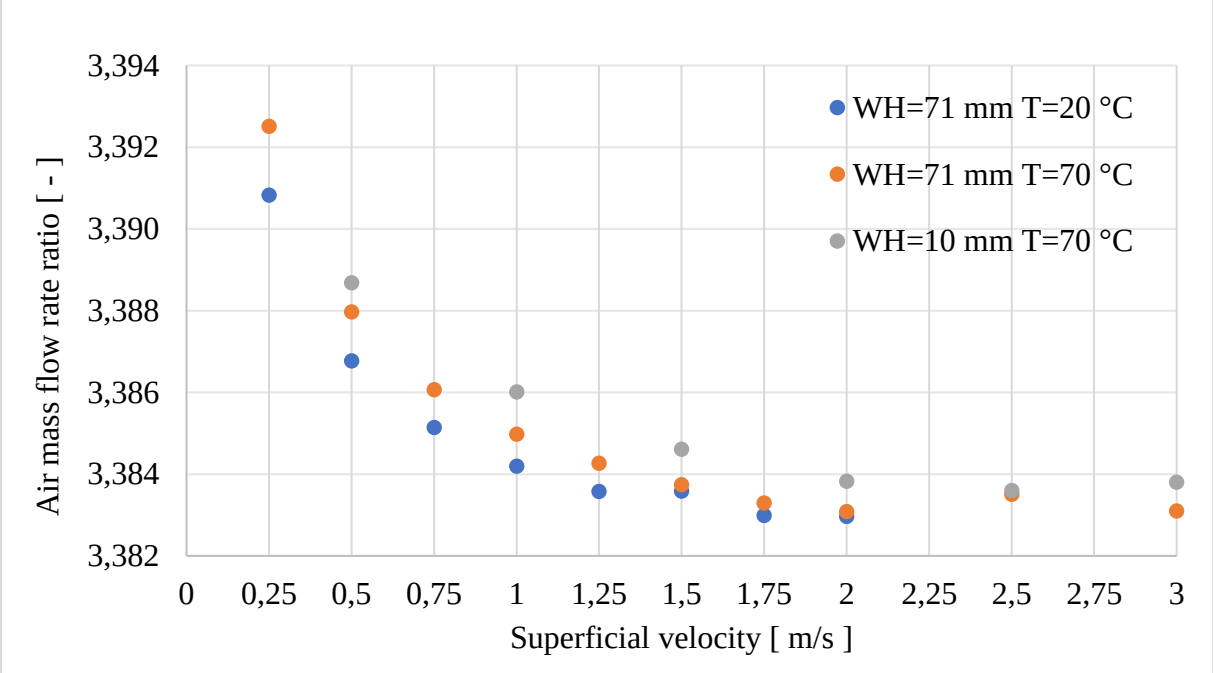

Figure 3.15 Air mass flow ratio between the internal and the external part of the distribution plate.

zone was measured such as done in the validation study in Section 2.6 to replicate the CFD-DEM calculations by Li et al [24]. The set of virtual experiments presented in Table 3.4 is replicated in Barracuda VR. With respect to the validation study (see Section 2.6.2), the software and hardware has improved: the version of Barracuda VR is the 17.1.0 and the used GPU is a NVIDIA GeForce GTX 1070 equipped with 2880 CUDA cores, 7.5 times the CUDA cores available before. This improvement allowed the simulation of 1 seconds of real time in a bit more than 1 minute. The real experiments had a spray phase which lasted more than 4 hours. Such a simulation would require more than 10 days to be performed, which is an astonishing result. Such a computational performance outdoes all computational performances found in literature as of today author knowledge. However, without a correct model for drying the coating solution on pellets, it is pointless to perform the whole process, since the coating solution is made of 89.6 % of water and, if not removed by drying, the particle growth will be too high, hindering the drag performance of pellets and the accuracy of the simulation. The virtual

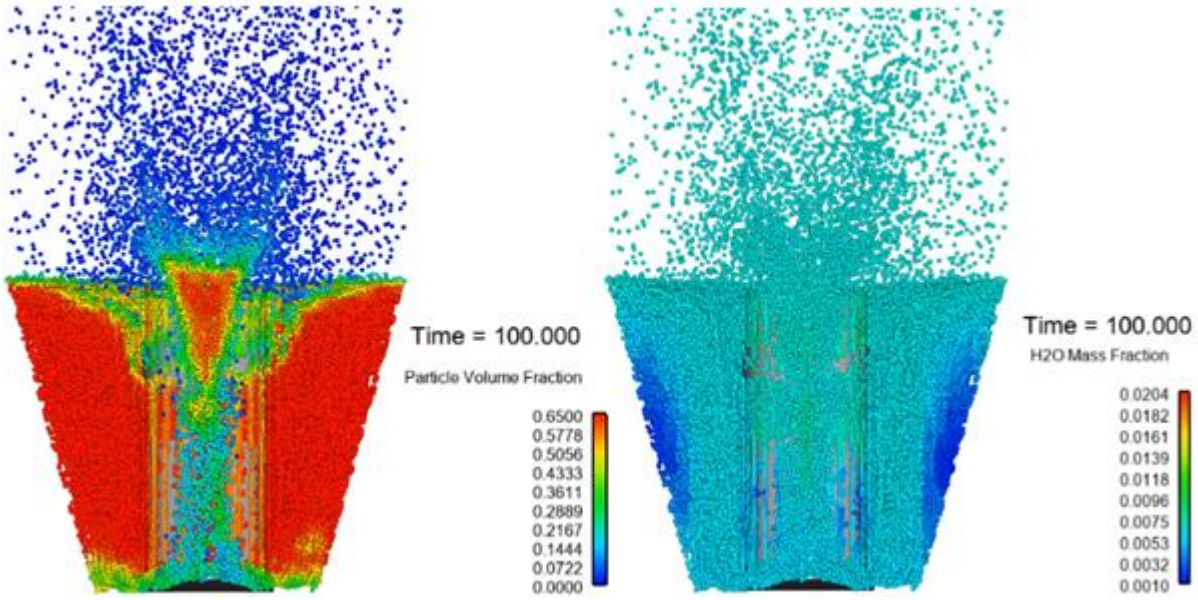

Figure 3.16 Snapshots of the particle volume fraction (LHS) and the water mass fraction on pellets (RHS) taken at 100 seconds of simulation.

experiments start with a phase for allowing particle pellets to move for 2 s before the actual spray of coating occurs. After 100 s, a snapshot of the state of the computational particles is taken to measure how much coating solution they received. The simulation is then carried on until the total simulation time reaches 600 s. The closing pack volume fraction of the particle is set to a value $\alpha_{cp} = 0.63$. The qualitative fluidization performance of the virtual experiment 1 can be seen by the snapshot of the of the particle volume fraction shown in Figure 3.16. The Wurster process occurs as the best practice suggests: in the central part particle are spouted towards the top of the machine and in the external part the bed slowly move downwards. In the horizontal transport region particle are slightly fluidized and this facilitates the particle motion towards the central part of the machine. On the right-hand side of Figure 3.16 the water mass

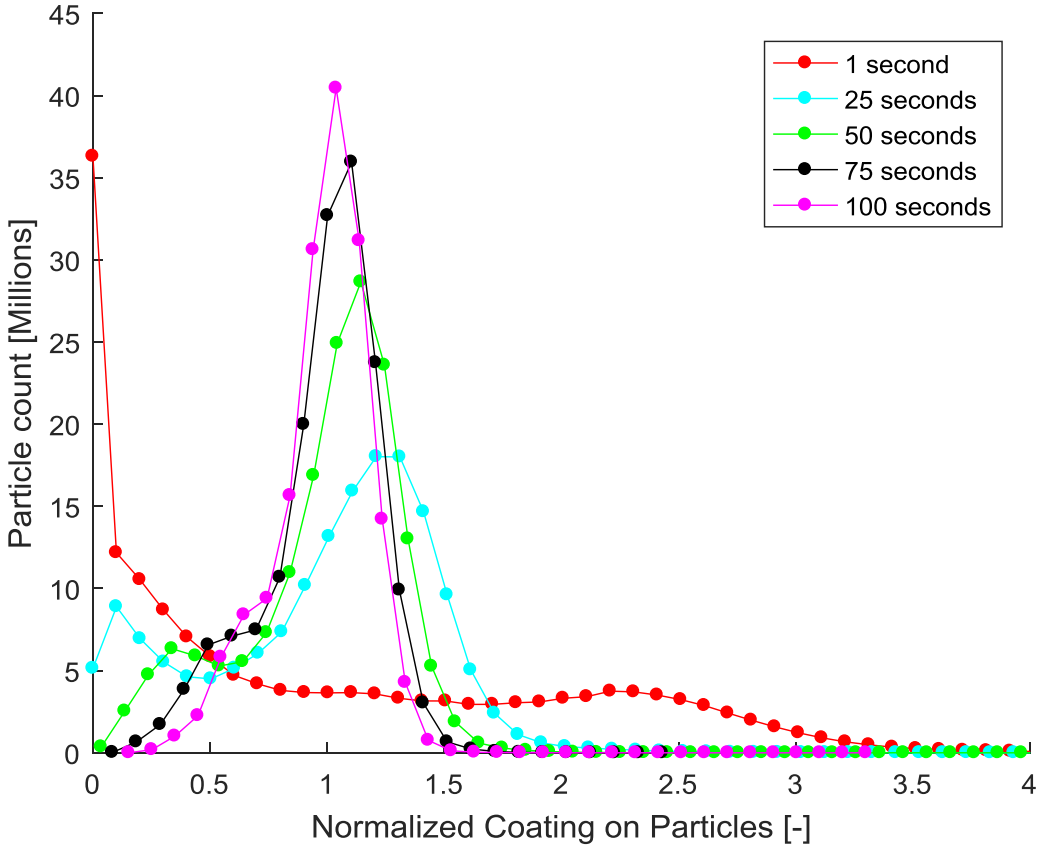

Figure 3.17 Normalized coating distributions for experiment 1.

fraction on pellets is shown after 100 s of simulation. There is a clear spot, on the side walls of the product basket, were particles move slowly and receive less coating solution. A strategy to remove this particle dead spot could be implemented to increase the performance of pellets coating distribution.

Method for comparing pellets coating distribution at different spraying times

As the coating solution is sprayed the coating distribution is expected to shift towards higher coating amounts. Since the set of experiments include different coating spray rates the coating distribution will shift at different velocities in time. A method of normalization is needed and the proposed one is to consider the normalized coating on particles, $\bar{m}_c$, defined as follow:

$$\bar{m}_c = \frac{m_c}{m_s} N_p \tag{3.7}$$

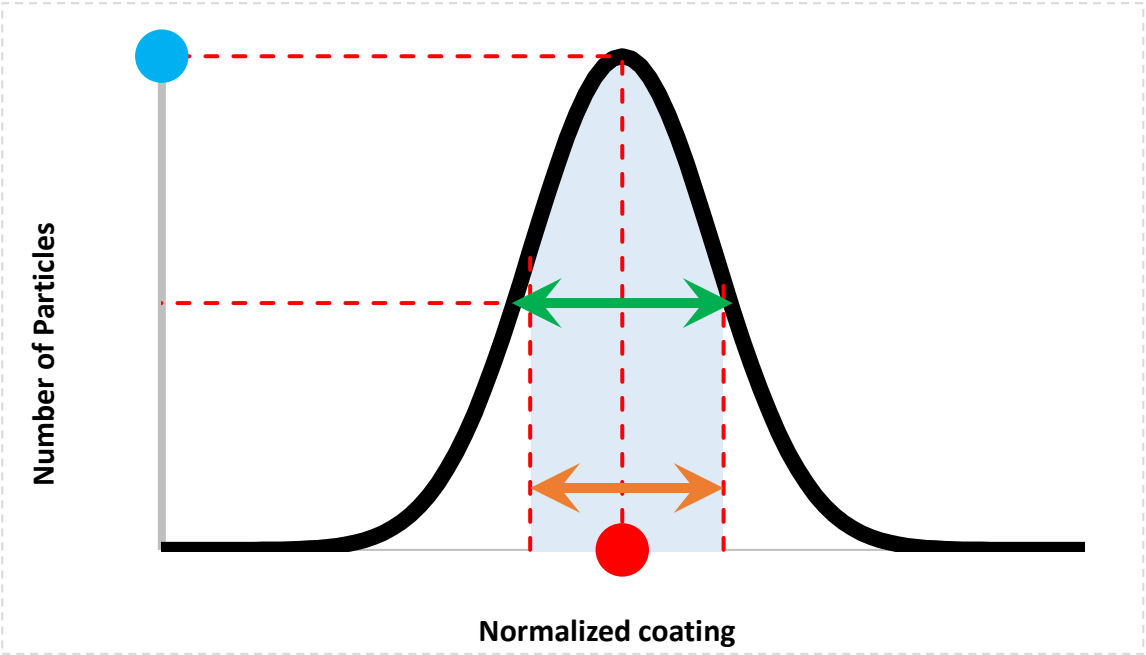

Figure 3.18 Quantitative analysis of the coating distribution peak. The blue dot is the height of the peak (PH), the green distance is the width of the peak (PW), the red dot is the peak normal coating (PNC) and the orange distance is the confidence width (CW).

where m_c is the coating solution mass on particle, m_s is the total mass of the coating sprayed and $N_p$is the total number of particles in the system.

If all particles receive the same amount of coating, the normalized coating on particle has a value equal to 1. Thus, the best coating distribution has a single narrowest peak at 1. The coating distributions during the first 100 s of simulation for the experiment 1 is given in Figure 3.17. As expected, the coating distribution quality increases with time to reach narrow peaks at a normalized coating value equal to 1. Qualitatively the improvements of the coating distribution are clearly visible when simulation spraying time increases from 1 s to 75 s. However, it is difficult to appreciate the differences between the peaks at 75 s and 100 s. It is expected that these differences will decreases in time. To better capture differences in the peaks of the coating

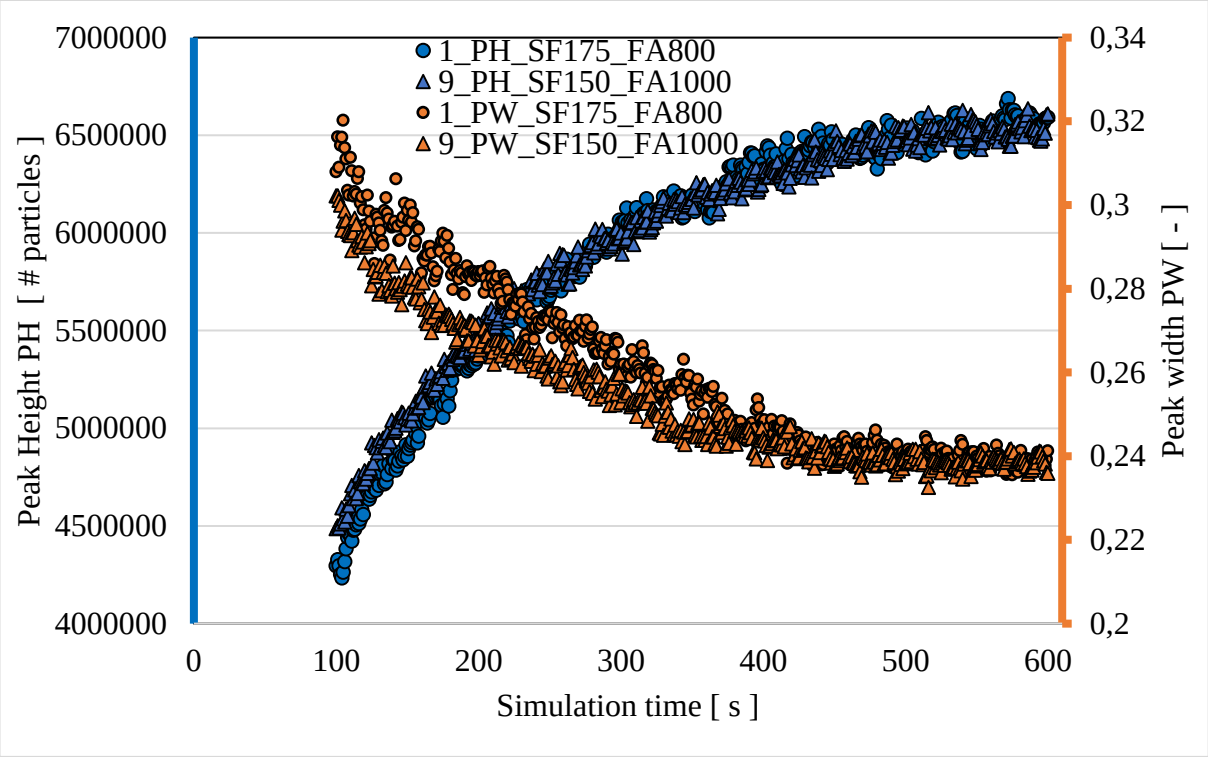

Figure 3.19 Peak height PH and peak width PW time evolution for experiment 1 and experiment 9. SF is the spraying flow rate in ml/min and FA is the fluidization air flow rate in Nm^3/h.

Table 3.6 Mean PH and mean PW in the last 10 s of simulation for the 9 virtual experiments.

Experiment number	Spraying flow rate [ml/min]	Fluidization air flow [Nm^3/h]	Mean PH in the last 10 s [$\times 10^{-6}$]	Mean PW in the last 10 s [-]
1	175	800	6.562	0.2395
2	200	800	6.563	0.2392
3	150	800	6.554	0.2387
4	200	1000	6.586	0.2380
5	200	900	6.572	0.2374
6	175	900	6.524	0.2392
7	150	900	6.534	0.2385
8	175	1000	6.632	0.2363
9	150	1000	6.521	0.2387

distributions, a quantitative peak analysis strategy was proposed. The peak has a height, PH, measured in number of particles. The width of the peak, PW, which is expressed in normalized coating units, is taken at half of the peak height. The peak normal coating, PNC, is the value of normal coating of the peak. The confidence width, CW, is measured in normal coating units and it measures the width of the area that includes 95 % of particles. The value of 95 % for CW was arbitrary chosen, but it is tunable to complaint with the request of specific industry quality department. To better understand these quantities a graphical explanation is given in Figure 3.18 The quantities introduced are measured for the whole set of experiments by sampling the particle status each second from 100 s of simulation till 600 s.

Peak height and peak width comparisons

In Figure 3.19 the time evolution of the peak height and time evolution of the peak width are presented, starting from 100 s and till 600 s. The experiments have a similar PH evolution which reaches approximately 6.5 million of particles. The time evolution of PW is faster in the

beginning of data collection but both time evolutions reach a value close to 0.24 in normal coating units. Every experiment has similar PH and PW evolution and it is difficult to compare them. Therefore, average PH and PW values for the last eleven samples, corresponding to the last 10 seconds of simulation for each experiment were calculated and reported in Table 3.6. Experiment 8 has the highest average peak and the smaller peak width. The largest average PW was measured for experiment 1 and the smaller average PH was measured for experiment 9. However, it is impossible to draw a clear conclusion on these quantities because variability is very low: the standard deviation of PH and PW values is below 1 %. Therefore, it is not advisable to draw conclusions from these quantities.

Peak normal coating comparison

The peak normal coating evolves from a very unstable value slightly above 1 to a more stable value around 0.98. For each experiment the average value of PNC measured in the last 10 s is

Figure 3.20 Peak normal coating evolution for experiment 3 and experiment 7. SF is the spraying flow rate in ml/min and FA is the fluidization air flow rate in Nm^3/h.

Table 3.8 Time to reach $CW = 0.205$ for the 9 experiments.

Experiment number	Spraying flow rate [ml/min]	Fluidization air flow [Nm^3/h]	Time to reach $CW = 0.205$ [s]
1	175	800	415
2	200	800	430
3	150	800	420
4	200	1000	582
5	200	900	577
6	175	900	583
7	150	900	578
8	175	1000	582
9	150	1000	593

equal to 0.9791 ± 0.0032. Therefore, the variation among the experiments is very small. The average values of PNC in the last 10 s of simulation are summarized in Table 3.7. In Figure 3.20 the comparison of PNC evolutions for experiments 3 and 7 is presented. PNC is, in general, higher in the experiment 3. However, the variability of the PNC indicator is too high to draw a conclusion. This evidence induces to not consider PNC as a valuable indicator to evaluate the coating performance.

Confidence width comparison

Despite confidence width is calculated with a fixed resolution of 0.005 normal coating units, it is considered, in author opinion, the best indicator for the quality of coating. Every experiment reaches a CW value equal to 0.205 normal coating units after 600 s. However, as can be seen in Figure 3.21, the final value is reached at different speeds. The CW time evolutions for experiments 1, 2 and 3 seems to be faster, especially in the initial period of sampling. On the other hand, experiments 5, 6 and 7 seems to have a slower CW time evolution. The time at

which CW reaches the stable value equal to 0.205 is measured and reported in Table 3.8. The worst set of experiments, in terms of time to reach CW equal to 0.205, are the ones with a fluidization flow rate equal to 1000 Nm^3/h. Experiments with fluidization flow rate equal to 900 Nm^3/h are slightly better than those with a fluidization flow rate equal to 1000 Nm^3/h. However, the best performance in terms of CW is given by the experiments with a lower fluidization flow rate that reach CW equal to 0.205 about 150 s before the other experiments and, on a total simulation time of 600 s it is a remarkable result. Experiment 1 is chosen as the best performance experiment even if difference with experiments 2 and 3 are quite negligible.

3.4.6 Conclusive remark

Using Barracuda VR, it was possible to extend the knowledge of the Wurster process performed in I.M.A. S.p.A. These results, especially the results obtained by comparing the confidence

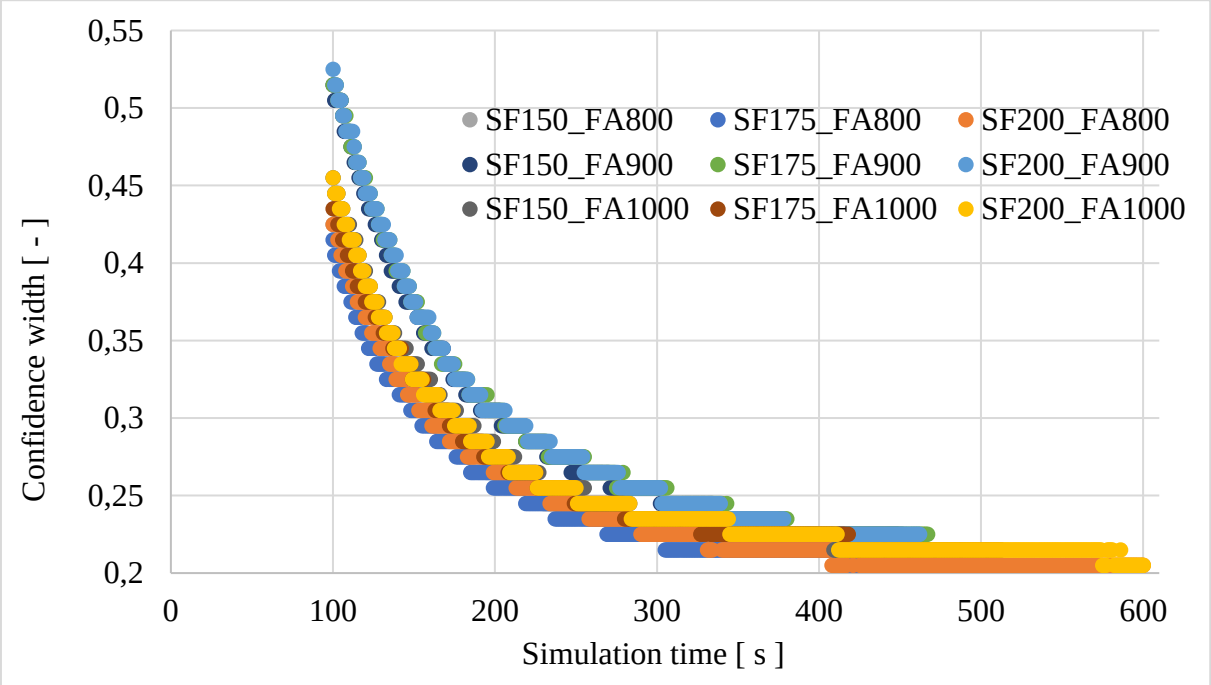

Figure 3.21Confidence width evolution for the 9 experiments. SF is the spraying flow rate in ml/min and FA is the fluidization air flow rate in Nm^3/h.

width indicator, will be used as guidance for the virtual prototyping of a novel machine. The operating conditions used for the virtual experiment 1 will be also used in the design process of the virtual prototype.

Section 4
Virtual Product design of a Spin Flow Fluidized Bed for granulation and coating

4.1 The Spin Flow Fluidized Bed concept

The high mass, momentum and heat interfacial exchange between particle and gas in conventional fluidized beds is limited by the gas-solids slip velocity. The maximum achievable slip velocity is the free-fall velocity of the particles, which strongly depends on the gravitational field [15]. By rotating the fluidization chamber, it is possible to generate centrifugal forces, which are a multiple of gravity, thus, increasing the maximum allowable slip velocity [68]. Moreover, very fine and cohesive particles (Geldart group C [21]), can be easily fluidized in centrifugal fields which are strong enough to overcome the van der Waals forces acting between particles [69]. Despite the clear advantages in terms of process intensification, a rotating fluidized bed has not been introduced in industrial application because the rotating equipment would introduce several problems such as vibrations and sealing [68]. To outcome these issues, De Wilde and de Broqueville introduced the concept of rotating fluidized bed in a static geometry (RFB-SG) in recent years [69]. The particle bed is kept uniform in a RFB-SG even at high gas-solids slip velocity and the mass, momentum and energy transfer coefficient are intensified [70]. The concept of RFB-SG was investigated using TFM simulations, including

practical applications such as fluid catalytic cracking, biomass gasification [71–74]. Keeping in mind its best performance, the idea of RFB-SG will be applied to ARIA120 equipment. The main geometry of the components will be kept, but a solution to obtain a RFB-SG such as the one proposed by De Wilde. To avoid confusion, this solution will be called "Spin Flow Fluidized Bed" (SFFB) or simply "Spin Flow". This investigation will be carried out with different virtual prototype based on the ARIA120 granulation configuration. The aim of this set of virtual prototypes is to verify whether the use of the new configuration can fluidize the bed in a spin flow behavior. Since particles for coating are spoutable, it is believed that they are harder to be fluidized with respect to the granulation particles. In fact, in the present process, particles are

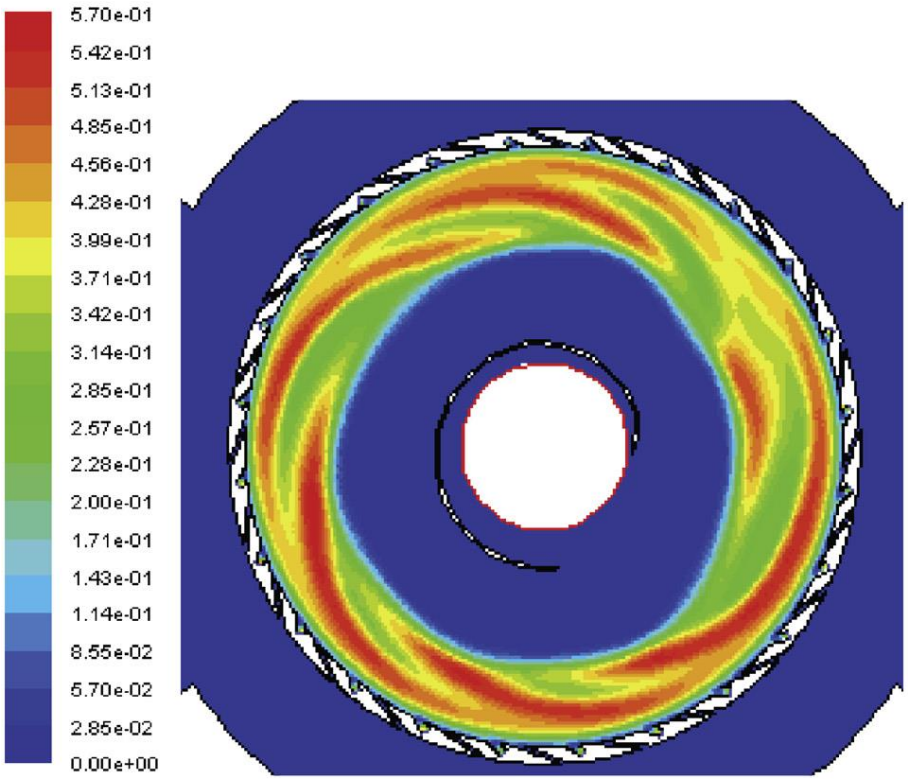

Figure 4.1 Particle volume fraction in a RFB-SG obtained with TFM simulations by de Broqueville and De Wilde [71].

spouted in the Wurster tube. Therefore, this study is more focused on developing the coating process in the ARIA120 granulation configuration.

4.2 Virtual Prototype S00. Using a tangential inlet

The first virtual experiment performed tested the fluid flow that is developed if the air inlet enters the basement tangentially without considering the presence of the solid bed. Simulations were performed using Ansys Fluent. The turbulence model used was the k-ε method ad the support grid was modeled as a porous mean. The air flow was 800 Nm^3/h. While the flow has a clear tangential behavior in the basement, it loses its tangential component when passing through the support grid as can be seen in Figure 4.2 (left hand side). Therefore, the product will be not affected by this solution, since the flow field in the basket and in the chamber is mainly

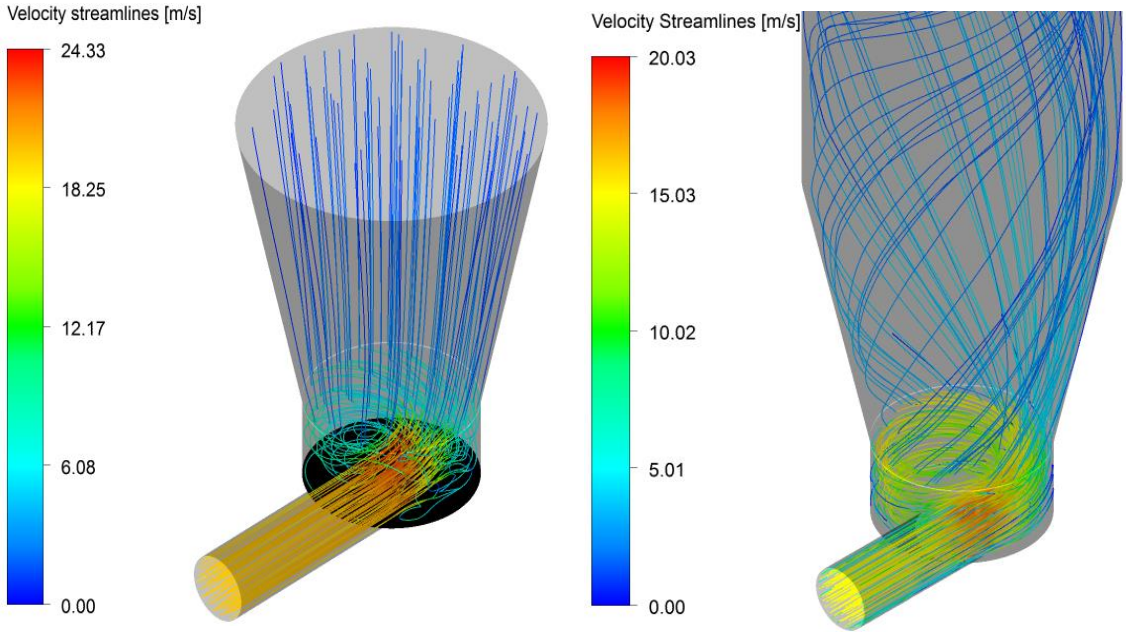

Figure 4.2 Streamlines for testing the tangential inlet. The support grid is an isotropic (LHS) or anisotropic (RHS) porous mean.

Table 4.1 Set of virtual experiments for VP S01.

Virtual experiment	Spraying flow rate [ml/min]	Total air flow [Nm^3/h]	Bottom air flow [Nm^3/h]	Lateral air flow [Nm^3/h]	Ratio *R*
S01_W1	175	800	182.48	617.52	3.384
S01_W1.2	175	800	158.08	641.92	4.0608
S01_W0.8	175	800	215.80	584.2	2.7072
S01_W3	175	800	71.74	728.26	10.152
S01_W0.33	175	800	375.94	426.06	1.128

vertical. To partially keep the tangential component the porous formulation of the support grid must be anisotropic: the two tangential coefficients will be much lower than the normal one. Used tangential coefficients were 100 times lower than the normal one. As can be seen in the right-hand side of Figure 4.2, this solution allows to keep the flow tangential component downstream the grid. To apply this solution in the real machine, an ad-hoc support grid must be provided. However, such a support grid could be useful only for a narrow range of operating conditions because it is static. It is believed that such a solution will not be able to provide a SFFB.

4.3 Virtual Prototype S01. Tangential additional inlet in the basket at 0.36 m height.

In the current ARIA120 equipment, it is possible to add a tangential inlet (with a diameter equal to 50.8 mm) in the basket at an approximate height equal to 0.36 m from the support grid with the atomizer placed right below it and in the same direction. This lateral inlet is almost tangential and has a direction with an angle equal to 20° with respect to the horizontal plane. A small real

granulation test was performed keeping the total air flow rate at a value equal to 800 Nm^3/h. However, it was not possible to measure the quantity of air that passes through the support grid and the air that passes in the additional inlet in the basket. The test gave results comparable with standard granulation performances. Therefore, VP S01 was adopted as the first virtual experiment set to test the performance in coating condition. The virtual experiments were performed using Barracuda VR v 17.1.0 running on a NVIDIA GeForce 1070. The boundary conditions are the one used for the case study in Section 3.4.5 for the virtual experiment 1, i.e. a total flow rate equal to 800 Nm^3/m and a spray rate equal to 175 ml/min. The pellets have a density equal to 680 kg/m^3 and the size distribution as shown in Figure 3.7. Batch size has a mass equal to 50 kg. Turbulence is modeled using LES. The ratio $R = 3.384$ was applied meaning that the air flow rate at the lateral inlet is 3.384 times the air flow rate at the bottom of the machine. The set of experiments includes other 4 values for the ratio as shown in Table 4.1. Due to the high flow rate that passes in the lateral inlet, especially when $R = 10.152$, the lateral inlet was modeled with a diameter equal to 101.6 mm. The 3D model of VP S01 is shown in Figure 4.3. The study of the SFFB will be focused on the performance in terms of tangential fluidization, so it is rather qualitative. However, the performance in terms of confidence width

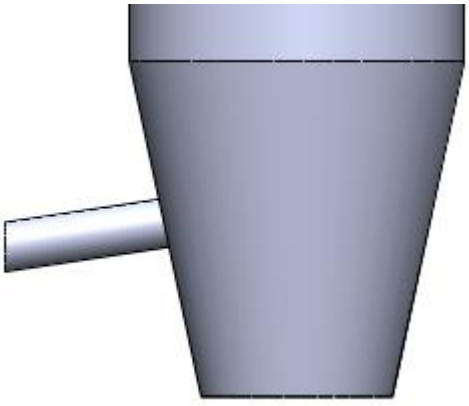

Figure 4.3 3D model for VP S01. Lateral view of basket.

CW will be presented. For this reason and to avoid confusion, fluidization results for virtual experiments S01_W1.2 and S01_W0.8 will not be shown as they are too similar to the results for S01_W1.

4.3.1 Tangential fluid and particle velocity and particle volume fraction

The fluid velocity should be tangential to the wall of the equipment to drag the particle bed and allow SFFB. Moreover, the tangential component must be in the same direction, i.e., clockwise

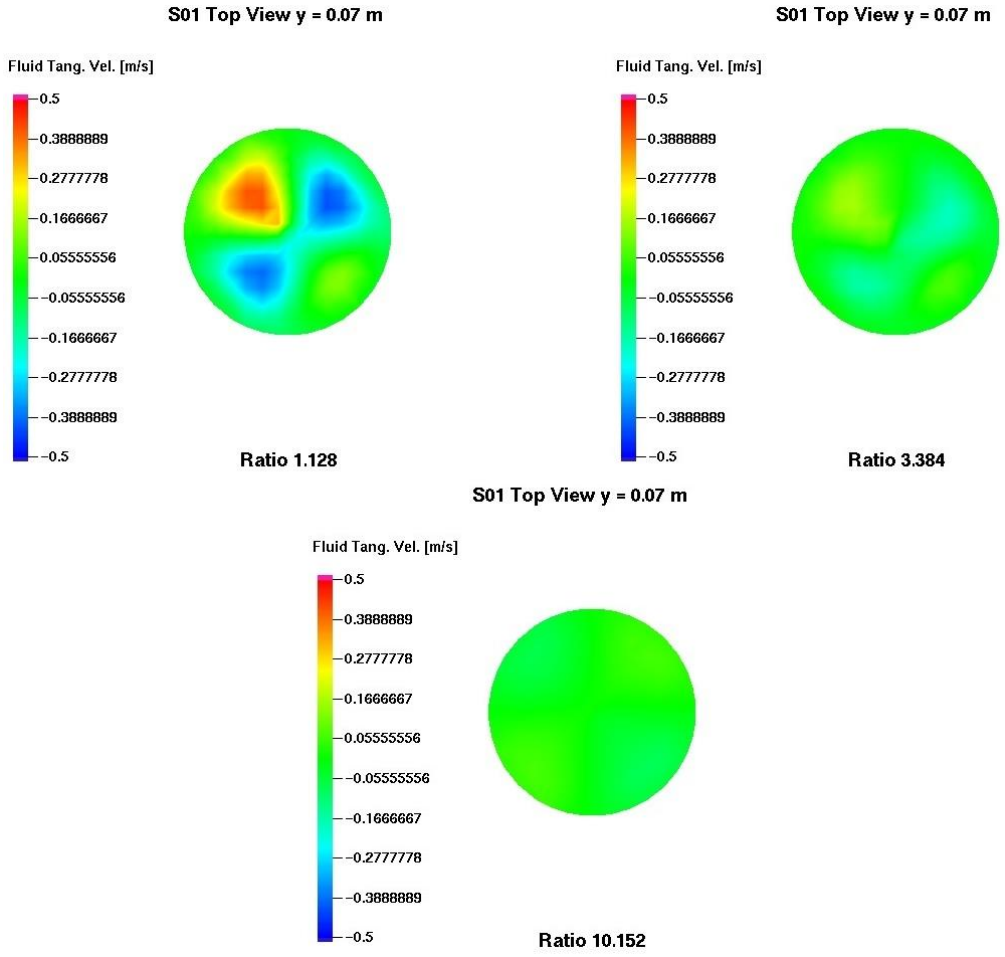

Figure 4.4 Top views at 0.07 m from the grid. Tangential fluid velocity for S01_W0.33 (top left), S01_W1 (top right) and S01_W3 (bottom). Positive velocities are clockwise.

or counter clock wise. Figure 4.4 shows the average tangential fluid velocity at 0.07 m from the support grid. The fluid has barely no tangential velocity when $R = 1.128$ and a small tangential component is present for $R = 3.384$. For $R = 1.128$ the tangential component of the fluid velocity is clear, but it is not in the same direction. This means that the tangential fluid velocity is mainly due to the turbulences that occur normally in the gas-solid flows. At this height in the machine the fluidization is mainly due to the bottom air flow rate which is higher for $R = 1.128$. Figure 4.5 shows the average tangential fluid velocity as a top view at the entrance of the lateral

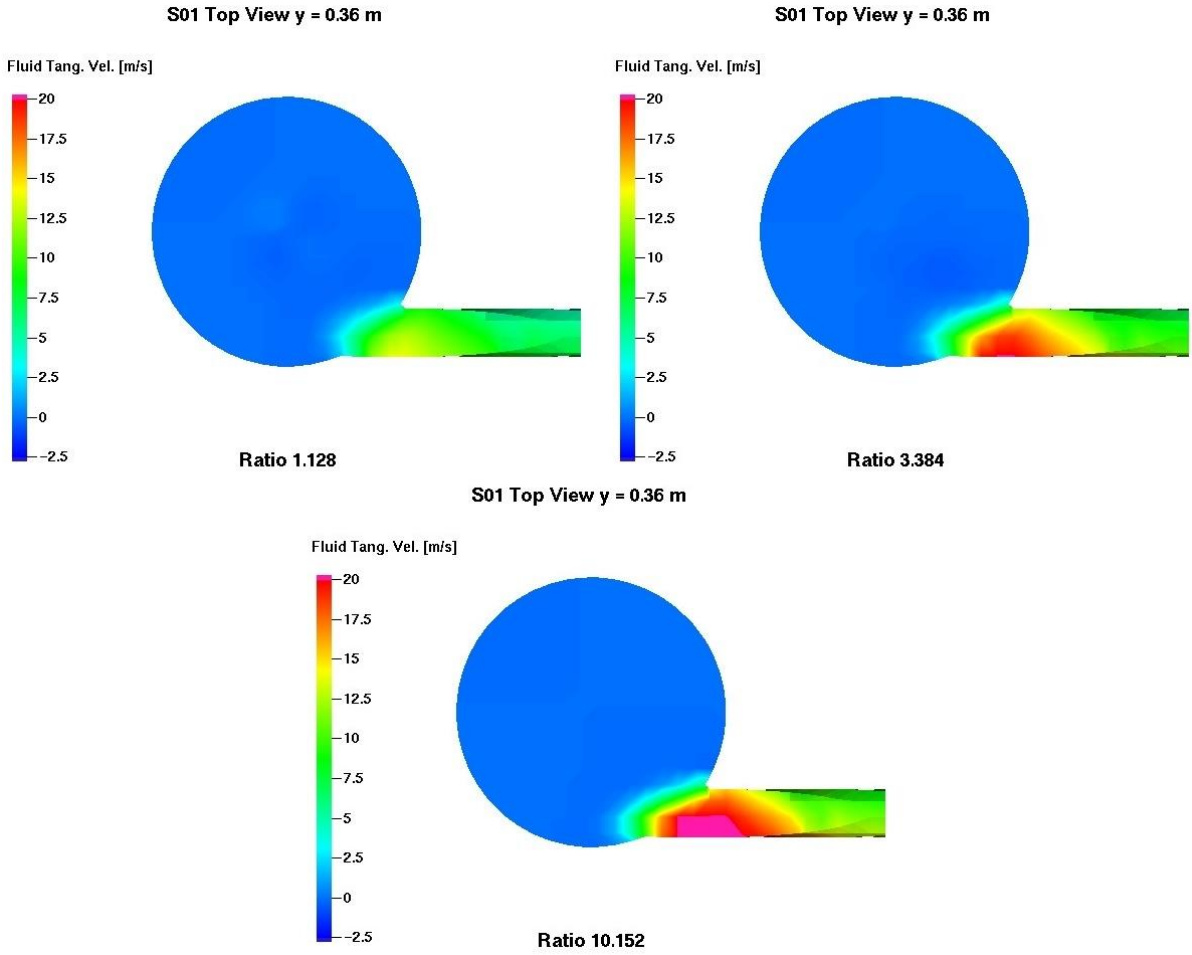

Figure 4.5 Top views at 0.36 m from the grid, the entrance of the lateral inlet. Tangential fluid velocity for S01_W0.33 (top left), S01_W1 (top right) and S01_W3 (bottom). Positive velocities are clockwise.

inlet. The fluid velocity seems to not follow a tangential direction, even when the lateral flow rate is higher for $R = 10.152$. In these air flow conditions, particles cannot be dragged to a spin flow motion. This is confirmed by the average particle tangential velocity which is shown, as vectors, in Figure 4.6. Particles velocity has barely no tangential component inside the equipment. Vectors suggest that particles are entrained towards the axial direction right in front of the lateral inlet. It is opinion of the author that particles are too packed to develop a spin flow in the tangential direction. Therefore, fluid tends to drag particles upwards where the particle

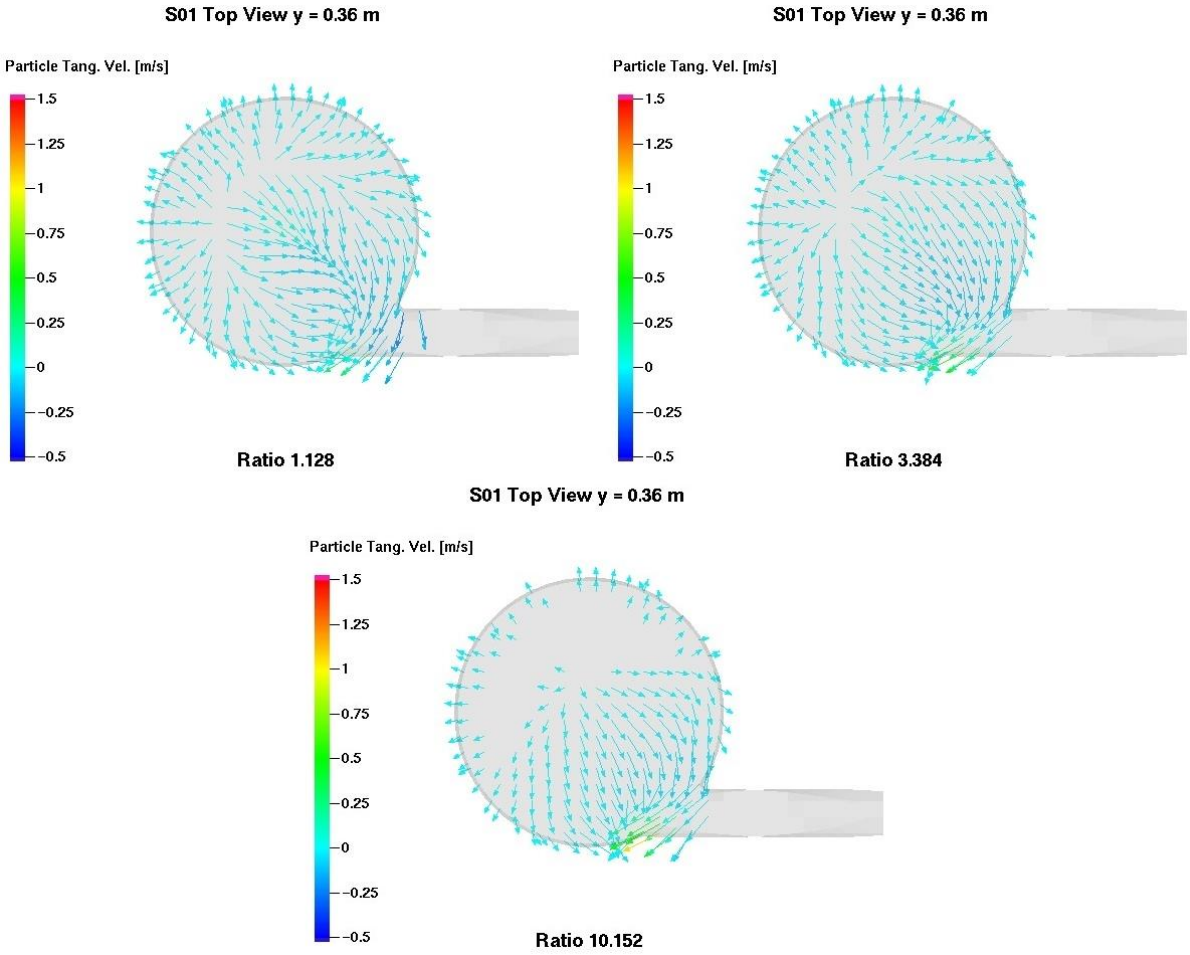

Figure 4.6 Top views at 0.36 m from the grid. Vectors of tangential particle velocity for S01_W0.33 (top left), S01_W1 (top right) and S01_W3 (bottom). Positive velocities are clockwise.

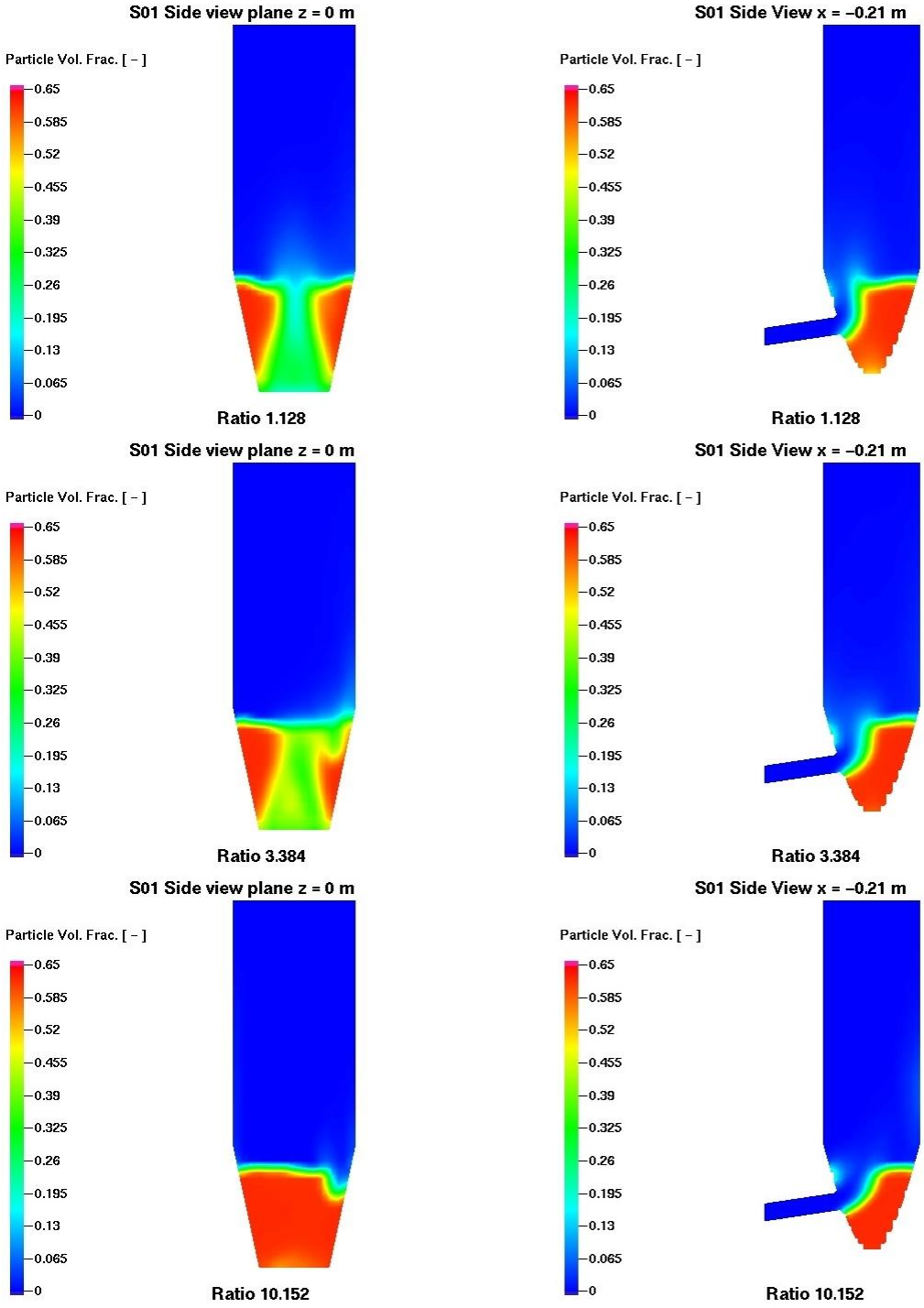

Figure 4.7 Side views of the particle volume fraction for solution S01. Middle side section (LHS) and side section at the entrance of the lateral inlet (RHS) for $R = 1.128$, $R = 3.384$ and $R = 10.152$ from top to bottom.

Table 4.2 Confidence width performance of virtual experiments for solution S01.

Virtual experiment	Ratio R	CW best value	Time to reach $CW = 0.205$ [s]
S01_W1	3.384	0.195	259
S01_W1.2	4.0608	0.195	261
S01_W0.8	2.7072	0.195	246
S01_W3	10.152	NA	NA
S01_W0.33	1.128	0.195	279

bed can expand. This is confirmed by the side views of the average particle volume fraction as can be seen in Figure 4.7. The side views at the position of the lateral inlet show that the fluid tends to occupy a preferred path that brings upwards without developing the SFFB. The particle bed results to be well mixed for $R = 1.128$ and $R = 3.384$.In these two cases, the fluidization air flow coming from the bottom is enough to ensure mixing. However, particles seem to be not well mixed for $R = 10.152$.

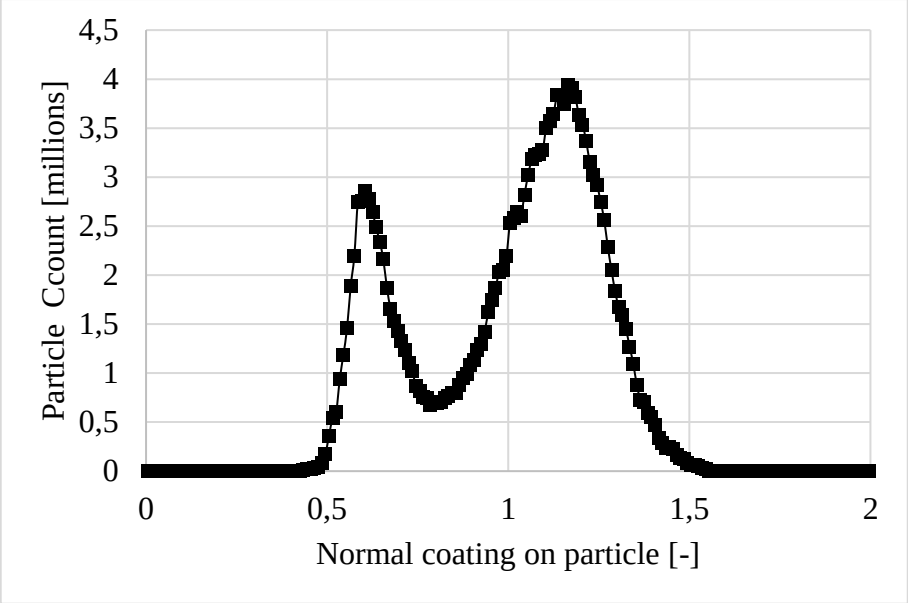

Figure 4.8 Particle coating distribution after 600 s for virtual experiment S01_W3.

4.3.2 Coating performance – Confidence Width

The coating performance expressed in confidence width for the virtual experiments of VP S01 is very good and better than the best performance of the Wurster process. However, increasing the value of the ratio to 10.152 does not give a good performance using this Virtual Prototype. The confidence width is not available for $R = 10.152$ because, as shown in Figure 4.8, the coating distribution has not a single peak, but it shows two different peaks. This result mainly occurs because the particles are not well mixed as previously understood from Figure 4.7. The confidence width performance for VP S01 is shown in Table 4.2.

4.4 Virtual Prototypes S02 and S03. Tangential inlet at 0.07 m from the support grid

Virtual Prototypes S02 and S03 are rather similar and gave comparable results in terms of fluidization. The lateral inlet is moved to the bottom of the basket at 0.07 m from the support grid. The lateral inlet for VP S02 has the same inclination as the one for VP S01, while the lateral inlet for VP S03 is horizontal. The atomizer is not placed in the same position as VP S01,

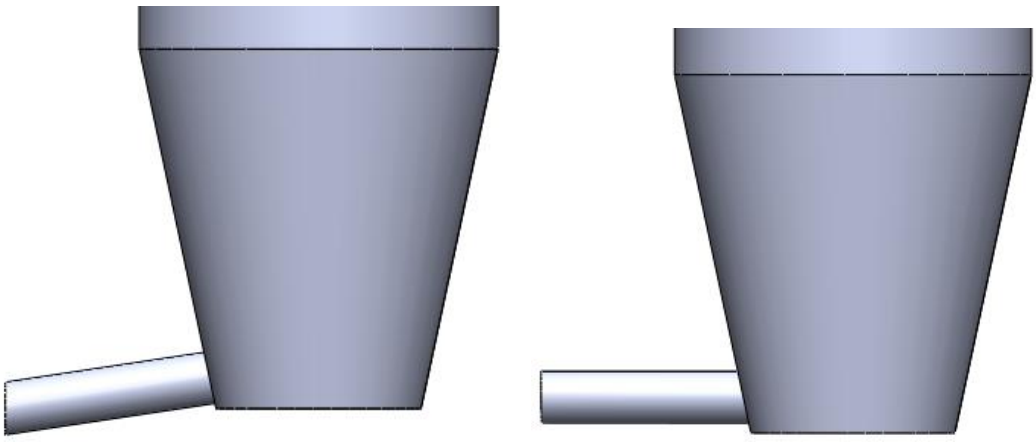

Figure 4.9 3D model for solution S02 (LHS) and S03 (RHS). Lateral view of basket.

Table 4.3 Set of virtual experiments for solution S02 and S03.

Virtual experiment	Spraying flow rate [ml/min]	Total air flow [Nm^3/h]	Bottom air flow [Nm^3/h]	Lateral air flow [Nm^3/h]	Ratio R
S02_W0.33	175	800	375.94	426.06	1.128
S02_W1	175	800	182.48	617.52	3.384
S02_W3	175	800	71.74	728.26	10.152
S03_W0.33	175	800	375.94	426.06	1.128
S03_W1	175	800	182.48	617.52	3.384
S03_W3	175	800	71.74	728.26	10.152

but, in VPs S02 and S03, it is placed collinear to the lateral inlet. The operating boundary conditions for VPs S02 and S03 are the same as the ones used for VP S01. Only three virtual experiments were performed for values of ratio $R = 1.128$, $R = 3.384$ and $R = 10.152$ for both the virtual prototypes. The two sets of virtual experiments for VPs S02 and S03 are summarized in Table 4.3.

4.4.1 Tangential fluid and particle velocity and particle volume fraction

The tangential fluid and particle velocity, are rather similar for VPs S02 and S03. For clarity and summary purposes, only pictures referring to VP S03 will be presented. When possible, the pictures will show the same quantities as the one presented for VP S01. The tangential inlet, placed at 0.07 m from the bottom of the basket, is not enough to ensure a complete tangential flow in the basket, as shown in Figure 4.10. Penetration of the fluid flow in the basket is, as expected, higher for $R = 10.152$, since the lateral flow rate is higher. As happened for VP S01,

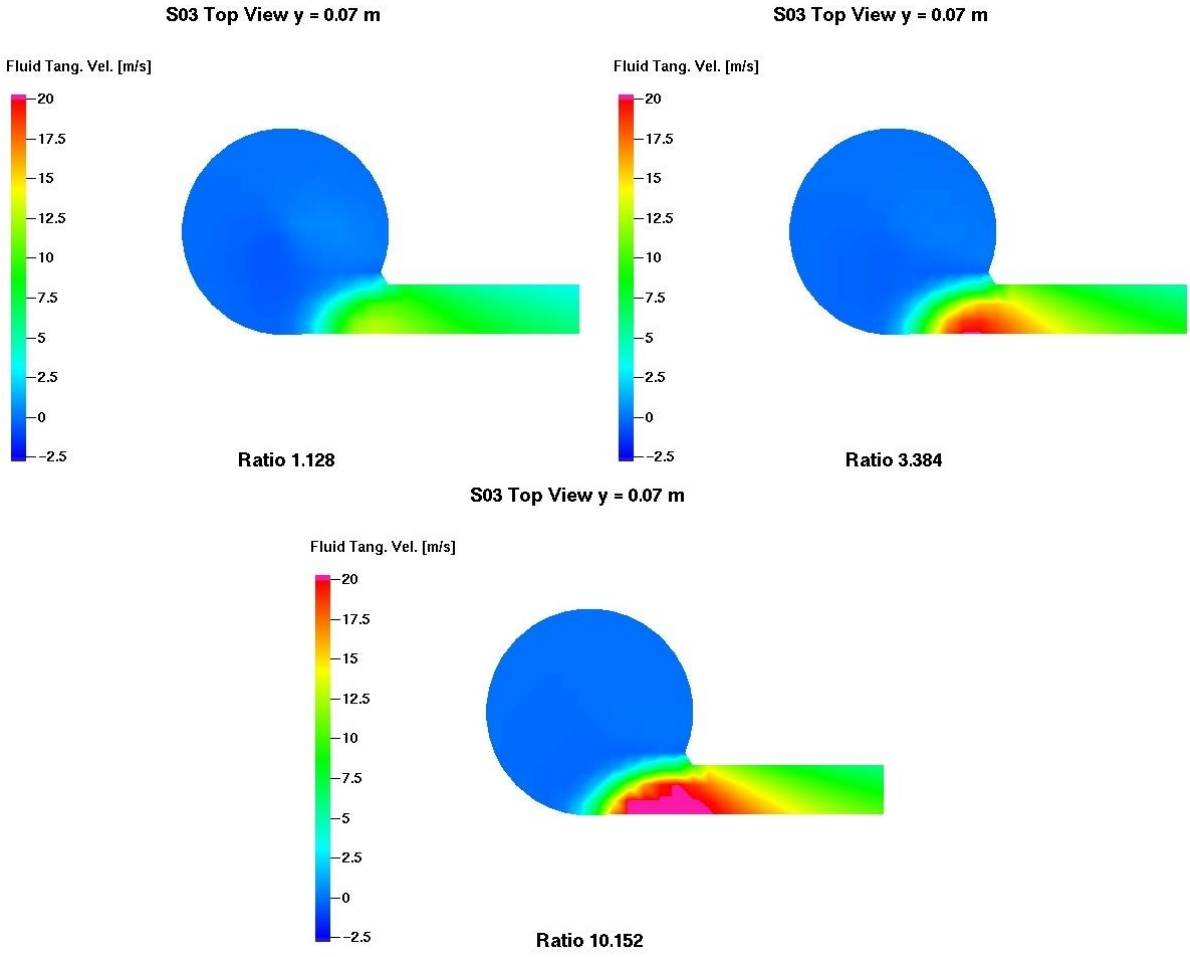

Figure 4.10 Top views at 0.07 m from the grid. Tangential fluid velocity for S03_W0.33 (top left), S03_W1 (top right) and S03_W3 (bottom). Positive velocities are clockwise.

evidences let the author think that the particle bed is too packed, and this let the fluid move upward to entrain particles. This supposition is confirmed by the vectors of average tangential velocity of particles shown in Figure 4.11. Particles are really entrained upwards by the high-speed lateral flow. Particles upwards entrainment is a major issue for VPs S01, S02 and S03, because it hinders the design of a Spin Flow Fluidized Bed. As occurred for VP S01, the explanation of this behavior could be the high volume fraction of particles, which are at almost at close pack condition ($\alpha_{cp} = 0.63$), in the section where lateral air flow is injected.

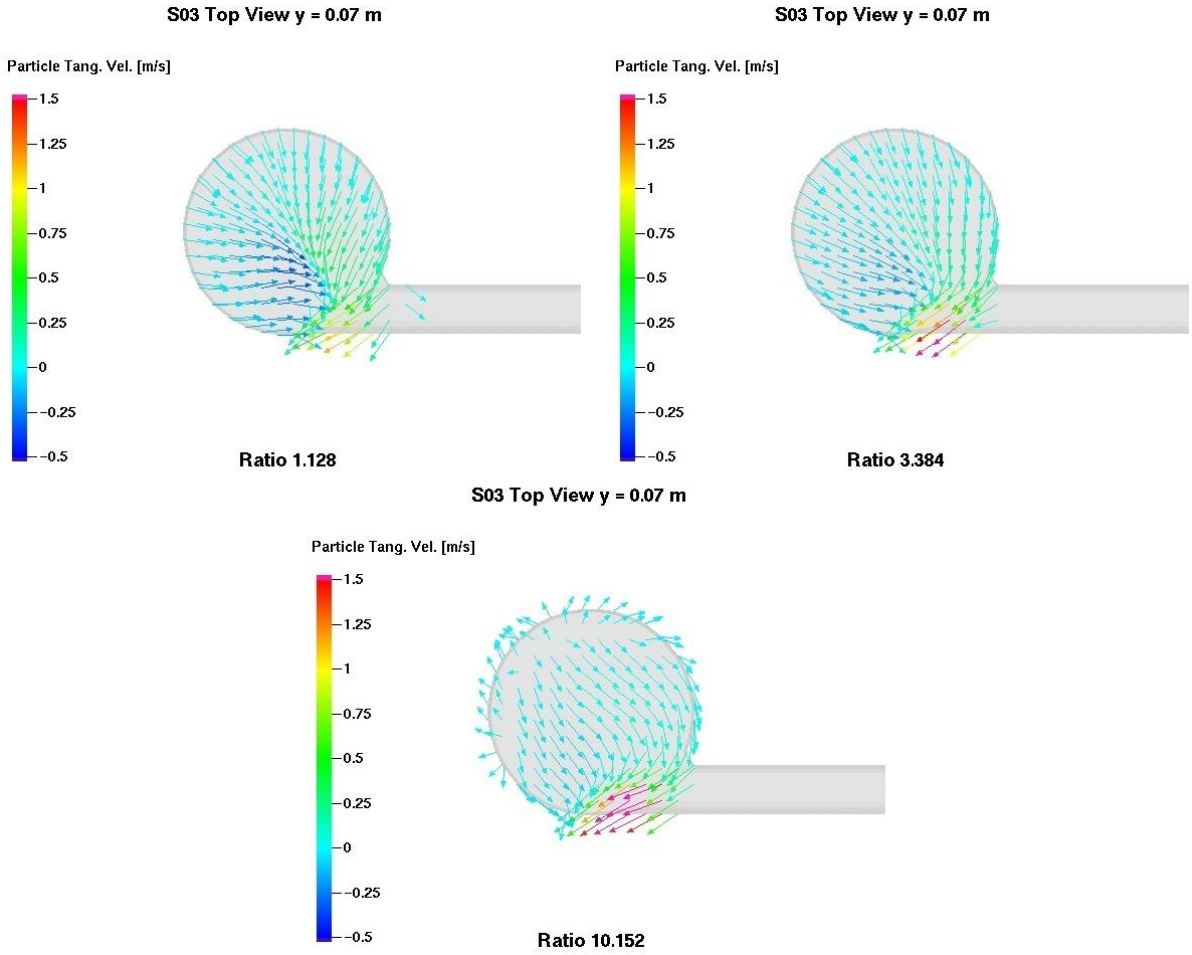

Figure 4.11 Top views at 0.07 m from the grid. Vectors of tangential particle velocity for S03_W0.33 (top left), S03_W1 (top right) and S03_W3 (bottom). Positive velocities are clockwise

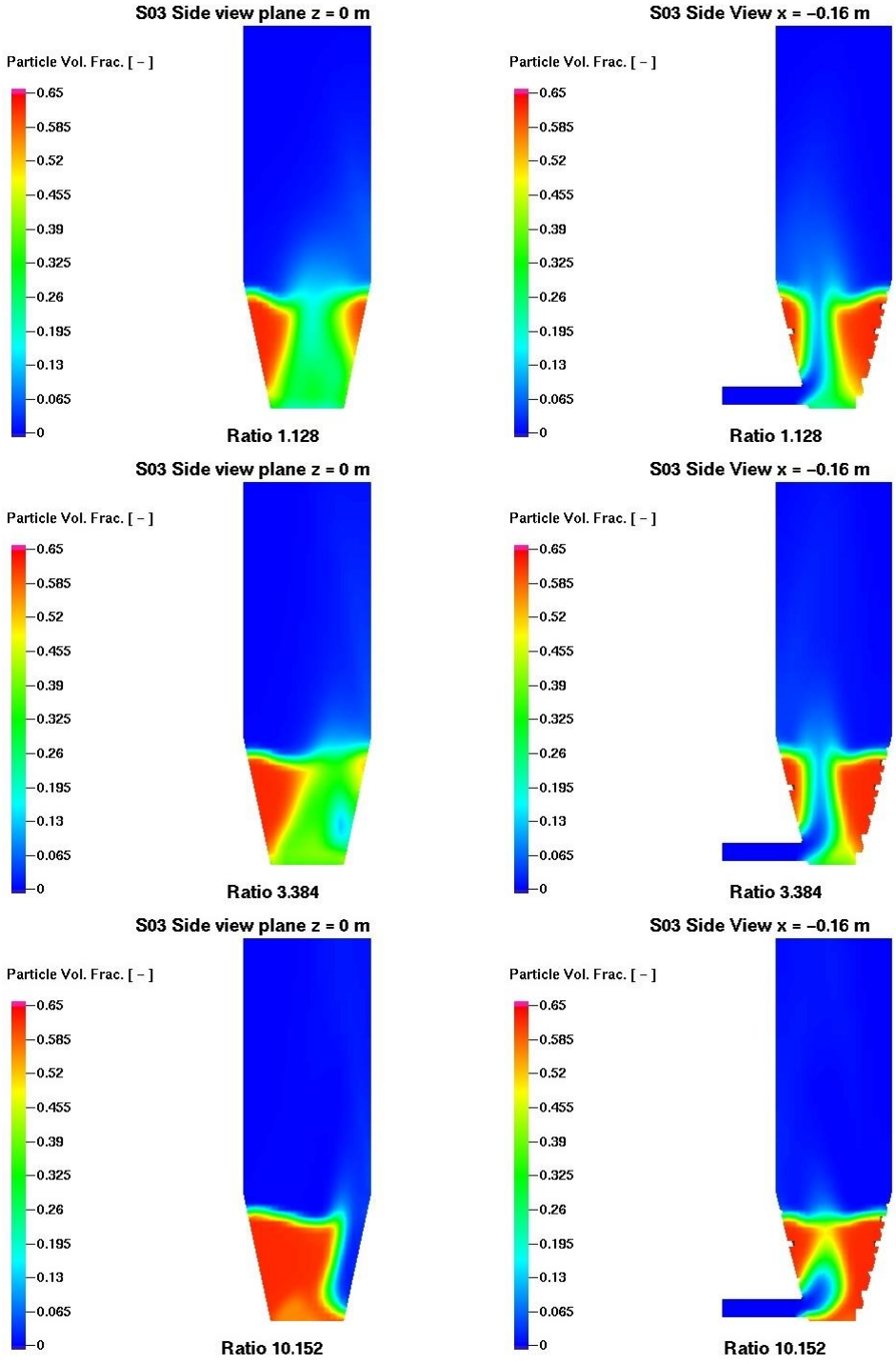

Figure 4.12 Side views of the particle volume fraction for solution S03. Middle side section (LHS) and side section at the entrance of the lateral inlet (RHS) for $R = 1.128$, $R = 3.384$ and $R = 10.152$ from top to bottom.

Table 4.4 Confidence width performance of virtual experiments for solutions S02 and S03.

Virtual experiment	Ratio R	CW best value	Time to reach $CW = 0.205$ [s]
S02_W0.33	1.128	0.195	214
S02_W1	3.384	0.195	227
S02_W3	10.152	0.205	519
S03_W0.33	1.128	0.195	220
S03_W1	3.384	0.195	232
S03_W3	10.152	0.205	504

However, looking at the particle volume fraction shown in Figure 4.12 the particle volume fraction at the bottom of the basket is decreased to a value around $\alpha_s = 0.35$ for $R = 1.128$ and $R = 3.384$ to a value around $\alpha_s = 0.58$ for $R = 10.152$. This ensures a well-mixed bed, even if the spin flow behavior is far from being obtained and there is a clear particles upward entrainment. It is believed that a perfect value of ratio R must be found to obtain a SFFB because bottom air flow rate allows the expansion of the particles bed, while the lateral inlet provides the tangential component of the particle velocity. However, to develop a good SFFB it is possible that the only solution would be to increase the total air flow rate.

4.4.2 Coating performance – Confidence Width

The bed good mixing behavior is confirmed by the positive coating performances expressed as confidence width results shown in Table 4.4. The coating performances of the virtual experiments with $R = 10.152$ are still not in line with the other S01, S02 and S03 results but they are better to virtual experiments 4 to 9 presented in Section 3.4.5, see Table 3.8. It is an important result because it means that this brand new process strategy could be comparable with

Table 4.5 Set of virtual experiments for solution S04.

Virtual experiment	Spraying flow rate [ml/min]	Total air flow [Nm^3/h]	Bottom air flow [Nm^3/h]	Lateral air flow [Nm^3/h]	Ratio R
S04_W0.33	175	800	375.94	4×106.52	1.128
S04_W1	175	800	182.48	4×154.38	3.384
S03_W3	175	800	71.74	4×182.07	10.152

the well-established Wurster process when it comes to coating performance expressed as confidence width.

4.4.3 Virtual Prototypes S02 and S03 choice

Virtual prototypes S02 and S03 gave very similar results, far below the uncertainty of the model used. Therefore, it is believed that, since the horizontal inlet is a simpler 3D model, VP S03 is the best choice to pursue from now on.

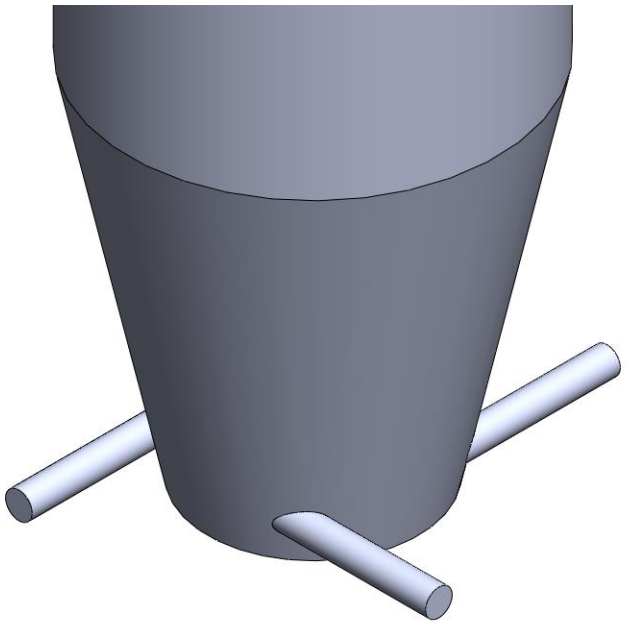

Figure 4.13 Isometric view of the basket used in VP S04. Inlets are radially equally distributed.

4.5 Virtual Prototype S04. 4 tangential inlets at 0.07 m from the support grid

The fourth spin flow virtual prototype S04 is derived from VP S03. At a height of 0.07 m from the support grid, 4 lateral inlets were modeled. These inlets provide in total the same lateral air flow rate as provided in previous VPs according to the value of R. The diameter of the four lateral inlets is half the diameter of the lateral inlets of the previous VPs: $d_{S04} = 50.8$ mm. This reduction was chosen because, at same total lateral air flow, the fluid velocity in the inlets stays the same. The isometric view of 3D model developed for this new VP is shown in Figure 4.13.

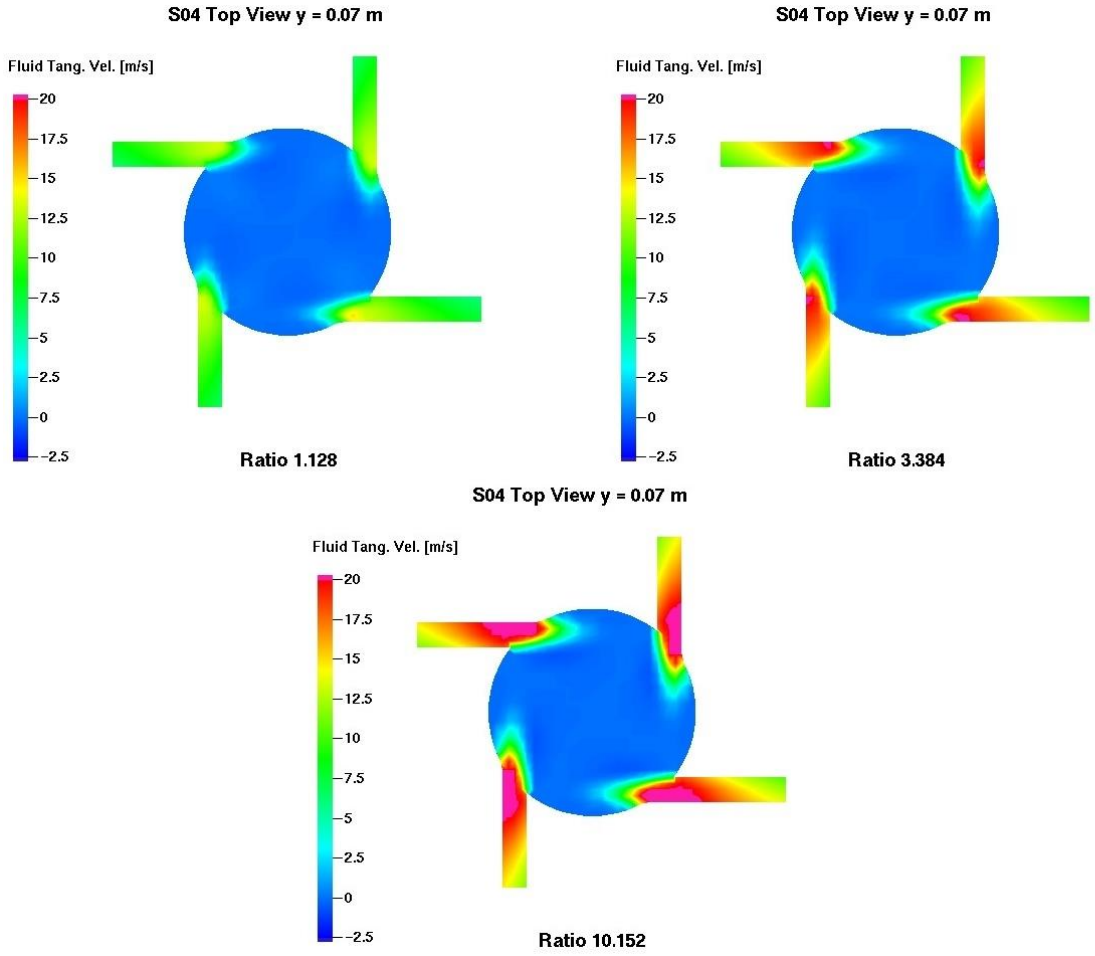

Figure 4.14 Top views at 0.07 m from the grid. Tangential fluid velocity for S04_W0.33 (top left), S04_W1 (top right) and S04_W3 (bottom). Positive velocities are clockwise.

for sake of comparison only one atomizer is placed collinear with one lateral inlet. The set of virtual experiments is given in Table 4.5. Due to the smaller inlets, the Eulerian mesh used was smaller and this led to an increased computational cost. Therefore, the total time simulated is reduced from 600 s to 300 s. While this reduction has an obvious effect on the best confidence width achieved, it has no impact on the average calculation of tangential fluid and particle velocity and on the average particle volume fraction. These quantities become time independent after less then 100 s for all VPs adopted.

4.5.1 Tangential fluid and particle velocity and particle volume fraction

Despite the velocity is kept constant, there is a general improvement of the penetration of fluid flow in the bed when using VP S04 as shown in Figure 4.14. Despite the complete tangential fluid flow is not achieved yet, the portion of the bed interested by the tangential fluid flow is larger than the one obtained with VPs S02 and S03 (see Figure 4.10). This is particularly true for $R = 3.384$ and $R = 10.152$. Therefore, it is expected that the fluid flow can partially

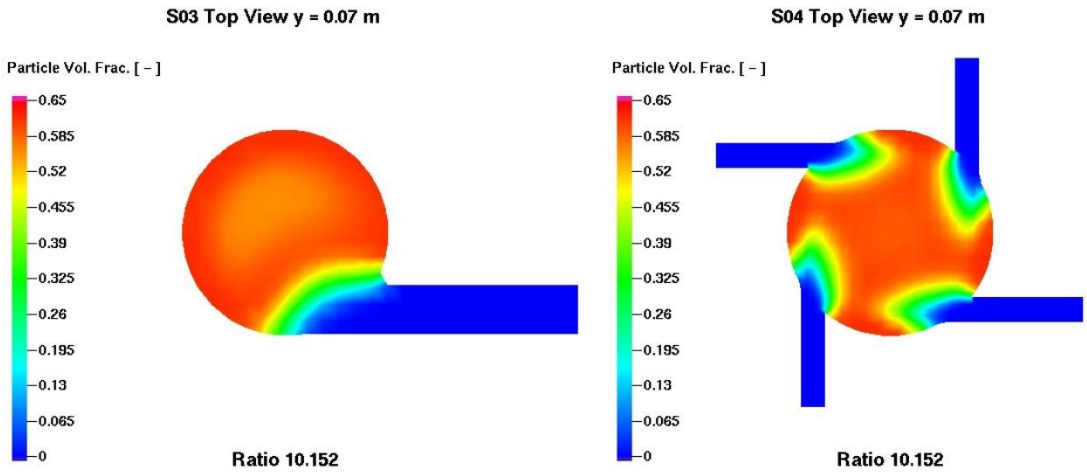

Figure 4.15 Top views of the particle volume fractions at 0.07 m from support grid. Comparison between different virtual experiments: S03_W3 (LHS) and S04_W3 (RHS).

Table 4.6 Confidence width performance of virtual experiments for solutions S04.

Virtual experiment	Ratio R	Time to reach $CW = 0.205$ [s]
S04_W0.33	1.128	227
S04_W1	3.384	245
S04_W3	10.152	289

fluidize the particles in the tangential direction. This is particularly easy to notice if the top views of particle volume fractions are compared. In Figure 4.15 the comparison for $R = 10.152$ of the VP S03 and VP S04 is given. It is clear the amount of particles far from the closing pack volume fraction is larger for VP S04. It is opinion of the author that each pinnacle of low solid fractions coming from the lateral inlets should reach the next one to develop a SFFB. Increasing the lateral inlets or the lateral air flow rate could be a valuable option to trigger the SFFB. Nonetheless, this VP achieves a very good particle mixing thanks to the high bed expansion shown in Figure 4.16. The spouted behavior, typical of the Wurster process, is reduced with respect to the other VPs and the bed results to be a little more expanded for $R = 3.384$ and $R = 10.152$.

4.5.2 Coating performance – Confidence Width

Since the bed mixing is improved it is expected that the confidence width performance would improve. For values of ratio $R = 1.128$ and $R = 3.384$ there is no improvement, but a small decrement of the performance since $CW = 0.205$ is reached a bunch of seconds later than the time it was reached using VP S03. However, these differences are far below what the author consider to be a significant difference to draw conclusions. On the other hand, an impressive

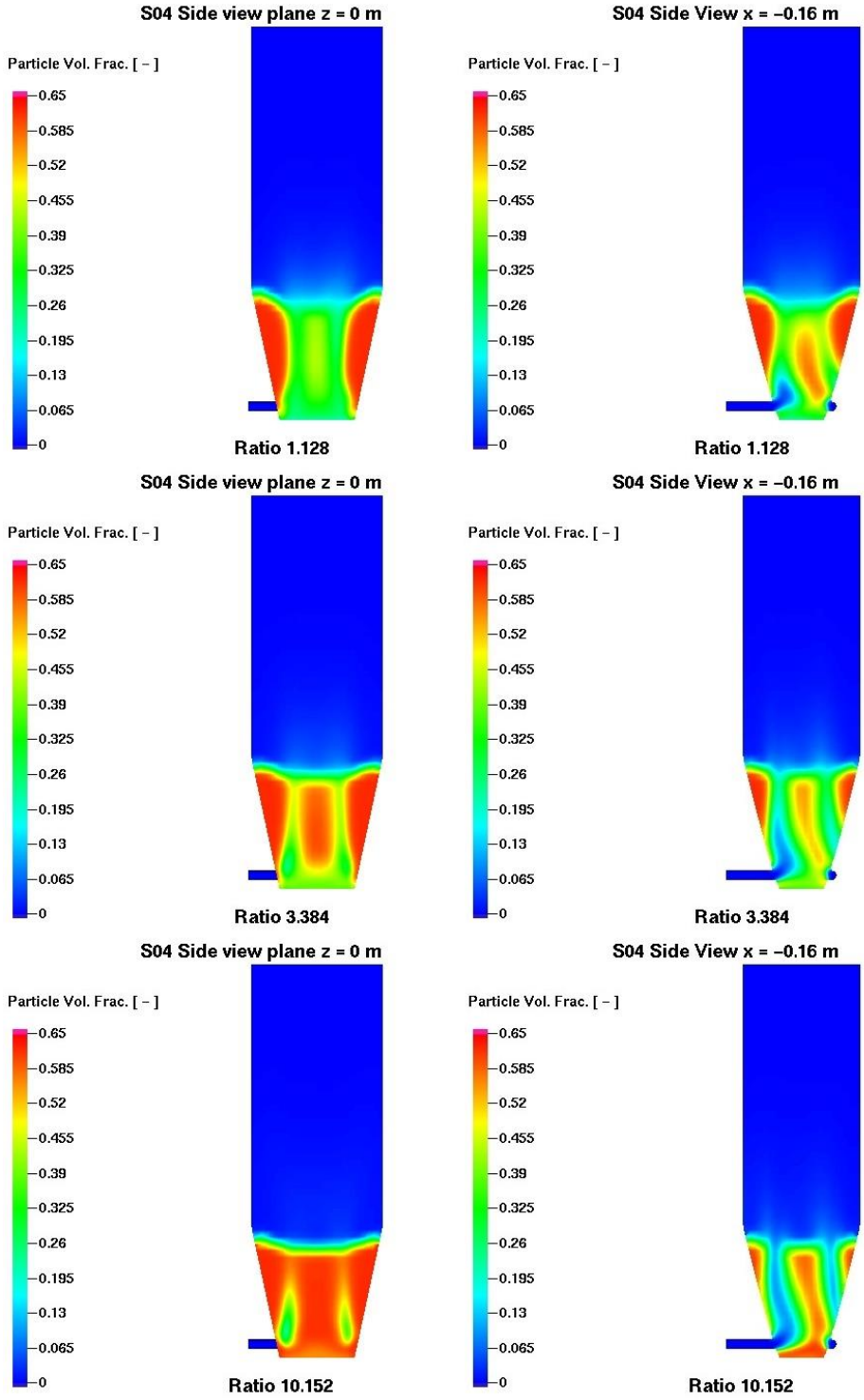

Figure 4.16 Side views of the particle volume fraction for solution S04. Middle side section (LHS) and side section at the entrance of a lateral inlet (RHS) for $R = 1.128$, $R = 3.384$ and $R = 10.152$ from top to bottom.

time it was reached using VP S03. However, these differences are far below what the author consider to be a significant difference to draw conclusions. On the other hand, an impressive increment larger than 200 s was achieved for $R = 10.152$. This virtual experiment is still the worse of the set, but the differences with the other two virtual experiments are minimal. The confidence width performance is summarized in Table 4.6 where the maximum confidence width (which is $CW = 0.205$) was not recorded to avoid confusion, since this VP ran for 300 s only.

4.6 Granulation in Virtual Prototype S04

As mentioned before, the SFFB aims to deal both with coating and granulation. Therefore, a granulation test was performed using virtual prototype S04 and a ratio $R = 3.384$. The operating and boundary conditions are the same as the one used for VP S04: the total air flow rate is 800 Nm^3/h and the spraying rate is 175 ml/min. The only difference is in the particle size

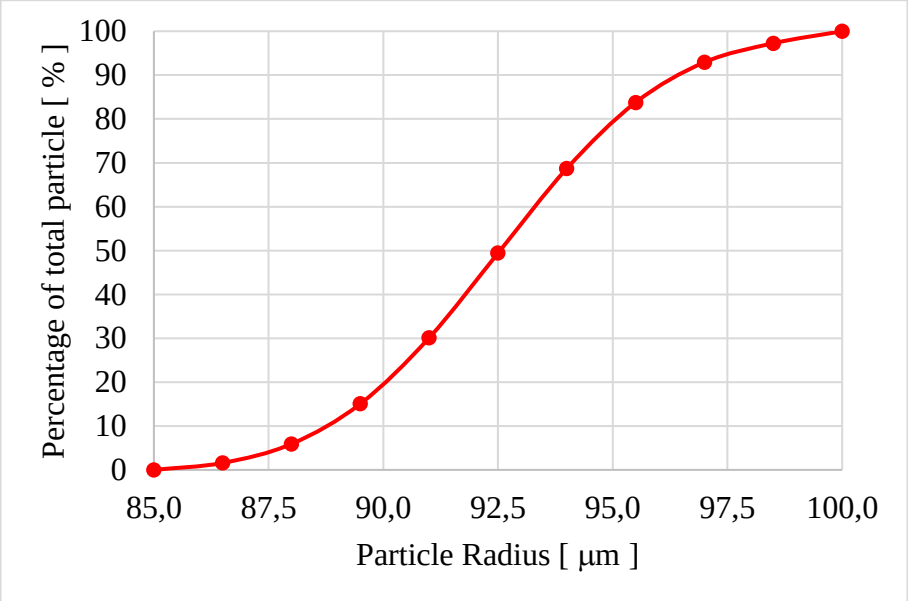

Figure 4.17 Cumulative particle size distribution used for granulation virtual experiment.

distribution. In the Barracuda VR model, the selected particles have the same distribution, but scaled down by a factor of 5, as shown in Figure 4.17.

4.6.1 Tangential fluid and particle velocity and particle volume fraction

Smaller particles are dragged more easily and the SFFB develops rapidly as can be seen from the tangential velocity of fluid shown in Figure 4.18. However, it seems that there is an asymmetric behavior. This asymmetry is likely due to the presence of the single atomizer, placed in the inlet on the bottom right in Figure 4.18. Its effect on the tangential fluid flow was not detected in the coating virtual experiments VP S04. This virtual experiment proves that the spraying atomizer could influence the flow. Particles move in a very recognizable spin flow behavior at the height equal to 0.07 m from the bottom of the basket, as shown by the vector of tangential velocity in Figure 4.19. However, this behavior is not kept when the bed rises to a

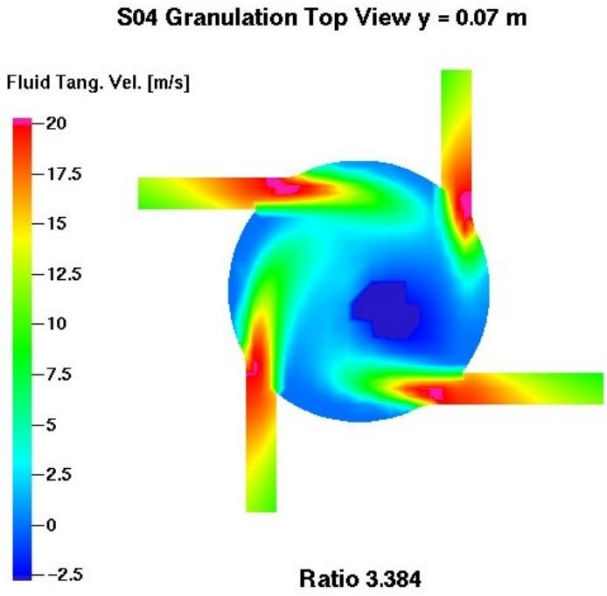

Figure 4.18 Top view at 0.07 m from the grid. Tangential fluid velocity for granulation test in VP S04. Positive velocities are clockwise.

height equal to 0.36 m from the bottom of the basket. At this height, the asymmetric behavior is clear. It is possible that the particle bed is in the conditions of bubbling fluidized bed and the presence of the atomizer could trigger the formation of bubbles. The average particle volume fraction in the bed, shown in Figure 4.20, shows that, likely due to the presence of the spraying atomizer, the bed has an asymmetric zone of high probability of bubbles or slug formation. In facts, the middle section side views from the x^{th} direction and from the z^{th} direction are completely different. However, the particle bed has a good degree of mixing that will probably have a good effect on the coating distribution.

4.6.2 Coating performance – Confidence Width

To be honest, it is wrong to talk about "coating performance", since this section deals with granulation and it is more correct to call it "binder distribution". However, for clarity and comparison with the other virtual experiments the coating performance will keep its name even in this section. This makes sense because the binder spraying is modeled in the exact same way

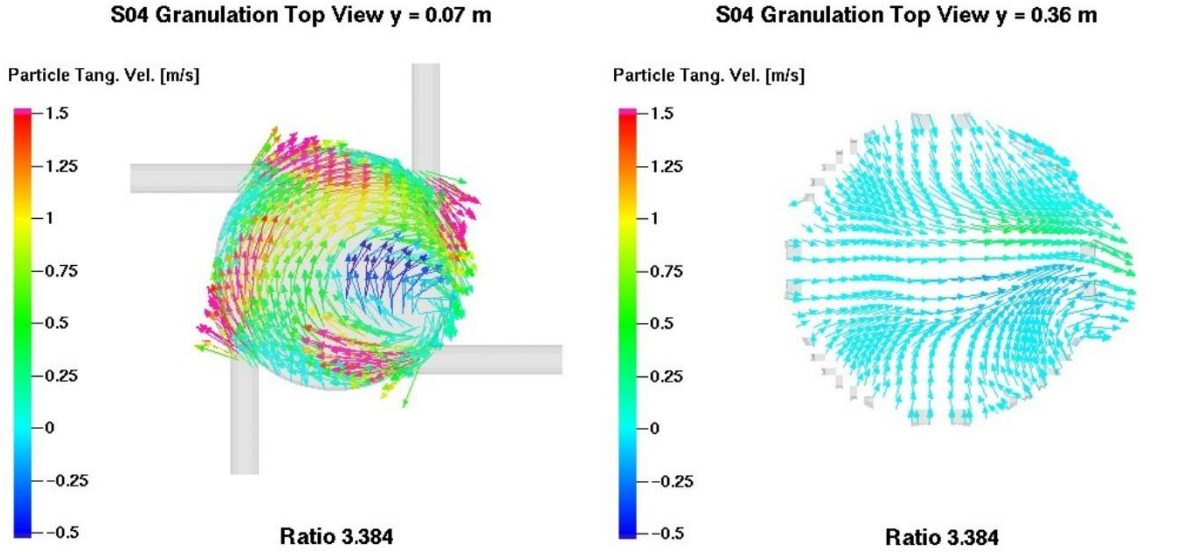

Figure 4.19 Top views at 0.07 m from the grid. Vectors of tangential particle velocity for S03_W0.33 (top left), S03_W1 (top right) and S03_W3 (bottom). Positive velocities are clockwise

as it was modeled in coating virtual experiments. The high level of mixing in the bed allowed to have a very good performance because the time to reach $CW = 0.205$ is 149 s, i.e., before any other virtual experiment performed so far. Moreover, after 220 s the confidence width reached the value $CW = 0.195$, far before any other virtual experiment.

4.7 Conclusive remarks

The present set of virtual prototypes does not allow to develop a Spin Flow Fluidized Bed for coating pellets. However, the suggestion of increasing the total air flow rate could be a valuable option to be tested with the present virtual prototypes. On the other hand, the Virtual Prototype S04 could be used for granulation purpose. The asymmetry due to the single atomizer could be overcome by adding one spraying atomizer per each inlet.

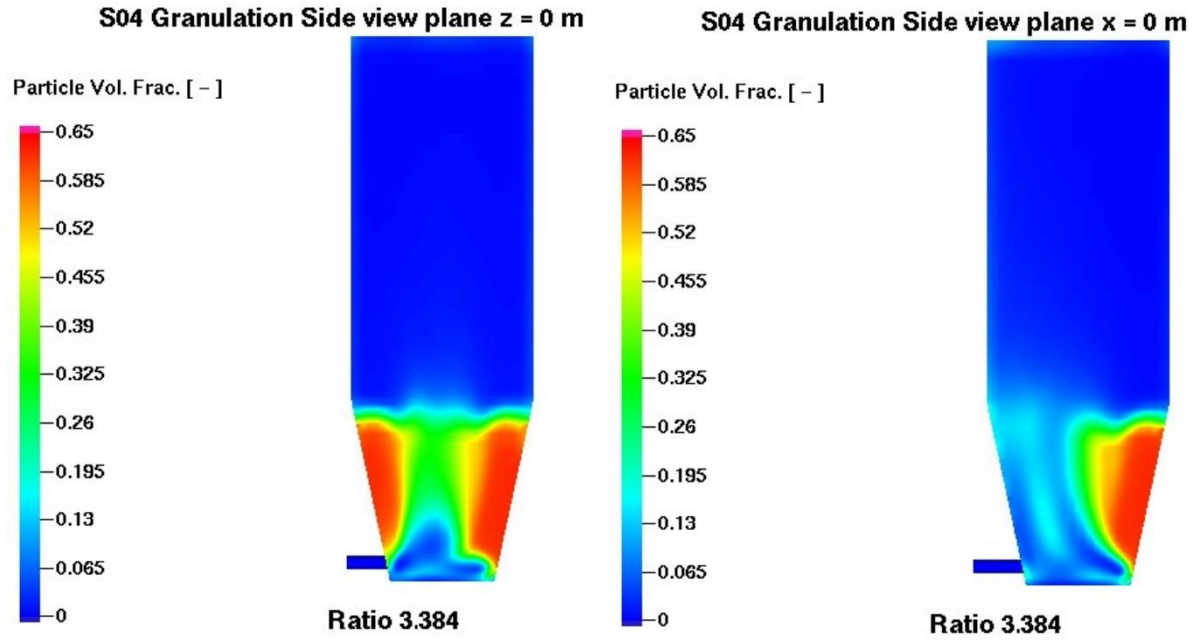

Figure 4.20 Particle average volume fraction. Middle side section views from the two directions.

Section 5
Conclusions and outlooks

In the work presented in this thesis a virtual prototyping methodology for pharmaceutical granulation and coating equipment has been developed and carried out by means of MP-PIC simulations. The application of this methodology was devoted to two cases starting from the same equipment, named ARIA 120. MP-PIC method, used with CPFD approach in Barracuda VR, is a powerful tool to model the gas-solid flows.

The first case involved the application of the MP-PIC method to simulate the use of ARIA 120 equipment when set in Wurster coating configuration. A set of 9 virtual experiments was carried out to replicate an already existing set of real experiments. This case study allowed to expand the knowledge of the Wurster process inside the ARIA 120 equipment by evaluating the coating distribution homogeneity introducing a set of performance indicators.

The second case involved the modeling of a new set of virtual prototypes of ARIA120 equipment in granulation configuration with a lateral additional inlet. Each virtual prototype was tested with a set of virtual experiments by varying the ratio between the lateral air flow rate and the bottom air flow rate. However, the desired spin flow behavior was not achieved for pellets coating and only partially achieved for granulation. The coating performances of these virtual prototypes are very good, indicating that further efforts in the virtual prototyping of these

solutions might lead to a valid option to substitute the actual Wurster process for coating used in ARIA120. It must be noticed that the end of this work does not provide a final and definitive prototype to be ready for production, but the most important achievement is the developing of a valuable method for virtual prototyping of granulators and coater using MP-PIC method. Scientific literature lacks modeling and simulation of the two-phase flow in granulators and coaters. Moreover, literature lacks modeling of coating or binder spraying in an Eulerian-Lagrangian framework, while this work presented a method to evaluate the coating or binder distribution performance.

An interesting by-products of the work was the investigation of the potential of Parallelization of calculation on NVIDIA CUDA cores boosted the pace of the research presented in this thesis since the software used (Barracuda VR) allowed this application.

However, some issues arose during the application of the MP-PIC as implemented in Barracuda VR. The strict cartesian Eulerian grid does not allow to model complicated geometry and, in this work, this feature would have been helpful to model the upstream part of the ARIA120 equipment. The use of different tools was needed. Coupling of different tools which works with different methods could be a source of errors. The derivation of the ratio of air flows in the central and annular part of the air distribution plate in the Wurster configuration could suffer this coupling error. Moreover, the validation performance of the MP-PIC approach led to an overestimation of the coating performance. Therefore, treatment of the performance obtained with Barracuda VR was always considered to be effective when compared with similar situations, thus, being a relative performance and not absolute. More efforts are needed to validate MP-PIC with experimental data for coating and granulation applications.

Further work will be performed to provide a definitive virtual prototype for an equipment which can perform both coating and granulation.

References

[1] M.G. Uccelli, M. Taisch, S. SpA, Cluster Smart Manufacturing 2020 CTN01_00163_216744, (2012) 1–77.

[2] H.S. Kang, J.Y. Lee, S. Choi, H. Kim, J.H. Park, J.Y. Son, B.H. Kim, S. Do Noh, Smart manufacturing: Past research, present findings, and future directions, Int. J. Precis. Eng. Manuf. - Green Technol. (2016).

[3] K. Łukaszewicz, Use of CAD Software in the Process of Virtual Prototyping of Machinery, Procedia Eng. 182 (2017) 425–433.

[4] G.G. Wang, Definition and Review of Virtual Prototyping, J. Comput. Inf. Sci. Eng. 2 (2002) 232.

[5] S. Barnat, A. Guédon-Gracia, H. Frémont, Virtual prototyping in a Design-for-Reliability approach, Microelectron. Reliab. 55 (2015) 1849–1854.

[6] G.Q. Zhang, A.A.O. Tay, L.J. Ernst, S. Liu, Z.F. Qian, H.J.L. Bressers, J. Janssen, Virtual thermo-mechanical prototyping of electronic packaging - Challenges in material characterization and modeling, Proc. - Electron. Components Technol. Conf. 0 (2001) 1479–1486.

[7] E. Conte, R. Morales-Rodriguez, R. Gani, The virtual product-process design laboratory for design and analysis of formulations, in: Comput. Aided Chem. Eng., Elsevier, 2009: pp. 825–830.

[8] J.S. Bao, Y. Jin, M.Q. Gu, J.Q. Yan, D.Z. Ma, Immersive virtual product development,

in: J. Mater. Process. Technol., Elsevier, 2002: pp. 592–596.

[9] H.Y.K. Lau, K.L. Mak, M.T.H. Lu, A virtual design platform for interactive product design and visualization, J. Mater. Process. Technol. 139 (2003) 402–407.

[10] H.Y. Kan, V.G. Duffy, C.J. Su, An Internet virtual reality collaborative environment for effective product design, Comput. Ind. 45 (2001) 197–213.

[11] I.M.A. S.p.A. Webpage https://ima.it/, (2017).

[12] ARIA webpage http://ima.it/pharma/machine/aria/, (2017).

[13] D.M. Parikh, M. Mogavero, Batch Fluid Bed Granulation, in: D.M. Parikh (Ed.), Handb. Pharmaceuitcal Granulation Technol., Taylor and Francis, 2005.

[14] L. Li, A. Rasmuson, A. Ingram, M. Johansson, J. Remmelgas, C. von Corswant, S. Folestad, PEPT study of particle cycle and residence time distributions in a Wurster fluid bed, AIChE J. 61 (2015) 756–768.

[15] J. De Wilde, Gas–solid fluidized beds in vortex chambers, Chem. Eng. Process. Process Intensif. 85 (2014) 256–290.

[16] H.S. Pordal, C.J. Matice, T.J. Fry, The Role of Computational Fluid Dynamics in the Pharmaceutical Industry, Pharm. Technol. (2002) 72–80.

[17] S. V Patankar, Numerical Heat Transfer and Fluid Flow, Hemisphere Publishing Corporation, 1983.

[18] B. Zhao, J. Wu, Numerical investigation of particle diffusion in a clean room, Indoor Built Env. 14 (2005) 469–479.

[19] D.M. Snider, P.J. O 'Rourke, The Multiphase Particle-In-Cell (MP-PIC) Method for dense particle flow., in: Comput. Gas-Solids Flows React. Syst. Theory, Methods Pract., 2011: pp. 1–38.

[20] M. Pell, J.B. Dunson, T.M. Knowlton, Gas-Solid Operations and Equipement, in: Perry's Chem. Eng. Handb., 8th ed., n.d.

[21] D. Geldart, Types of gas fluidization, Powder Technol. 7 (1973) 285–292.

[22] E. Teunou, D. Poncelet, Batch and continuous fluid bed coating - Review and state of the art, J. Food Eng. 53 (2002) 325–340.

[23] A. Rajesh, D. Reetika, A. Sangeeta, B. Ashok, Wurster Coating- Process and Product Variables, Int. J. Pharm. Inoovations. C (2012) 61–66.

[24] L. Li, J. Remmelgas, B.G.M. van Wachem, C. von Corswant, M. Johansson, S. Folestad, A. Rasmuson, Residence time distributions of different size particles in the spray zone of a Wurster fluid bed studied using DEM-CFD, Powder Technol. 280 (2015) 124–134.

[25] R. Šibanc, S. Srčič, R. Dreu, Numerical simulation of two-phase flow in a Wurster coating chamber and comparison with experimental results, Chem. Eng. Sci. 99 (2013) 225–237.

[26] S. Karlsson, A. Rasmuson, B. Van WaChem, I.N. Björn, CFD modeling of the wurster bed coater, AIChE J. 55 (2009) 2578–2590.

[27] B.J. Ennis, J.D. Litster, Particle size enlargement, in: D.W.G. RH Perry (Ed.), Perry's Chem. Eng. Handb., McGraw-Hill, 1997.

[28] B.J. Ennis, Theory of Granulation: An Engineering Perspective, in: D.M. Parikh (Ed.), Handb. Pharmaceuitcal Granulation Technol., Taylor and Francis, 2005.

[29] B.H. Ng, Y.L. Ding, M. Ghadiri, Modelling of dense and complex granular flow in high shear mixer granulator - A CFD approach, Chem Eng Sci. 64 (2009) 3622–3632.

[30] D.M. Parikh, Introduction, in: D.M. Parikh (Ed.), Handb. Pharmaceuitcal Granulation Technol., Taylor and Francis, 2005.

[31] R. Gokhale, Y. Sun, A.J. Shukla, High-Shear Granulation, in: D.M. Parikh (Ed.), Handb. Pharmaceuitcal Granulation Technol., Taylor and Francis, 2005.

[32] W. Zhong, A. Yu, G. Zhou, J. Xie, H. Zhang, CFD simulation of dense particulate reaction system: Approaches, recent advances and applications, Chem. Eng. Sci. 140 (2016) 16–43.

[33] E.-U. Hartge, L. Ratschow, R. Wischnewski, J. Werther, CFD-simulation of a circulating fluidized bed riser, Particuology. 7 (2009) 283–296.

[34] C.K.K. Lun, S.B. Savage, D.J. Jeffrey, N. Chepurniy, Kinetic theories for granular flow - Inelastic particles in Coutte-Flow and slightlty inelastic particles in a general flowfield, J Fluid Mech. 140 (1984) 223–256.

[35] J. Ding, D. Gidaspow, A bubbling fluidization model using kinetic theory of granular flow, AIChe J. 36 (1990) 523–538.

[36] X.-Z. Chen, D.-P. Shi, X. Gao, Z.-H. Luo, A fundamental CFD study of the gas-solid flow field in fluidized bed polymerization reactors, Powder Technol. 205 (2011) 276–288.

[37] B.G.M. van Wachem, J.C. Schouten, C.M. van den Bleek, R. Krishna, J.L. Sinclair, Comparative analysis of CFD models of dense gas-solid systems, AIChe J. 47 (2001) 1035–1051.

[38] M. Upadhyay, J.-H. Park, CFD simulation via conventional Two-Fluid Model of a circulating fluidized bed riser: Influence of models and model parameters on hydrodynamic behavior, Powder Technol. 272 (2015) 260–268.

[39] M. Syamlal, W. Rogers, T.J. O'Brien, MFIX Documtation, Theory Guide, (n.d.).

[40] A. MILLER, D. GIDASPOW, Dense, vertical gas-solid flow in a pipe, AIChe J. 38 (1992) 1801–1815.

[41] N. Yang, W. Wang, W. Ge, J. Li, CFD simulation of concurrent up gas solid flow in circulating fluidized beds with structure dependent drag coefficient, Chem Eng J. 96 (2003) 71–80.

[42] S.-C. Hu, C.-C. Chen, Locating the very early smoke detector apparatus (VESDA) in vertical laminar clean rooms according to the trajectories of smoke particles, Build Env. 42 (2007) 366–371.

[43] L. Fries, S. Antonyuk, S. Heinrich, S. Palzer, DEM-CFD modeling of a fluidized bed spray granulator, Chem. Eng. Sci. 66 (2011) 2340–2355.

[44] A. Kumar, K. V. Gernaey, T. De Beer, I. Nopens, Model-based analysis of high shear wet granulation from batch to continuous processes in pharmaceutical production - A

critical review, Eur. J. Pharm. Biopharm. 85 (2013) 814–832.

[45] H. Liu, M. Li, Two-compartmental population balance modeling of a pulsed spray fluidized bed granulation based on computational fluid dynamics (CFD) analysis., Int. J. Pharm. 475 (2014) 256–69.

[46] N. Hampel, A. Bück, M. Peglow, E. Tsotsas, Continuous pellet coating in a Wurster fluidized bed process, Chem. Eng. Sci. 86 (2013) 87–98.

[47] H.R. Norouzi, R. Zarghami, N. Mostoufi, New hybrid CPU-GPU solver for CFD-DEM simulation of fluidized beds, Powder Technol. 316 (2017) 233–244.

[48] H. Wang, G. Qiu, J. Ye, W. Yang, Experimental study and modelling on gas–solid flow in a lab-scale fluidised bed with Wurster tube, Powder Technol. 300 (2016) 14–27.

[49] D.M. Snider, An Incompressible Three-Dimensional Multiphase Particle-in-Cell Model for Dense Particle Flows, J. Comput. Phys. 170 (2001) 523–549.

[50] CPFD Software, Barracuda Virtual Reactor Manual, 2016.

[51] ANSYS, ANSYS FLUENT 15.0 Theory Guide, 2013.

[52] David C. Wilcox, Turbulence Modeling for CFD, 1993.

[53] ANSYS, ANSYS FLUENT 15.0 User's Guide, 20113.

[54] CD ADAPCO, STAR-CCM + ® Documentation, 2016.

[55] F.R. Menter, Two-equation eddy-viscosity turbulence models for engineering applications, AIAA J. 32 (1994) 1598–1605.

[56] J. Smagorinsky, General Circulation Experiments With the Primitive Equations, Mon. Weather Rev. 91 (1963) 99–164.

[57] M.J. Andrews, P.J. O'Rourke, The multiphase particle-in-cell (MP-PIC) method for dense particulate flows, Int. J. Multiph. Flow. 22 (1996) 379–402.

[58] CPFD Software, Barracuda Virtual Reactor Training Material, 2016.

[59] C.Y. Wen, Y.H. Yu, Mechanics of fludization, Chem. Eng. Prog. Symp. (1966).

[60] S. Ergun, Fluid flow through packed columns, Chem. Eng. Prog. 48 (1952) 89–94.

[61] R. Beetstra, M.A. Van Der Hoef, J.A.M. Kuipers, Drag force of intermediate reynolds number flow past mono- And bidisperse arrays of spheres, AIChE J. 53 (2007) 489–501.

[62] Y. Liang, Y. Zhang, T. Li, C. Lu, A critical validation study on CPFD model in simulating gas–solid bubbling fluidized beds, Powder Technol. 263 (2014) 121–134.

[63] L. Pirani, Studio ed analisi fluidodinamica di reattori a letto fluido in applicazioni farmaceutiche, 2012.

[64] A. Meslem, F. Bode, C. Croitoru, I. Nastase, Comparison of turbulence models in simulating jet flow from a cross-shaped orifice, Eur. J. Mech. - B/Fluids. 44 (2014) 100–120.

[65] B.E. Poling, G.H. Thomson, D.G. Friend, R.L. Rowley, W.V. Wilding, Physical and Chemical Data, in: Perry's Chem. Eng. Handb., Eighth, Mc Graw Hill, 2009.

[66] Data of IMA S.p.A., n.d.

[67] C. Melegari, S. Bertoni, A. Genovesi, K. Hughes, A.R. Rajabi-Siahboomi, N. Passerini, B. Albertini, Ethylcellulose film coating of guaifenesin-loaded pellets: A comprehensive evaluation of the manufacturing process to prevent drug migration, Eur. J. Pharm. Biopharm. 100 (2016) 15–26.

[68] J. De Wilde, A. de Broqueville, Experimental investigation of a rotating fluidized bed in a static geometry, Powder Technol. 183 (2008) 426–435.

[69] J. De Wilde, A. de Broqueville, Rotating fluidized beds in a static geometry: Experimental proof of concept, AIChE J. 53 (2007) 793–810.

[70] P. Eliaers, J. De Wilde, Drying of Biomass Particles: Experimental Study and Comparison of the Performance of a Conventional Fluidized Bed and a Rotating Fluidized Bed in a Static Geometry, Dry. Technol. 31 (2013) 236–245.

[71] A. de Broqueville, J. De Wilde, Numerical investigation of gas-solid heat transfer in rotating fluidized beds in a static geometry, Chem. Eng. Sci. 64 (2009) 1232–1248.

[72] W. Rosales Trujillo, J. De Wilde, Fluid catalytic cracking in a rotating fluidized bed in a static geometry: a CFD analysis accounting for the distribution of the catalyst coke content, Powder Technol. 221 (2012) 36–46.

[73] J. De Wilde, A. Habibi, A. de Broqueville, Experimental and numerical study of rotating fluidized beds in a static geometry, Int. J. Chem. React. Eng. 5 (2007).

[74] N. Staudt, A. De Broqueville, W. Rosales Trujillo, J. De Wilde, Low-Temperature Pyrolysis and Gasification of Biomass: Numerical Evaluation of the Process Intensification Potential of Rotating- and Circulating Rotating Fluidized Beds in a Static Fluidization Chamber, Int. J. Chem. React. Eng. 9 (2011).

Acknowledgements

It has been a hard journey, and many are the ones I wish to thank. I hope I won't forget any of them.

First, UniFe Professor Michele Pinelli because he firstly contacted me, offering this PhD position. His guidance throughout these three years was an important factor in the achievements I got.

Lorenzo Maldina, manager at I.M.A. S.p.A., was the most enthusiast supporter of my application to this PhD student position. It is likely that without him I would have not been admitted.

Professor Maria Grazia De Angelis was my supervisor during my PhD studies. Despite she was not directly involved in the project, she was always helpful when I had some doubts and she always gave good educational advices.

Thanks also to the other engineers at I.M.A. S.p.A.: Nicola Gandolfi, Silvio Sessa and Dario Fabbri.

The most "technical thanks" go to Federico Monterosso and Micaela Olivetti, OMIQ srl, for their priceless support in the use of Barracuda VR. Thanks also to Paola for making me able to take contact with OMIQ srl.

Thanks also to my coworkers in Ferrara office for shared with me these three years: Alessio Suman, Anna Vaccari, Carlo Bissaro, Carlo Buratto, Devid Dainese Elettra Fabbri, Matteo Occari, Nicola Aldi, Nicola Casari and Saverio Randi.

When I write, I make many mistake and therefor i wish to thank Jacopo Gabrielloni, Daniele Ghezzi and Caterina La Grotteria because they proof read parts of this thesis so I wont present such a bad orthography or silly mistakes as the ones in this sentence. Jacopo gave also good advices on the content of the thesis.

Outside the PhD related person, I would like to thank all my Ferrara, Bologna and Pesaro friends for giving me something to do when I was not in the office.

Francesco Pirisi. I don’t know why, but it turns out that he’s always close to me.

Roberta Cossuto for being very helpful during all this time, even when some things in my life didn't go exactly how I expected, since they cannot be predicted with a fluid dynamic model.

On this purpose, I wish to deeply thank Dr. Maria Antonietta Brugnoli for her professionality: it really helped me to be able to hand in this thesis. She was of primary importance for my motivation recovering and without her guidance I would have probably quit.

I would like to thank the whole AGESCI Pesaro 6 group, in particular, all the cub scouts I (successfully?) tried to educate in the last three years.

Thanks to Cristina, because she met me in the most stressful six months of my life and she still finds something interesting in me. Mystery.

Thanks to my parents, Tito and Mari, for their unconditional support. Seriously, they provided integration to the PhD scholarship.

Finally, thanks to my sister, Serena, and her partner, Matteo. They decided to give birth to the boys I dedicated my thesis to, Diego and Giacomo.